Detecting Corrosion in Aircraft Components Using Neutron Radiography

by

David Walter Fink

Submitted to the Department of Nuclear Engineering
in partial fulfillment of the requirements for the degree of

Master of Science

at the

MASSACHUSETTS INSTITUTE OF TECHNOLOGY

January 1996

Author ....
Department of Nuclear Engineering
January 18, 1996

Certified by ....
Richard Lanza
Principal Research Scientist
Thesis Supervisor

Read by ....
Lawrence Lidsky
Professor of Nuclear Engineering
Thesis Reader

Accepted by ....
Jeffrey Freidberg
Chairman, Departmental Committee on Graduate Students

Detecting Corrosion in Aircraft Components Using Neutron Radiography

by

David Walter Fink

Submitted to the Department of Nuclear Engineering
on January 18, 1996, in partial fulfillment of the
requirements for the degree of
Master of Science

Abstract

This work involved testing an accelerator based neutron radiography imaging system. The neutron source was a DL-1 radiofrequency quadrupole accelerator from AccSys technologies used to accelerate deuterium ions to 975 keV, producing neutrons in the $^9Be(d,n)B^{10}$ reaction. The goal of this work was to demonstrate the capability of the relatively new RFQ accelerator to provide a compact, mobile neutron source with an intensity sufficient for imaging purposes. Neutron production rates of up to 8.8E8 $\frac{n}{s}$ were achieved with the DL-1 source, with a thermal neutron flux of 1.3E4 $\frac{n}{cm^2 s}$ at the imaging plane. A mobile neutron source of this strength widens the applications possible for neutron radiography.

The imaging system used was a thermal neutron scintillator that was lens coupled to a cooled, charge coupled device. This provides a very low noise imaging system. The maximum signal level of the imaging system is 3.27E4 counts per pixel, with a readout noise of 76.7 counts per pixel and a dark current noise of less than 1 count per pixel per second.

Noise sources affecting the imaging system were investigated and minimized. The system capabilities were tested by imaging phantoms of known internal structure. The ability to use this system to image corrosion in aircraft components was tested by using the system on pieces of aircraft skin from actual aircraft with successful results.

Thesis Supervisor: Richard Lanza
Title: Principal Research Scientist

Acknowledgments

Finally, I would like to thank the people who, although they did not contribute directly to this work, were special to me in other ways. I would like to thank my roommate, Jon Lunglhofer, for being a true friend and dragging me up climb after climb. You introduced me to the vertical world, which will always be part of my life. For that, and putting up with me for almost two years, I thank you. Keep cranking hard.

I thank my girlfriend Carol Berrigan for supporting me and being there for me no matter how irritable or impatient I got. I love you.

I thank my parents, Harvey and Barbara Fink, for their unconditional love and support. Without them I wouldn't be where I am today. I love you.

Contents

List of Figures

List of Tables

Chapter 1

Introduction

1.1 Goals

Neutron radiography is a technique that has been proven to be an effective method for the non-destuctive evaluation of materials in a number of fields. It's applications, however, have been severely limited by the fact that neutron sources of sufficient strength were limited to fixed, expensive, and exceedingly complex nuclear reactors. Recent developments in ion accelerator technology have made cheaper, more compact accelerators with higher currents available for use in neutron generators.

These new, smaller, higher current accelerators have made portable neutron sources with sufficient intensity for radiography a reality. The reality of a mobile neutron source capable of generating the neutron flux required for imaging has opened many new applications to neutron radiography.

One of these applications is imaging corrosion in aluminum aircraft components. The main thrust of this work was to demonstrate the capability of one of these mobile neutron sources for imaging corrosion in aluminum. A commercially available, accelerator based neutron source was used along with an imaging system composed of commercially available components. The performance of this combined system was tested on phantoms whose composition was known and pieces of aircraft skin.

1.2   Contributions of This Thesis

The first contribution of this thesis was the characterization and mitigation of sources of noise in the imaging system used. It was found that photons produced from the neutron source caused noise in the imaging system, and that shielding components of the system with lead mitigated this noise.

A second contribution of the thesis was the use of phantoms of known content to characterize the performance of the imaging system. Specifically, signal attenuation and spatial resolution were investigated using phantoms of known hydrogen content in an aluminum matrix.

Finally, the ability of the system to image epoxy and corrosion in components taken from aircraft was demonstrated. A number of pieces of aircraft skin were obtained and radiographed. The results show the ability of this system to locate hidden corrosion and epoxy in aircraft components.

1.3   Organization of This Work

Chapter Two provides an introduction to tradiography theory and technique. It provides some of the physics that govern radiography and mathematics that govern imaging systems. Some brief historical notes and past uses of radiography are outlined.

Chapter Three describes why corrosion of aircraft components is a topic of growing concern and importance. A number of reasons for having a quick and reliable method for detecting corrosion of aluminum aircraft components are discussed. Additionally,

the chemistry of aluminum corrosion is detailed, indicating why neutron radiography is a valid technique for detecting this corrosion.

Chapter Four is a description of the imaging system used in this work. A brief overview of types of position sensitive neutron detectors is given. Each of the components of the imaging system is discussed. Characteristics of the entire imaging system such as spatial resolution, noise, dynamic range, and detector efficiency are characterized.

Chapter Five is a discussion of the neutron source. The advantages and disadvantages of the three basic types of neutron source (reactor, accelerator, isotope) is given. A brief outline of the theory behind radiofrequency quadrupole accelerators is included. Specific characterization of the DL-1 source characteristics, such as source strength and neutron spectrum produced, is provided.

Chapter Six details how the phantoms used to test the system were created. It also contains the reults of using the imaging system on these phantoms. The actual results are compared to the results predicted by theory.

Chapter Seven describes the samples of aircraft skin used to test the system and the radiographs of those samples.

Chapter Eight contains the conclusion reached doing this work and suggestions for future work related to this imaging system.

Chapter 2

General Properties of Radiography

2.1 History of Radiography

Radiography is an imaging technique that has been as a non-destructive method for the evaluation of materials. The earliest use of radiography occurred the first time someone held an object up to a bright light to determine what was inside it. This is obviously an exceedingly simple case, but it is radiography, i.e. a projected shadow image.

The first use of a more technical form of radiography came with the discovery of x-rays by Roentgen in 1895[17, p. 1]. He found that a electron beam device caused exposure of photographic film. Roentgen also found that placing different materials between the electron tube and the film would sometimes form a shadow image of the object on the film. We now know that the film exposure was caused by x-rays, and the reason different materials altered the amount of exposure seen in the film was that these different materials stopped some of the x-rays, preventing them from reaching the film. This was later put to use in medicine when it was discovered that flesh was more easily penetrated by x-rays than bone, causing the two to show up with different intensities on photographic film.

The neutron was not discovered until 1932 by Chadwick[17, p. 1]. Problems with neutron sources and neutron detectors prevented investigation of neutron radiography until 1948, when Kallman began to research the possibilities[22]. Industrial applications of the technique were explored by Thewlis in 1956[35] and continued by Berger in 1985[4].

Until recently, these industrial applications were limited by the fact that the only neutron sources strong enough to allow neutron radiography were nuclear reactors. This meant that samples to be radiographed had to be small enough to be transported into an existing reactor, and shipping costs would add to the cost of testing. Additionally, the early techniques for imaging neutron beams were rather complicated and involved a number of steps. They took a long time and did not have very good resolution.

Neutron radiography has been used in the past to image:

- Distribution of explosives in pyrotechnics (ammunition and shells)

- Gaps in seals and sealants

- Bond voids

- Corrosion, moisture, and hydrogen content in metals

- Nuclear fuel rods

- Welds

- Hydrocarbon fuels and lubricants[16, p. 71]

- Electronics[25, p. 81]

These uses of neutron radiography prove that it is a useful and viable technology. However, more widespread application of this technology has been limited by the fact
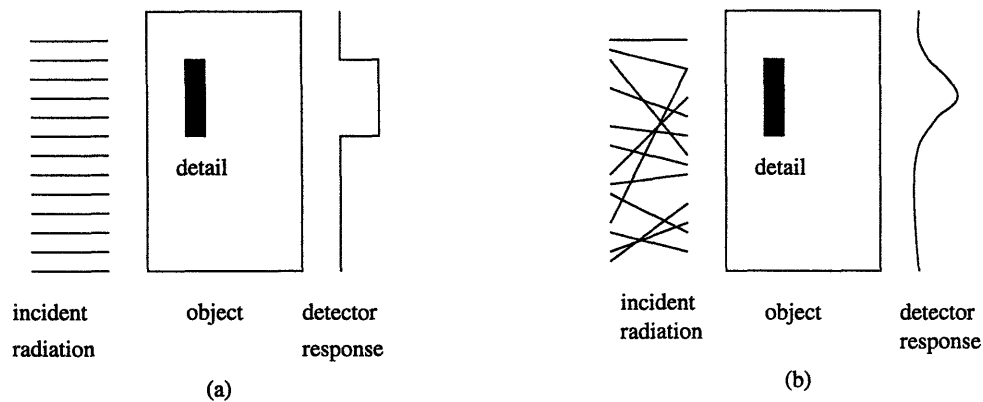
Figure 2-1: Importance of Collimation for Spatial Resolution

that it requires an fixed neutron source (a nuclear reactor) and the need for improved neutron imaging systems.

2.2 Theory of Radiography

Radiography is the process of creating a projected shadow image. Radiation is passed through an object, and the spatial distribution of the radiation flux on the opposite side of the object was the "projected shadow." Differences in the amount of radiation that pass through the object at different positions indicate different material properties of the object at different positions.

2.2.1 Requirements for Radiography

Collimation

One requirement for good radiographic imaging is that the radiation is well collimated. If the radiation is not collimated, image resolution is lost. The difference between the image formed using a highly collimated beam and using a beam with poor collimation is displayed in Figure 2.1.

The beam on the left (Figure 2.1a) shows excellent collimation. The image formed
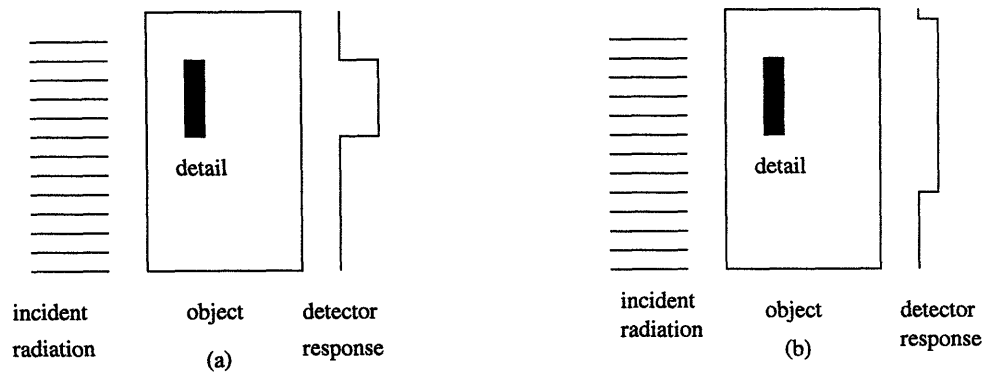
Figure 2-2: Importance of Detector Spatial Resolution for Radiography

using this source shows the clean, sharp edges of the interior detail. The uncollimated beam (Figure 2.1b) blurs the edges of the detail in the image due to radiation passing through the object at different angles. This problem is accentuated for thicker objects and systems with larger distances between the object and the detector.

Detector

Radiography also requires a position sensitive detector with a high spatial resolution. If the detector does not have high spatial resolution, the image will be blurred. In Figure 2.2a one can see how a detector with a high resolution can show the sharp edge of the detail and represent its size accurately. Figure 2.2b shows a detector with large pixel size. The detail in the object smaller than the detector pixel cannot accurately be imaged. It appears as a larger, less dense detail than it actually is due to the detector pixel size.

Radiation

Radiography also requires certain characteristics of the radiation attenuation through the object. First, the radiation must be able to penetrate the bulk object. Otherwise, the detector response is zero for all positions, as illustrated in Figure 2.3a. Second, there must be a difference of attenuation through materials that one wishes to dis-

19
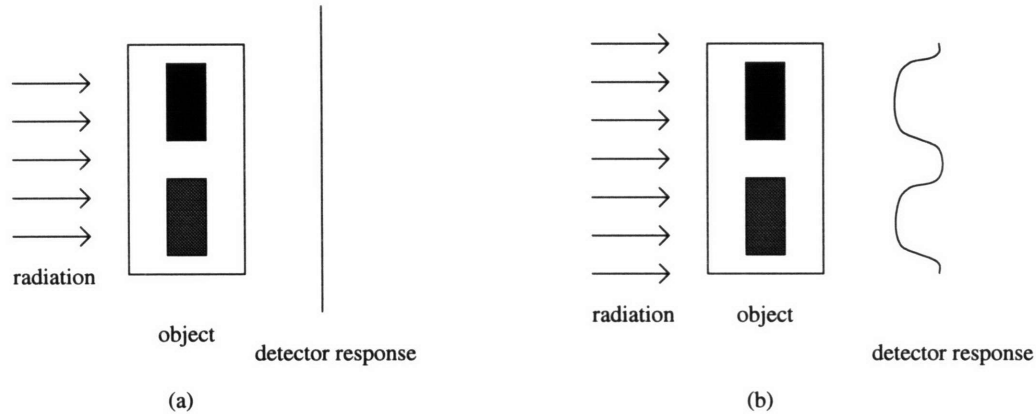
Figure 2-3: Object Containing Two Materials with Similar Radiation Attenuation Properties

tinguish between. If the radiation is attenuated the same amount by two different materials, it is impossible to distinguish between them by looking at the detector response. Both appear as equally dark spots on the image. Figures 2.3a and 2.3b each show an object with two different materials inside of it. Each material has the same attenuation properties as the other, so they appear the same on the image. Figure 2.3b shows the identical detector response to two different materials with the same attenuation characteristics.

2.2.2   Fluence Requirements for Radiography

The fluence required to form a radiographic image depends on many factors, including the size of the details one wishes to image, the efficiency of the detector, the attenuation of the bulk object, the difference in attenuation between the detail and the bulk object, and the desired signal to noise ratio.

The mathematical relationship between these factors is relatively easy to derive. First, realize that the signal generated is simply the difference in the detected flux between the detail and the rest of the object.

$$signal = \Phi(e^{-\mu D} - e^{-\mu(D-\Delta x)}e^{-(\mu+\delta\mu)(\Delta x)})\eta \qquad (2.1)$$

Where:

- Φ = total fluence (particles/unit area)

- D = thickness of object

- μ = attenuation coefficient of bulk object

- Δx = size of detail to be imaged

- $\mu + \delta\mu$ = attenuation coefficient of detail to be imaged

- η = detector efficiency

If we assume a well collimated beam and a perfect detector, the only noise present is due to statistical variation of the number of detected neutrons. Assuming that the beam conforms to Poisson statistics, the noise is easily characterized.

$$noise = \sqrt{\Phi\eta e^{-\mu D}} \qquad (2.2)$$

Define the signal to noise ratio, Ψ, and simplify:

$$\Psi = \sqrt{\frac{\Phi(\delta\mu)^2\Delta x^4\eta}{e^{\mu D}}} \qquad (2.3)$$

Rewriting this equation to express the required fluence to image details of a given size with a specific signal to noise ratio yields:

$$\Phi = \frac{\Psi^2 e^{\mu D}}{(\delta\mu)^2\Delta x^4\eta} \qquad (2.4)$$

Equation 2.4 shows that fluence must be increased dramatically to image smaller and smaller objects (as Δx decreases, Φ increases rapidly). Additionally, as attenuation through the bulk object increases (μD increases), the required fluence increases. As

the difference in attenuation between the detail and the bulk object increases ($\delta\mu$ increases), the required fluence drops rapidly.

2.3   Spatial Resolution of Imaging Systems

An imaging system may be thought of mathematically as an operator that acts on a function representing the physical object and returns a function that we call the image.

$$g(x,y) = S[f(x,y)] \qquad (2.5)$$

Where:

- g(x,y) = image function

- f(x,y) = object function

- S[f] = imaging system

As an example consider a medical x-ray. The physical object is some part of a human body, perhaps an arm. The function f(x,y) would be the distribution of x-ray attenuation coefficients in the arm. The image function g(x,y) would consist of the brightness of the photographic film at position (x,y).

Definition of a Linear, Stationary System

One type of imaging system is a linear, stationary system. These systems are mathematically easier to analyze and are used for many imaging applications. Linear, stationary systems are more tractable mathematically because the image function, g(x,y), is the superposition of the imaging system function acting on each point of the object function (definition of linear system), and the imaging system function is identical for each point in the object function (definition of stationary system).

Using these two properties, we can rewrite equation 2.5:

$$g(x,y) = \int \int f(x_1, y_1) h(x - x_1, y - y_1) dx_1 dy_1 \qquad (2.6)$$

$$g(x,y) = \int \int f(x - x_1, y - y_1) h(x_1, y_1) dx_1 dy_1 \qquad (2.7)$$

Where:

- (x,y) = position in image space

- (x_1, y_1) = position in object space.

- g(x,y) = image function

- $f(x_1, y_1)$ = object function

- h(x,y;x_1, y_1) = mapping function

Here we have replaced the imaging system function, S[f(x,y)], with the linear superposition (sum) of the imaging system acting on each point in the object function. Because the system is stationary, the imaging system function is identical for each point in the object function. We have replaced the imaging system function S[f(x,y)] with h(x,y), where:

$$h(x,y) = S[\delta(x_1, y_1)] = S[\delta(x_2, y_2)] = S[\delta(x_3, y_3)]... \qquad (2.8)$$

Thus, h(x,y) is simply the result of the imaging system acting on a point. For this reason, h(x,y) is called the point spread function, or PSF. Equation 2.7 shows that the image function, g(x,y), is simply the convolution of the PSF, h(x,y) and the object function, f(x,y).

Frequency Domain and Edge Response

We may change the convolution encountered in equation 2.7 into a simple multiplication by taking the Fourier Transform of equation 2.7. The two dimensional transform of any function f(x,y) is defined as:

$$F(k_x, k_y) = \int \int f(x,y) e^{-i(k_x x + k_y y)} dx dy \qquad (2.9)$$

where:

- $F(k_x, k_y)$ = Fourier Transform of f(x,y)

- (k_x, k_y) = Frequency domain coordinates corresponding to (x,y) in the position domain

Taking the Fourier Transform of equation 2.7 yields:

$$G(k_x, k_y) = F(k_x, k_y) H(k_x, k_y) \qquad (2.10)$$

The convolution has been replaced with multiplication. Thus, a useful function to characterize a system is the Fourier transform of the point spread function. However, because it is difficult to create a true "point" object to measure the point spread function, systems are usually defined by a line response function.

The line response function (LRF) is defined as the point spread function (PSF) integrated over one variable:

$$l(x) = \int \int \delta(x_1 - x_0) h(x_1, y_1) dx_1 dy_1 \qquad (2.11)$$

$$l(x) = \int h(x_0, y_1) dy_1 \qquad (2.12)$$

where:

- l(x) = line response function

- $\delta(x)$ = line at x = x_0

- h(x,y) = point response function

The line response function is much easier to measure experimentally. All that is required is an edge of material that is opaque to the imaging radiation used for the system. This "edge" can be represented mathematically as an object function:

24

f(x,y) = 0   f(x,y) = 1

Xo
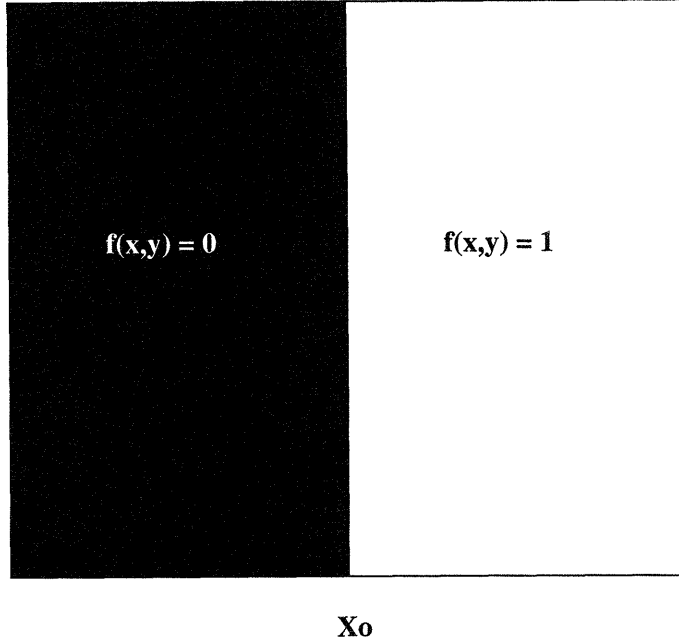
Figure 2-4: Edge Function

$$f(x, y) = 0 \, for \, x < x_0 \tag{2.13}$$

$$f(x, y) = 1 \, for \, x > x_0 \tag{2.14}$$

By taking the derivative of the edge response, we can obtain the line response.

$$\frac{d}{dx} f(x, y) = 0 \, for \, x > x_0, x < x_0 \tag{2.15}$$

$$\frac{d}{dx} f(x, y) = 1 \, for \, x = x_0 \tag{2.16}$$

$$\frac{d}{dx} f(x, y) = f'(x, y) = \delta(x - x_0) \tag{2.17}$$

Let the edge response be represented mathematically as e(x):

$$e(x) = \int \int f(x, y) h(x_1, y_1) dx_1 dy_1 \tag{2.18}$$

Taking the derivative of the edge response with respect to x yields:

25

f'(x,y) = 0   f'(x,y) = 0

f'(Xo) = 1

Xo
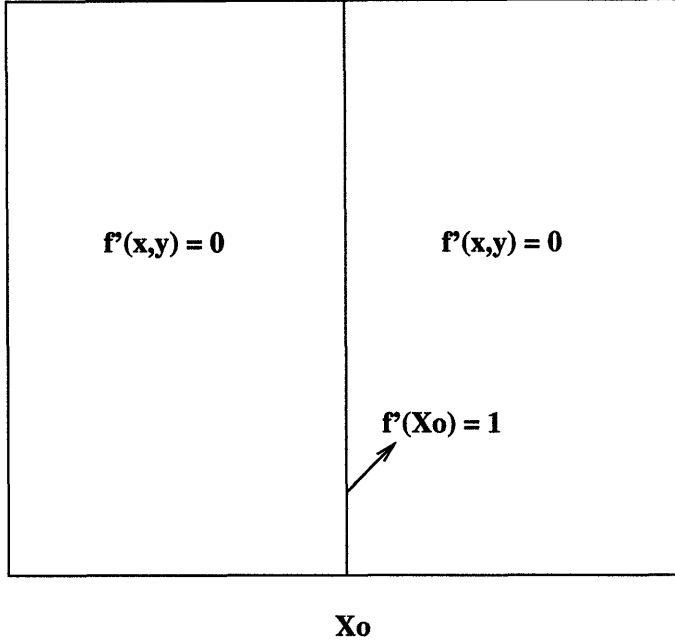
Figure 2-5: Derivative of Edge Function

$$\frac{d}{dx}e(x) = \frac{d}{dx}\int\int f(x,y)h(x_1,y_1)dx_1dy_1 \qquad (2.19)$$

$$\frac{d}{dx}e(x) = \int\int f'(x,y)h(x_1,y_1)dx_1dy_1 \qquad (2.20)$$

$$e'(x) = \int\int \delta(x_1 - x_0)h(x_1,y_1)dx_1dy_1 \qquad (2.21)$$

$$e'(x) = l(x) \qquad (2.22)$$

2.4 Neutrons vs. X-Rays

In order to determine which type of radiation is best suited for a particular imaging application, one must keep in mind the requirements for radiography previously discussed in section 2.2.1. We determined that in the ideal case the radiation used would penetrate the bulk object unattenuated, and that $\delta\mu$ would be as high as possible. These two characteristics would minimize the fluence required to image objects with a specified resolution with a specified signal to noise ratio (see equation 2.4).

26
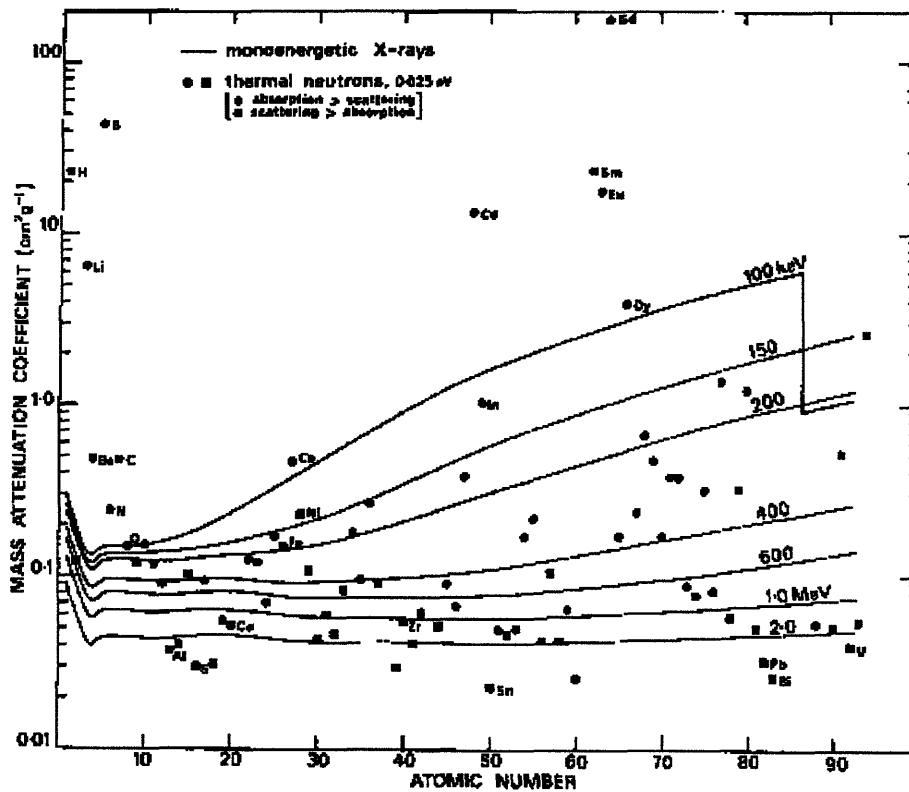
Figure 2-6: Neutron vs Photon Attenuation Characteristics

Interactions of X-Rays with Matter

Photons interact with matter mostly through interactions with atomic electrons. This means that photon attenuation is highly dependent on electron density, which increases with atomic number Z and material density. Thus a x-ray radiograph yields information primarily regarding the electron density of the object.

Photon attenuation also depends on photon energy. Figure 2.6 shows a plot of the attenuation coefficient vs. atomic number for photons ranging in energy from 100 keV to 2 MeV. The general trend of increasing attenuation with increasing atomic number can easily be seen, especially in the lower energy photons. Another important feature is that attenuation decreases with increasing photon energy and becomes less dependent on atomic number.

Interactions of Neutrons with Matter

Neutrons interact with matter in a much different way than x-rays. Neutrons almost never interact with atomic electrons; instead they are much more likely to interact with the nucleus. The result is that neutron attenuation varies a great deal from nucleus to nucleus. Looking at Figure 2.6 one can see that neutron attenuation coefficients vary over a much wider range of the logarithmic vertical axis than the x-ray attenuation coefficients. This nuclear interaction means that a neutron radiograph yields information regarding the isotopic content of the object imaged; an x-ray radiograph only gives information about electron density.

2.4.1   Applications Suited to Neutron Radiography

Inspecting Figure 2.6, one can easily see why neutron radiography was used for the applications listed at the beginning of this chapter. All involve the imaging of a hydrogen containing material in a metal matrix. Hydrogen is present in the explosives inside of a metallic shell casing, in the rubber or organic seal used in most seals and sealants, in the epoxy used to form bonds between metals or other materials, in many corrosion products found trapped in metallic matrices, in water which may leak into cracks in the metal cladding of nuclear fuel rods, and in the fuels and lubricants used in metallic engines.

Figure 2.6 indicates that hydrogen has a very large neutron cross section, and most structural metals (Al, Fe) have much lower neutron cross sections. This relationship is reversed for low energy x-rays, which show a low cross section for hydrogen and a high cross section for most metals. The x-rays are heavily attenuated in the metals, making them a poor choice for imaging details within metal structures. The x-ray cross section for metals drops with increased x-ray energy allowing penetration of metallic objects, but higher energy x-rays present a different problem. They show a relatively uniform attenuation coefficient for all materials, meaning $\delta\mu$ is small. Neu-

trons are clearly a much better choice for imaging hydrogen containing compounds in metals than x-rays.

Chapter 3

Radiography of Corrosion in Aircraft Structures

3.1   Costs Associated with Corrosion

Corrosion is defined as "destructive attack of a metal by chemical or electrochemical reaction with its environment." [36, p. 1] Corrosion costs impact industry in many ways; one cost is from repair and replacement of parts that must be replaced due to corrosion. Another cost is time and product lost due to a work stoppage caused by equipment failure due to corrosion or maintenance required due to corrosion. Corrosion also costs money in the form of inspection and preventative maintenance.

In addition to these economic costs, there are human costs as well. Many workers have been injured or killed due to corrosion weakened steam pipes rupturing, leaking high pressure, high temperature steam into workspaces. These human costs of corrosion struck the airline industry on April 28, 1988 when an Aloha Airlines Boeing 737, flight 243, experienced a failure in a joint in the aircraft skin at 24,000 feet[2]. A large section of the aircraft skin was torn away, resulting in rapid decompression of the aircraft cabin. One flight attendant was swept overboard, presumably killed, and eight other individuals were seriously injured. The reason for the failure of the joint was determined to be fatigue cracking of a bonded, riveted joint connecting sections
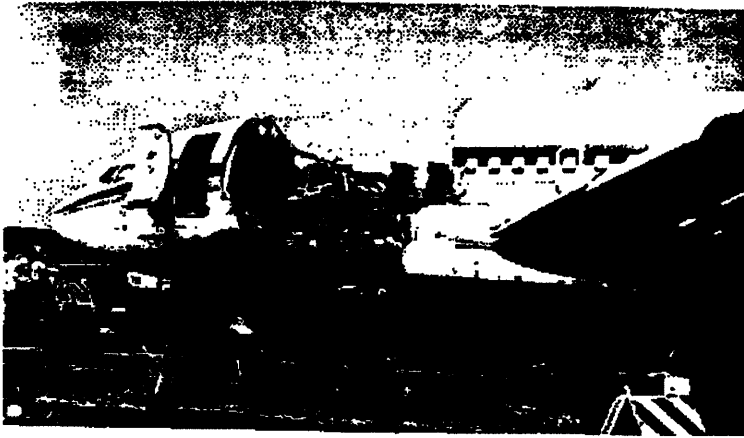
Figure 3-1: Photograph of Aloha Airlines Flight 243

of the aircraft skin. A similar accident occurred in the Republic of China in 1981, when a 737 experienced a similar explosive decompression of the cabin. The cause of the accident in China was determined to be "extensive corrosion damage in the lower fuselage structures, and at a number of locations there were corrosion penetrated through pits, holes and cracks due to intergranular corrosion and skin thinning exfoliation corrosion . . . resulting in rapid decompression . . . midair disintegration[1]."

3.2 Corrosion of Aluminum Aircraft Structures

Corrosion is an electrochemical process that damages metal through dissolution of the metal atoms. A metal atom has electrons ripped away from it by another atom which strongly attracts electrons, like oxygen. The metal atom is said to have been *oxidized* and the atom that receives the electrons is said to have been *reduced*. Through this process, metal atoms are dissolved as ions in solution, and the metal structure is weakened through material loss.

3.2.1 Corrosion Products

Professor Marcel Pourbaix pioneered a useful technique in corrosion science. He wrote down equilibrium reactions for all possible reactions the metal might undergo when it is oxidized, and determined which reactions were energetically most favorable in certain environments. These are graphically represented as regions of a two dimensional diagram where the vertical axis represents the electric potential of the metal vs. a standard cathode and the horizontal axis represents pH. The regions indicate the most stable corrosion product for that environment. Figure 3.2 shows the Pourbaix diagram for aluminum in deaerated water.

From Figure 3.2 one can see that three corrosion products are possible, Al^{3+} in solution, $Al_2O_3 : 3H_2O$, or AlO_2^-. The most common form of corrosion product is aluminum oxide hydrate, $Al_2O_3 : 3H_2O$.

3.2.2 Types of Corrosion

There are many different types of corrosion, but they can be divided into two general categories: uniform attack and localized attack. Uniform attack is characterized by uniform dissolution of material over the entire metal surface. It accounts for the greatest tonnage of material lost every year. [21, p. 11] Localized attack, while accounting for much less material loss, is of greater concern than uniform corrosion because it is much harder to predict, detect, and control. Forms of localized attack include pitting, crevice corrosion, intergranular attack, stress corrosion cracking, and corrosion fatigue cracking.

Localized forms of attack tend to have penetration rates much higher than those of uniform corrosion. This is because localized attack allows the local environment to become isolated from the rest of the electrolyte, causing corrosion products to build up and changing the concentrations of ions in the solution. Metal ions in solution
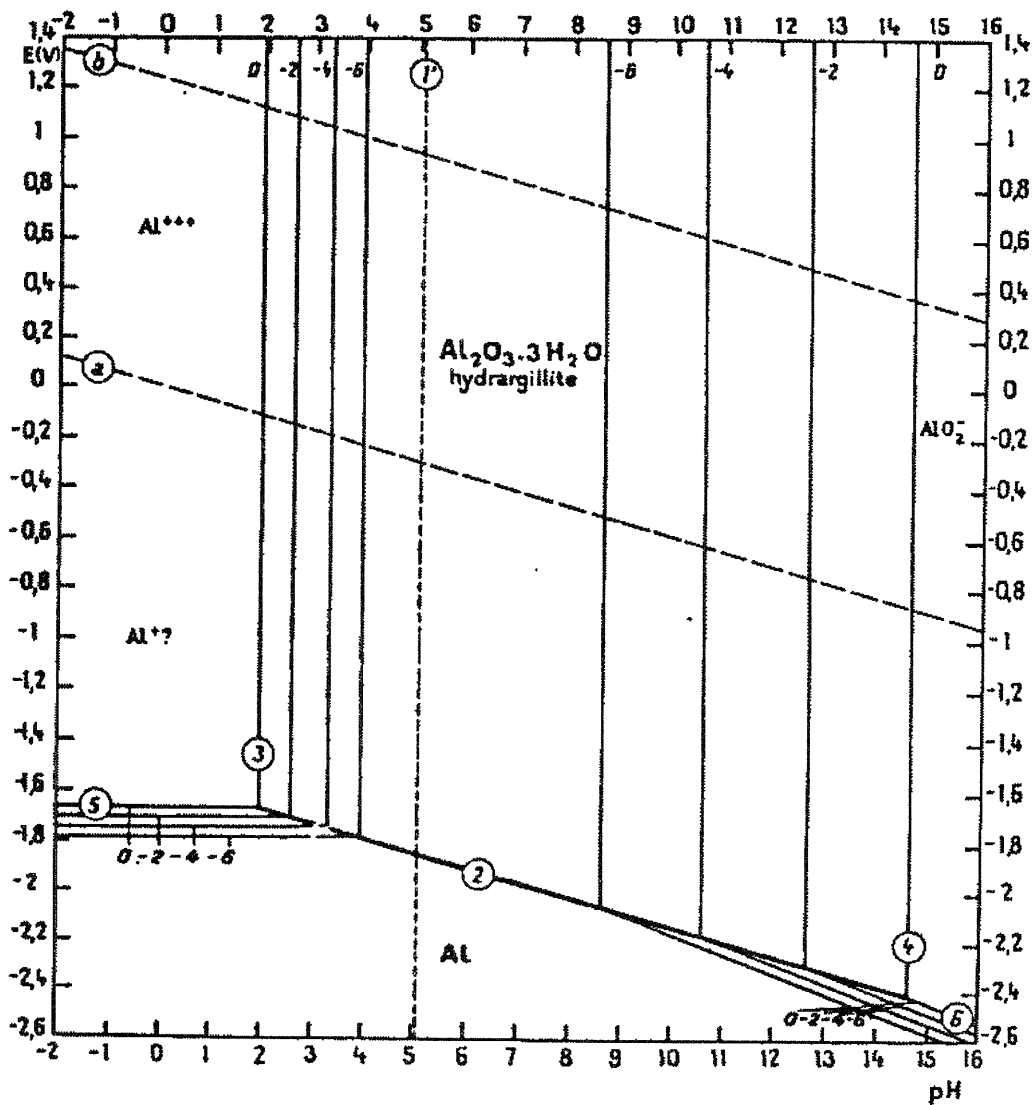
Figure 3-2: Pourbaix Diagram for Aluminum
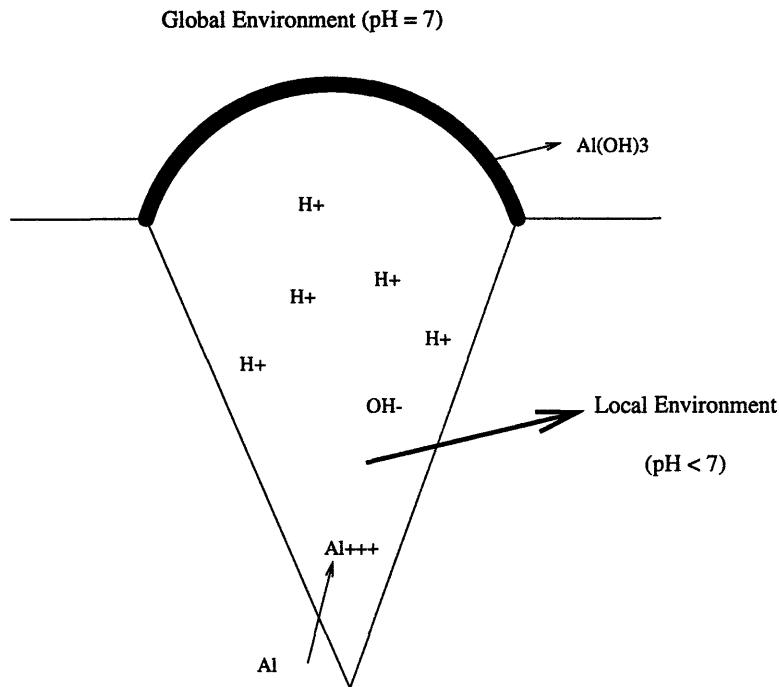
Figure 3-3: Chemistry of a Corrosive Pit

tend to precipitate out as hydroxides, lowering the pH of the local environment. The buildup of insoluble hydroxides tends to limit diffusion of hydroxide ions from the global environment into the local environment, causing the pH of the isolated environment to drop. This increasing acidity of the local environment increases the corrosion rate, putting more metal ions into solution, which precipitate out more hydroxide ions, which lowers the pH even more, continuing the cycle. This positive feedback loop accelerates the corrosion process. This effect is most pronounced at the crack tip, causing the defect to deepen at a faster rate than it widens.

The factors that control this feedback process are the solubility of the metal hydroxide, the size of the "local" environment, and the rate of diffusion of the ions in solution. Any area that allows a portion of the corrosive electrolyte to be isolated is vulnerable to this type of accelerated local attack. Some examples of vulnerable areas are cracks, scratches, crevices formed from joining two surfaces (as in a lap joint), rivets, and pits formed when corrosion resistant coatings fail locally.

Typical crack or pit sizes are in the range of 10^{-5} to 10^{-3} m across the pit opening and

may be deep enough to penetrate the entire thickness of the material. From Figure 3.3 one can see that these localized forms of corrosion will often result in the attacked regions being left packed with corrosion product, either $Al(OH)_3$ or $Al_2O_3 : 3H_2O$.

3.3 Non-Destructive Evaluation of Corrosion in Aircraft Structures

3.3.1 Benefits of NDE to the Airline Industry

The airline industry could save a great deal of money with a fast, inexpensive, reliable non-destructive inspection process to locate corrosion in aluminum structures. This would allow the airlines to catch the corrosion early and repair a small, inexpensive problem rather than a large, costly one. It would also decrease the amount of time each aircraft spent inoperable due to corrosion related problems. Airlines are very concerned with minimizing the amount of time aircraft must spend on the ground, and taking an aircraft out of service in order to repair corrosion damage is a very costly affair even if repair costs are ignored and only revenue lost due to flights not completed is considered. An effective non-destructive inspection procedure would also extend aircraft service life.

3.3.2 Aging Aircraft Concerns

We have already mentioned that it is economically advantageous to the airline industry to extend aircraft lifetimes as long as possible due to the huge capital cost of the aircraft. Twenty years ago this was not an issue of great concern because large, commercial jet aircraft fleet was relatively new. Today, however, some of the aircraft still flying are older than many of their passengers.

Different concerns exist for military aircraft. They are not required to operate

User	Total In Fleet	Total Over 20 Years Old	% Over 20 Years Old
Army			
Helicopters	8,115	5,176	64
Fixed Wing	330	179	54
Navy/Marines			
Helicopters	1,385	579	42
Fixed Wing	3,129	529	19
Air Force			
Fixed Wing	4,493	2,560	57
Total Military	17,452	9,087	52
Total Commercial	5,084	1,700	33

Table 3.1: Aging Aircraft Summary

continuously due to economic concerns like civilian aircraft. There is an additional problem, though, in that the military cannot independently determine the service lifetime of its aircraft. An excellent example is the KC-135 mid-air refueling tanker. The aircraft was brought into service in the mid 1950's, and Congress has recently voted to appropriate funds for a replacement aircraft in 2045. The Air Force has no choice but to continue operating the older aircraft past their intended lifetime. This is not an isolated example. A study in 1990 concluded that corrosion damage to U.S. Air Force aging aircraft is the most significant cost burden of any structurally related factors.[11] Table 3.1 shows the average age of various types of aircraft, both military and commercial[9].

3.3.3 Present State of Non-Destructive Inspection of Aircraft

The airline industry presently relies on two techniques, visual inspection and eddy current probes.[19] Visual inspection is a non-quantitative technique that doesn't allow for inspection of areas that an operator can't access. It is effective at detecting

more advanced corrosion, but it is difficult to see the early stages of uniform corrosion or localized forms of corrosion, such as small pits and cracks.

The eddy probe monitor is a device that relies on the fact that aluminum conducts electricity and the corrosion products of aluminum do not. The probe is a small, hand-held device that induce eddy currents in the aircraft skin. The behavior of the eddy currents allows the operator to determine the thickness of the conductor. In this way the amount of material lost to corrosion can be determined. It is an accurate technique when the instrument is handled by an experienced operator and is calibrated correctly. Drawbacks of the eddy current probe are that it is not very effective at detecting localized forms of corrosion attack such as pitting or stress corrosion cracking and that it is a very time consuming technique. Operators must literally crawl over the skin of the aircraft with the probe, which can only test a small area (on the order of square centimeters) at one time.

3.3.4 Neutron Radiography and Detection of Corrosion in Aircraft Structures

In order to determine if neutron radiography is suitable for imaging corrosion in aircraft structures, one must remember the requirements for radiography. Radiography requires that the radiation penetrates the bulk material and that the details one wishes to image has a high attenuation coefficient.

Table 3.2 shows the elemental cross section for aluminum, oxygen, and hydrogen for soft x-rays (30 keV), thermal neutrons (0.025 eV) and cold neutrons (0.005 eV).

These cross sections are easily converted into linear attenuation coefficients of

Element	X-Rays 30 keV	Thermal Neutrons .025 eV	Cold Neutrons .005 eV
Hydrogen	0.597	38.30	65
Oxygen	9.810	4.20	6.0
Aluminum	49.3	1.42	1.5

Table 3.2: Cross Sections of Various Elements for X-Rays and Neutrons in barns $(10^{-24} cm^2)$

different materials by the following formula:

$$\mu = (\Sigma_i \chi_i \sigma_i A_0) \frac{MW_i}{\rho} \qquad (3.1)$$

Where:

- Σ_i = sum over all isotope types present in material

- χ_i = mole fraction of isotope i

- μ = linear attenuation coefficient (cm^{-1})

- σ_i = atomic cross section $\left(\frac{cm^2}{atom}\right)$ of isotope i

- A_0 = Avogadro's Number = $6.02 x 10^{23} \frac{atom}{mol}$

- MW_i = molecular weight of material

- ρ = density $\frac{g}{cm^3}$ of material

Using equation 3.2, we can determine the linear attenuation coefficients of aluminum and corrosion products for soft x-rays, thermal and cold neutrons. The results are listed in table 3.3.

Table 3.4 makes it easy to see why thermal neutrons are a better choice for imaging corrosion in aluminum than x-rays. Recall from Chapter 2 that the total fluence required to image a detail of fixed size is proportional to the inverse of the square of $\delta \mu$. The corrosion products of aluminum show much larger values of $\delta \mu$ for thermal

Material	X-Ray 30 keV	Thermal Neutron 0.025 eV	Cold Neutrons 0.005 eV
Al	3.0	0.085	0.086
$Al_2O_3 : 3H_2O$	1.57	2.51	4.18
$Al(OH)_3$	1.50	2.41	4.55

Table 3.3: Linear Attenuation Coefficients for Aluminum and Corrosion Products for X-Rays and Neutrons (cm^{-1})

Material	$\frac{\delta\mu}{\mu}$ vs Aluminum		
	X-Rays	Thermal Neutrons	Cold Neutrons
Al	0	0	0
$Al_2O_3 : 3H_2O$	0.48	2.85	4.76
$Al(OH)_3$	0.50	2.73	5.19

Table 3.4: $\frac{\delta\mu}{\mu}$ for Corrosion Products in Aluminum for Different Radiation Types

and cold neutrons than for x-rays, making neutrons a better choice for imaging corrosion in aluminum structures.

Chapter 4

Detector Configuration and Characteristics

The detector used in this work consisted of commercially available elements. No expensive, custom made parts were required. This was an important concern because the purpose of this work is to show that neutron radiography is a practical technique for use in the field. Exotic and delicate materials are not suited for field work. After considering the available detector types, we chose a scintillator coupled to a CCD camera because it is a simple, relatively inexpensive detector with low noise and high spatial resolution.

4.1 Theory of Position Sensitive Neutron Detection

Direct spatially localized detection of neutrons is a difficult task. Most position sensitive neutron detectors rely on a neutron converter, which converts the neutron into a more easily detected secondary radiation, such as a photon, electron, or alpha particle. The detector used actually detects this secondary radiation.

When choosing a converter-detector pair, one must consider a number of factors. Neutron converters must balance efficiency with spatial resolution and output of secondary radiation. One must also match the secondary radiation produced in the converter to the proper type of detector. By choosing the appropriate balance of these factors, one can maximize the detector response per unit neutron flux.

4.1.1 Gas Detectors

Gas neutron detectors rely on a gas as a neutron converter. A gas with a high neutron cross section is chosen, such as boron trifluoride (BF_3) or helium (He^3). An incident neutron strikes a gas molecule and ionizes it. A high voltage is placed across the gas chamber, accelerating the liberated electron and the ion towards the electrodes. As the particles are accelerated towards the electrodes, they gain energy and collide with other gas molecules, causing additional ionization. In this way a cascade of electrons and positive ions is formed, and a measurable charge is collected at the electrode. This measurable charge is the detector output signal.[10]

These types of detectors have been used in a position sensitive manner in two ways. One method is a discreet element gas detector, which is simply many small gas detectors placed in an array. Because each detector has an individual output, it is easy to determine where the neutron was detected. These detectors are expensive, require many outputs to be monitored, are easily saturated, and have very poor spatial resolution. They are not suitable for radiography.

A second gas position sensitive detector is a multiwire gas detector. This is a single gas chamber with a grid of wire electrodes. Because the charge is created and collected in a small area around the neutron interaction site, the electrode nearest the interaction site will collect the most charge. The neutron detection site can be found by using the vertical and horizontal wire with the largest response. These detectors are also expensive, delicate, and have poor spatial resolution, making them unsuitable

for radiography.

4.1.2 Scintillator Methods

Scintillator detectors are materials that have two characteristics. First, they have molecules with high neutron cross sections to absorb the energy of incident neutrons. Second, they have special added molecules that accept energy from nuclei excited by an incident neutron and release that excitation energy as a visible light photon. Thus, scintillators are neutron converters with visible light photons as the secondary radiation. The photons are converted into an output signal using a photomultiplier tube.

Like gas detectors, they have been used in a number of ways as position sensitive neutron detectors. Similar to a discreet element gas detector, as discreet element scintillator detector consists of many individual scintillator detectors in an array, each with an individual output. The detectors are expensive and have poor spatial resolution.

The scintillator detector known as the Anger Camera is similar to a multi-wire gas detector. It consists of a single scintillator with many phototubes behind it. The neutron detection site is found by taking a weighted sum of the output signals from the phototubes. These detectors have poor spatial resolution and have problems with being saturated..

4.1.3 Film Methods

Film methods rely on materials with high neutron cross sections that undergo an (n,γ) reaction, such as gadolinium. A thin foil is coupled to a photographic emulsion screen. The photons produced in the film are then detected in the photographic plate.

The detector response is measured by the darkening of the photographic plate.

These detectors have excellent spatial resolution, but have other problems. One is that the response is not linear with detector flux. This means that the imaging system is not linear, as defined in chapter 2, and cannot be analyzed using the simplifications we used for a linear, stationary system.

4.2   Detector Configuration

The detector used for this work consisted of a commercially available scintillator screen whose output was directed and focused onto a charge-coupled device used for imaging purposes. The entire set-up was encased in a light tight aluminum box to prevent noise from external light affecting the detector. This aluminum box was covered with 5.1E-2 cm thick cadmium sheeting on three sides to reduce the number of thermal neutrons that reached the screen after scattering from the sides or above the detector. The detector is shown in Figure 4.1.

4.3   Scintillator

The scintillator screen used was a Nuclear Enterprises NE-426 screen. It uses lithium flouride with a zinc sulfide actuator. The lithium flouride is enriched in Li^6, which has a very high thermal neutron absorption coefficient of 945 barns. The Li^6 undergoes an (n, α) reaction, liberating a 2.05 MeV alpha particle. The energetic alpha particles then collide with zinc sulfide molecules, transferring energy in the collision. These energetic zinc sulfide molecules then relax, emitting visible light photons in order to lose the energy the gained as the result of the collisions with alpha particles.

There are two important factors to consider that control the light output of the
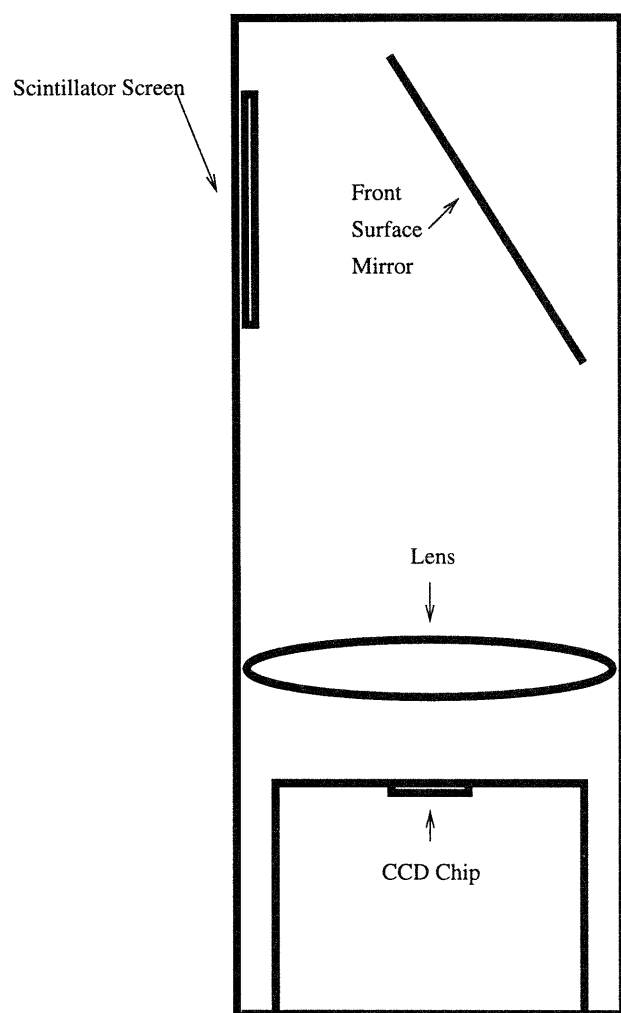
Figure 4-1: Components of Imaging System

screen. The first factor is the fraction of incident neutrons that react in the screen. This neutron efficiency is a function of two variables, the thickness of the screen and the density of Li^6 in the screen. Spowart investigated the effect of these two factors on the light output of the scintillator screen.[33]

The NE-426 screen used was 0.25 mm. Spowart investigated screens of thicknesses from 0.05 mm to 1mm and found that the optimal thickness for radiography was 0.25 mm. The thickness could be increased in order to increase the neutron efficiency, but at the expense of both light output and spatial resolution. Light output for a thicker screen is slightly lower due to self absorption and spatial resolution is decreased. Screens thinner than 0.25 mm had problems due to non-uniform distribution if the lithium flouride.

The NE-426 screen used has approximately 15% neutron efficiency. It has one part lithium flouride and four parts zinc sulfide by weight. We chose this value because Spowart investigated the light output of scintillator screens with ZnS/Li^6 weight ratios from about 0.1 to 6 and found that the peak light output is obtained for a ZnS/Li^6 weight ratio of four. The light output measured by Spowart for this screen was $1.7x10^5$ photons per detected neutron. Because photon from the screen is isotropic, only half of these photons, or 8.5E4 photons per detected neutron, were produced in a direction such that they were directed onto the CCD camera.

4.4 Camera

The camera used to image the scintillator screen was a Princeton Instruments TE/CCD-1242E. The CCD is an EEV 05-30 with 1242x1152 pixels. The chip size is 28 mm x 26 mm, for a pixel size of 22.5 μm x 22.5 μm. The camera is interfaced via a Princeton Instruments ST-138 controller which can be read out at high speed (12 bits, 1 Mhz) or low speed (15 bits, 430 kHz). The ST-138 also controls the thermoelectric camera
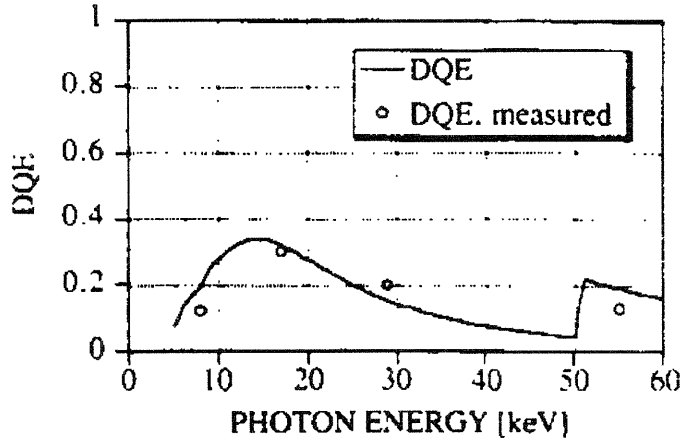
Figure 4-2: CCD Efficiency vs Photon Energy

cooling mechanism, which can be run air cooled or with circulating chilled water.

4.4.1 Efficiency of CCD

The photon efficiency of the CCD depends on the photon energy. Koch measured the efficiency of the CCD vs photon energy and found that the peak efficiency was about 30% at photon wavelengths of 550 nm (See Figure 4.2). [24] Because the NE-426 photon emission spectrum has it's peak below this wavelength, copper (Cu) was added to the scintillator to shift the peak emission towards the area of highest CCD efficiency. The efficiency changes relatively slowly with photon energy, however, so we assumed a total efficiency of approximately 30%.[27]

4.4.2 CCD Noise Characteristics

The noise characteristics of CCD detectors have been investigated by Schempp and Toker.[28] They determined the noise in the CCD signal comes from three sources: background photon noise, dark current, and readout noise. The total noise is given by the following expression:

46

$$\sqrt{(P + B)tQ_e + Dt + N_r{}^2} \qquad (4.1)$$

where:

- P = signal photon flux

- B = background photon flux

- t = integration time

- Q_e = detector efficiency

- D = dark current

- N_r = readout noise

Background Noise

The first source, background photon noise, is easy to understand. It is fluctuations produced in the CCD output due to the statistical variation in background photon flux. Because our detector is in a light tight box, there is no visible light background radiation. There is, however, background radiation in the form of x-rays and gamma rays produced by the accelerator itself and in the beryllium target used for neutron production.

In order to determine the effects of this x-ray flux, we exposed the system to identical neutron fluxes in two situations; first the camera was left bare and the mean pixel response was measured. Then camera was surrounded by lead bricks two inches thick and the measurement was repeated. After each measurement of camera response, the neutron flux was measured using a GS-20 thermal neutron scintillator, which is a glass scintillator that also uses the Li^6 thermal neutron reaction to detect neutrons. This GS-20 response was used to normalize the CCD response, as the neutron production rate may vary slightly even with the same accelerator settings. The following table contains the raw data collected. Each pixel in the image represents a square in real

47

Time (m)	Mean Pixel Level (ADC Counts)			
	9.1 uA w Pb	9.1 uA w/o Pb	40 uA w Pb	40 uA w/o Pb
.5	127.07	170.00	231.02	406.56
5	621.78	1045.40	1683.60	3360.89
10	1172.67	2003.64	3299.82	6674.59
20	2271.47	3947.58	6569.02	13434.03
30	3364.62	–	9885.27	20133.15
GS-20 Counts Over 5 m	56275	52123	281319	284023

Table 4.1: Average Pixel Exposure, Shielded and Unshielded CCD

space 1.6E-2 cm on each side.

The data from the previous table is contained in the following two plots. The horizontal axis represents the time of exposure and the vertical axis represents the mean pixel value divided by the number of counts per second measured by the GS-20 detector. This was done to normalize the values for slight fluctuations in neutron flux.

It is easy to see from these plots that the CCD is sensitive to the x-ray flux produced in the accelerator and target, but this background noise can be controlled by placing lead around the CCD camera. It is difficult to generate a specific numerical value for B because the x-ray flux produced depend on the accelerator settings and current. Thus, B is different for different accelerator settings and current. To reduce this x-ray contribution to the background level, B, the CCD was surrounded on all sides by 2" of lead. Additionally, We placed a .25" thick lead sheet at the base of the cement brick and polyethylene moderator structure surrounding the neutron source.

We did not generate a spectrum of the x-rays and gamma rays that might cause this background noise in the CCD. The specifics of the photon spectrum were of no concern to us, we simply wanted to know if the detector performance was improved by shielding the CCD with lead, and the data above shows that convincingly.
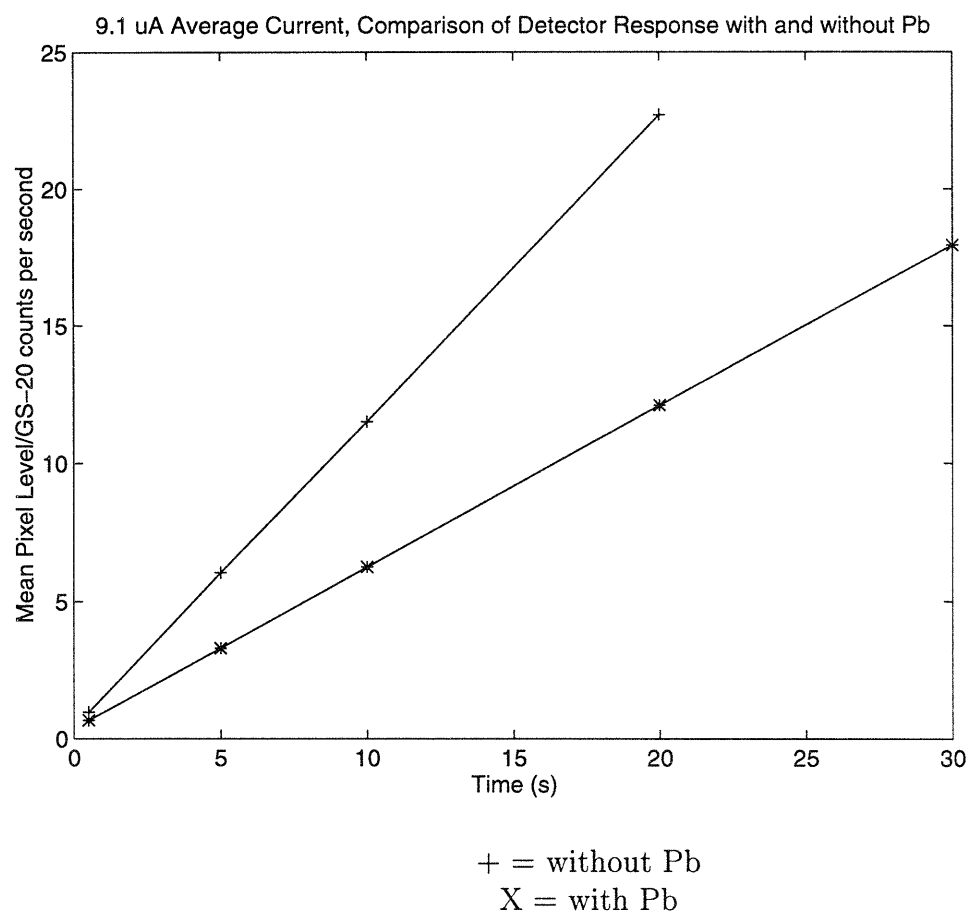
Figure 4-3: Mean Pixel Level, Shielded and Unshielded CCD, 9.1 uA Beam Current
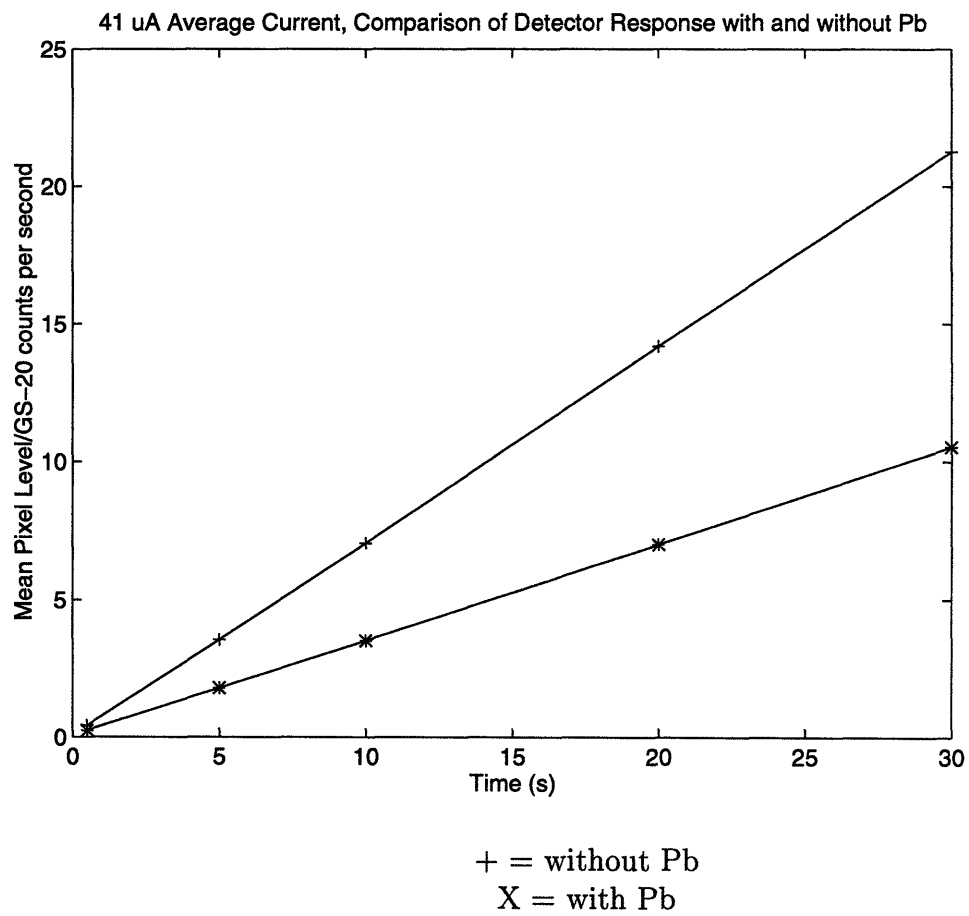
Figure 4-4: Mean Pixel Level, Shielded and Unshielded CCD, 40.0 uA Beam Current

Time (s)	Mean Pixel Level (A-D counts)	Std. Dev. (A-D counts)
10	87.12	2.33
30	104.92	5.02
45	119.79	7.24
60	133.53	9.47
90	162.38	13.96
120	191.93	18.52

Table 4.2: Dark Current Data

Dark Current Noise

Understanding the second and third noise sources requires a very basic understanding of how CCD detectors operate. They can be thought of as a grid of capacitive wells that trap electrons liberated as a photon passes through the semiconductor chip, exciting electrons into the conduction band. These "wells" are then read out sequentially. Dark current noise that part of the output signal that is due to electrons that are thermally excited into the conduction band and then collected in a capacitive well. It obviously depends on the temperature of the CCD chip. for this reason, we kept the CCD chip cooled to -50 degrees Celsius with a water cooled thermoelectric Peltier device.

We measured the dark current noise by taking exposures for different times and measuring the mean pixel level. The results are shown in the table and plot below.

The dark current is equivalent to the slope of this curve, which is 0.9547 ADC per second per pixel. An ADC is an analog to digital count, and is simply a measurement of the number of electrons collected per pixel "well".

Readout Noise

The readout noise is caused by the method of reading each pixel "well" out the the ST-138 controller. The contents of each "well" are transferred from pixel to pixel
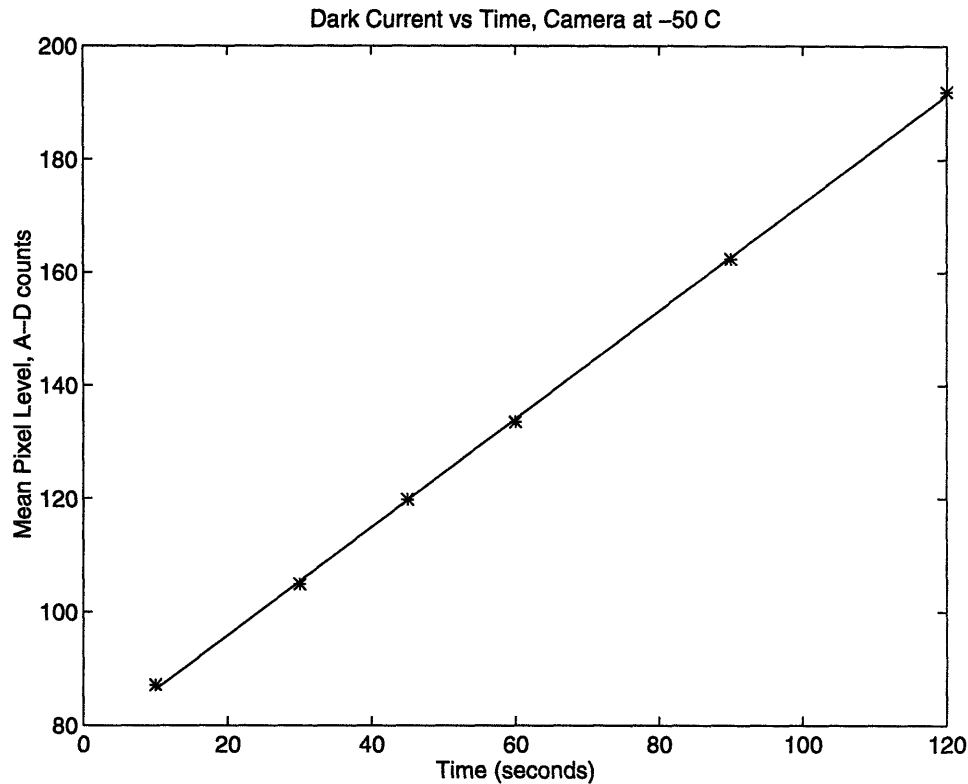
Figure 4-5: Dark Current Exposure vs. Time

as successive pixel "wells" are read out. This process can be thought of as a bucket brigade, where the contents of each bucket are poured into the next as the final bucket is emptied (i.e. read out). The readout noise is the variation in the signal produced due to this transfer process. Because this noise is a factor of the way the CCD is read out and not any factors depending on time, it is independent of time. In the plot above, the readout noise can be found from extrapolating the data back to time zero and finding the ADC level. The readout noise for our system is 76.7906 ADC per pixel.

Fixed Pattern Noise

Fixed pattern noise is noise that is introduced into the signal due to imperfections in the CCD chip itself. These imperfections occur at a fixed location on the CCD chip, hence the name fixed pattern noise. Fixed pattern noise does not occur in the equation for CCD noise because it is very easy to eliminate. It can be eliminated

by subtracting two images taken over the same exposure period. The "fixed pattern noise" is identical in both images, so by subtracting them we remove the noise. The IPLab imaging software[12] was able to subtract two images from each other, pixel by pixel. In this way the fixed pattern noise was eliminated.

4.4.3 Camera Gain

The detector gain is the number of analog to digital counts (ADC) produced per electron. If n_e is the number of electrons liberated in the CCD pixel, then the ADC value of the pixel is given by:

$$A_1 = G n_{e1} \tag{4.2}$$

$$A_2 = G n_{e2} \tag{4.3}$$

where A is the ADC signal and G is the detector gain. The subscripts 1 and 2 refer to 2 different exposures.

We can write n_e as the sum of three parts:

$$n_{e1} = n_{sig1} + n_{read1} + n_{fp1} \tag{4.4}$$

$$n_{e2} = n_{sig2} + n_{read2} + n_{fp2} \tag{4.5}$$

where n_{sig} is the sum of all signals obeying Poisson Statistics (including the photon signal, the dark current and background noise) and n_{read} is the readout noise portion of the signal and n_{fp} is the fixed pattern portion of the signal.

Taking the difference between the two pictures pixel by pixel:

$$A_1 - A_2 = G(n_{e1} - n_{e2}) \tag{4.6}$$

$$A_1 - A_2 = G[(n_{sig1} - n_{sig2}) + (n_{read1} - n_{read2})] \qquad (4.7)$$

Notice that $n_{fp1} = n_{fp2}$ so these terms cancel from the difference image.

The variance in the difference image can be found:

$$\sigma_{A_{1-2}}{}^2 = G^2[(\sigma_{sig1}{}^2 + \sigma_{sig2}{}^2) + (\sigma_{read1}{}^2 + \sigma_{read2}{}^2)] \qquad (4.8)$$

Recall that sig1 and sig2 represented the portion of the signals that obeyed Poisson statistics. We can replace $\sigma_{sigX}{}^2$ with n_{sigX}.

$$\sigma_{A_{1-2}}{}^2 = G^2[(n_{sig1} + n_{sig2}) + (\sigma_{read1}{}^2 + \sigma_{read2}{}^2)] \qquad (4.9)$$

If the two pictures used to form the difference image were dark current exposures under identical conditions for identical times, then $n_{sig1} = n_{sig2} = n_{sig}$ and $\sigma_{read1}{}^2 = \sigma_{read2}{}^2 = \sigma_{read}{}^2$. This allows us to simplify:

$$\sigma_{A_{1-2}}{}^2 = G^2(2n_{sig} + 2\sigma_{read1}{}^2) \qquad (4.10)$$

If the read noise and fixed pattern noise are small compared to the signal (a good assumption for our system) the we can rewrite:

$$G^2 n_{sig} = G(G n_{sig}) = G\overline{A} \qquad (4.11)$$

Where $\overline{A}$ is the mean pixel value for either of the exposures. This allows us to write the following:

$$\sigma_{A_{1-2}}{}^2 = 2G\overline{A} + 2G^2\sigma_{read}{}^2 \qquad (4.12)$$

Thus a plot of the variance of the difference of two dark current images vs the average pixel level of the dark current images will yield a straight line of slope $2G$ with an intercept of $2G^2\sigma_{read}{}^2$.

Time (min)	Mean Pixel Level (ADC)	Variance of Difference Image (ADC^2)
1	142.28	36.605
2	210.63	49.4209
3	279.25	62.8849
4	348.58	78.3225
5	418.16	87.2356
6	485.86	100.6009
7	555.23	115.7776
9	694.38	149.5729
10	763.42	150.0625

Table 4.3: Gain Curve Data Points

The following data was obtained for the CCD cooled to -50 C and readout in the fast readout (15 bit) mode:

After curvefitting the above data points, the line of best fit was found to be:

$$\sigma_{A_{1-2}}{}^2 = 0.1912\overline{A} + 9.4664 \tag{4.13}$$

Thus, 2 G = 0.1912 A-D counts per electron, and G = 0.0956 counts per electron, or 10.5 electrons per count.

4.5   Detector Response

Two quantities that it is useful to know are what the minimum neutron flux required and the maximum neutron fluence allowed are. The minimum neutron flux is set by the noise characteristics of the camera system. The flux must be large enough that the signal generated by the scintillator screen in the CCD is greater than the noise generated in the CCD. The maximum neutron fluence is set by the dynamic range of the CCD, or the depth of the capacitive "wells". Both of these quantities require that we know the CCD response per neutron.
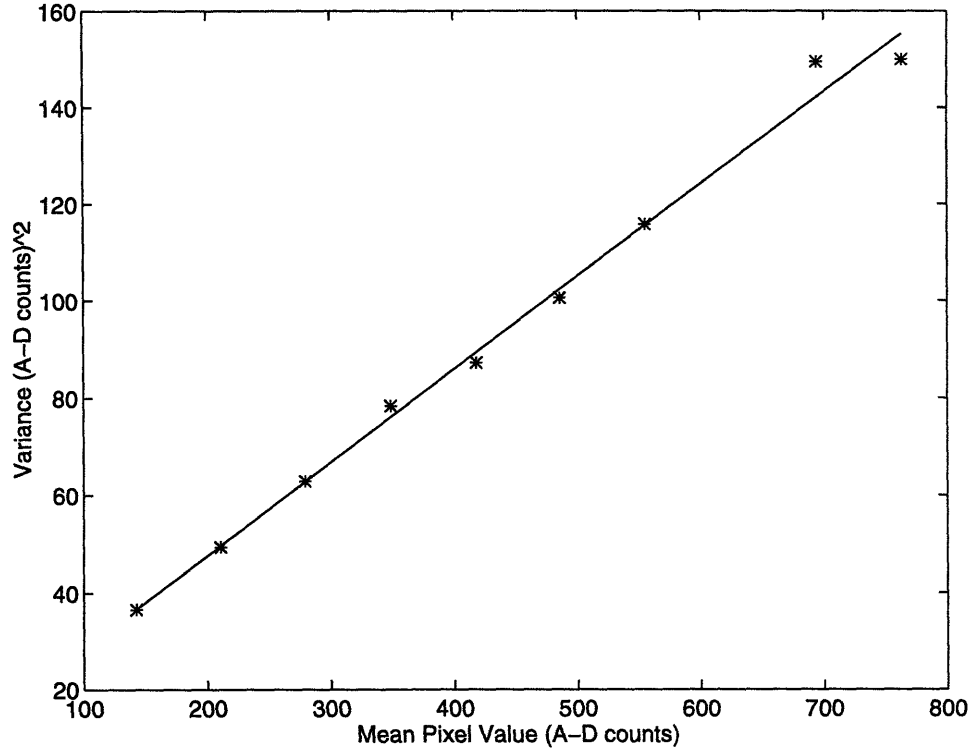
Figure 4-6: Camera Gain Curve

The number of photons per unit area detected in the CCD chip can be expressed by:

$$\phi_\gamma = \Phi \eta n_\gamma m^2 \chi Q_e \tag{4.14}$$

where:

- ϕ_γ = number of photons detected in CCD per unit area.

- Φ = total neutron fluence (neutrons/cm^2)

- η = scintillator screen neutron efficiency

- n_γ = number of photons produced per detected neutron

- m = minification ratio $(A_{object}/A_{image} = m^2)$

- χ = factor accounting for light lost to to optical system

- Q_e = CCD detector quantum efficiency (electrons/incident photon)

56

The factor of m^2 is to account for the decrease in image size as it passes through the lens. The photons are concentrated into a smaller area by the lens, so the detected photon fluence is higher by a factor of m^2.

The fraction of light that is captured by a lens from a scintillator screen is given for small angles by:

$$\chi = \frac{\eta_o}{(2F(m+1))^2} \tag{4.15}$$

where:

- χ = fraction of light captured by lens system

- η_o = fraction of light that passes through lens

- F = f number of the lens

Using this expression for χ and simplifying we obtain:

$$\phi_\gamma = \frac{\Phi \eta n_\gamma Q_e \eta_o}{4F^2} \frac{m^2}{(m+1)^2} \tag{4.16}$$

Our system had the following characteristics:

- $\eta = 0.15$

- $n_\gamma = 8.5E4$

- $Q_e = 0.30$

- $\eta_o = 0.80$

- F = 0.9

- m = 7

Which gives a value of 723Φ electrons liberated per unit area. This factor already accounts for the minification of the image, therefore if Φ is measured in neutrons per

square centimeter then the number of electrons liberated is 723Φ electrons per square centimeter. Each CCD pixel is 22.5E-4 cm x 22.5E-4 cm. Using this to conversion factor we determine that an incident neutron fluence of Φ neutrons per square centimeter will liberate 4.38E-3Φ electrons per pixel. By multiplying this factor by the system gain, which we determined earlier to be 0.0956 counts per electron, we can find the ADC value per pixel for a given neutron fluence of Φ neutrons per square centimeter 4.19E-4Φ counts per pixel.

These conversion factors also work for incident neutron flux as well as fluence. Using this we can convert the neutron flux that is required to overcome the inherent noise of the system. The dark current for the CCD cooled to -50 degrees Celsius was determined to be 0.9547 ADC per pixel per second (see section on CCD Dark Current). In order for the neutron signal to overcome this dark current noise, we must have:

$$4.19E - 4\phi\frac{ADC}{pixels} > 0.9547\frac{ADC}{pixels} \tag{4.17}$$

$$\phi > 2.28E3\frac{n}{cm^2s} \tag{4.18}$$

We have used ϕ to represent the neutron flux, as opposed to Φ which represents the neutron fluence (time integrated flux). Thus, our minimal thermal neutron flux is $2.28E3\frac{n}{cm^2s}$.

We can also determine our maximum allowable fluence. The maximum signal our CCD is capable of reading is 15 bits, or 2^{15} ADC per pixel.

$$4.19x10^{-4}\Phi_{max} = 2^{15} \tag{4.19}$$

$$\Phi_{max} = 7.82E6\frac{n}{cm^2} \tag{4.20}$$

The maximum fluence allowed for our system is 7.82E6 neutrons per square cen-

58

timeter. Any neutron fluence above this value saturates the detector and the response in non-linear.

4.5.1 Dynamic Range

The dynamic range of the system is defined as the ratio of the maximum usable signal to the readout noise level. Our system has a maximum useable signal of 15 bits, or 32,768 ADC. The readout noise of our CCD at -50 degrees celsius is 76.79 ADC. Thus the dynamic range is 426.72.

4.6 Spatial Resolution of Imaging System

In chapter 2 we discussed the concepts of the point spread function, the edge response function, and the line response function. We showed that the line response function could be derived from the edge response function.

Shuanghi Shi found the line response function for our system during her thesis work. [29] The line response function was found by taking a radiograph of an "edge" formed by a material that was opaque to thermal neutrons. This can be done using a sheet of cadmium, which has a huge thermal neutron cross section. Two measurements were performed. One was the bare system with no collimation. The next was the system using a collimator constructed from aluminum strips 5 cm wide. The strips were coated with latex paint that had boron carbide powder mixed in with it (6 g of B_4C to 30 cc paint). This paint was then applied to the aluminum strips. The strips were then stacked approximately 1 cm apart. One set of strips was stacked horizontally, the other vertically, resulting in a L/D value of about 5.

Once this edge image is formed, the average pixel value in each column was calculated. Next, the first differences of this string of column averages was computed. This
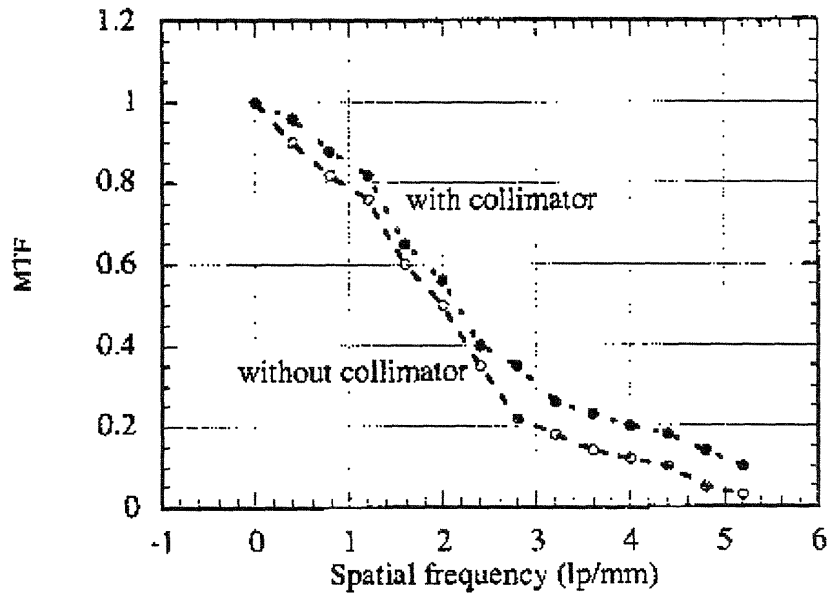
Figure 4-7: MTF of Imaging System

is analogous to taking the first derivative of the edge response function. Once the derivation has been completed, the one dimensional Fourier Transform of the data is performed. This Fourier Transform is then normalized to have a value of 1 at zero frequency. Finally, the modulus (magnitude) of the Fourier transform is plotted. This modulus of the Fourier transform is what we refer to as the line response function, or modulus transfer function.

Chapter 5

Neutron Source

5.1 Overview of Types of Neutron Sources

There are three types of neutron sources: fission reactors, accelerator sources, and isotope sources, listed in decreasing order of cost, complexity, and strength. Neutron sources have been a limiting factor in neutron radiography. Until recently, reactors were the only source of neutrons intense enough to do neutron radiography in a practical amount of time.

Reviewing the chapter on the theory of radiography shows that good neutron source characteristics are an intense source of well collimated, thermal neutrons. Reviewing the information on neutron detection, one can see that it is also desirable to have a source that has minimal photon production. Most neutron detectors are sensitive to photons, so any x-rays or gamma rays produced by the source add to the noise of the image.

5.1.1 Reactor Sources

Reactor sources are by far the strongest, most well collimated, and certainly the most expensive and complex neutron sources for thermal neutron radiography. They pro-

vide a thermal neutron flux of up to $10^8 \frac{n}{cm^2s}$ with L/D ratios up to 250, offering collimation that is much better than either of the other two types of source. Figure 5.1 shows a comparison of neutron source strength for different collimator L/D values.

5.1.2 Accelerator Sources

Accelerator sources are important because they offer a portable neutron source that is stronger than a radioisotope source. Portable sources are important in widening the range of applications of neutron radiography. Accelerator neutron sources accelerate charged particles to cause a nuclear reaction that generates neutrons as a product. Some typical reactions are:[18]

- D + D = He + n + 3.28 MeV

- T + D = He + n + 17.6 MeV

- Be + γ = 2 He + n - 1.67 MeV

- Be + H = B + n + 1.85 MeV

- Be + D = B + n + 4.35 MeV

Accelerator sources must be chosen to maximize the thermal neutron flux. One consideration is the cross section for the desired reaction. This can be thought of in terms of neutrons produced per unit of accelerated particles. This factor is a function of the energy of the incident particle. Figure 5.2 shows the neutron yeild for various reactions as a function of incident energy.

Another factor to consider when choosing an accelerator neutron source is how much power the target must absorb. If one were to consider Figure 5.2 alone, without considering thermal effects, one would decide to maximize neutron yeild by using high energy protons striking lithium at high currents. However, 1 milliampere of 6 MeV protons would put over six kilowatts of energy into the lithium target. If the
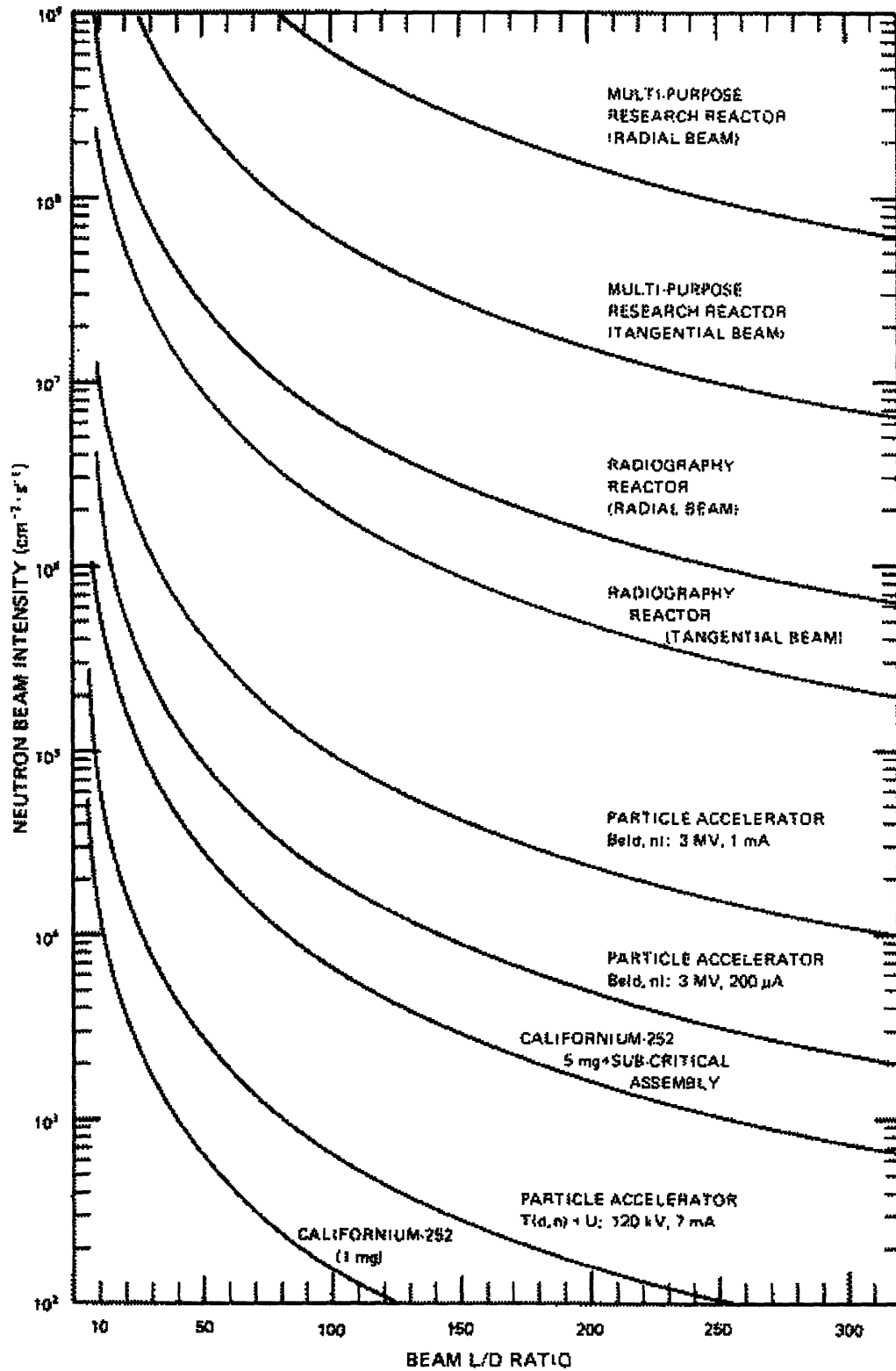
Figure 5-1: Comparison of Neutron Source Strengths
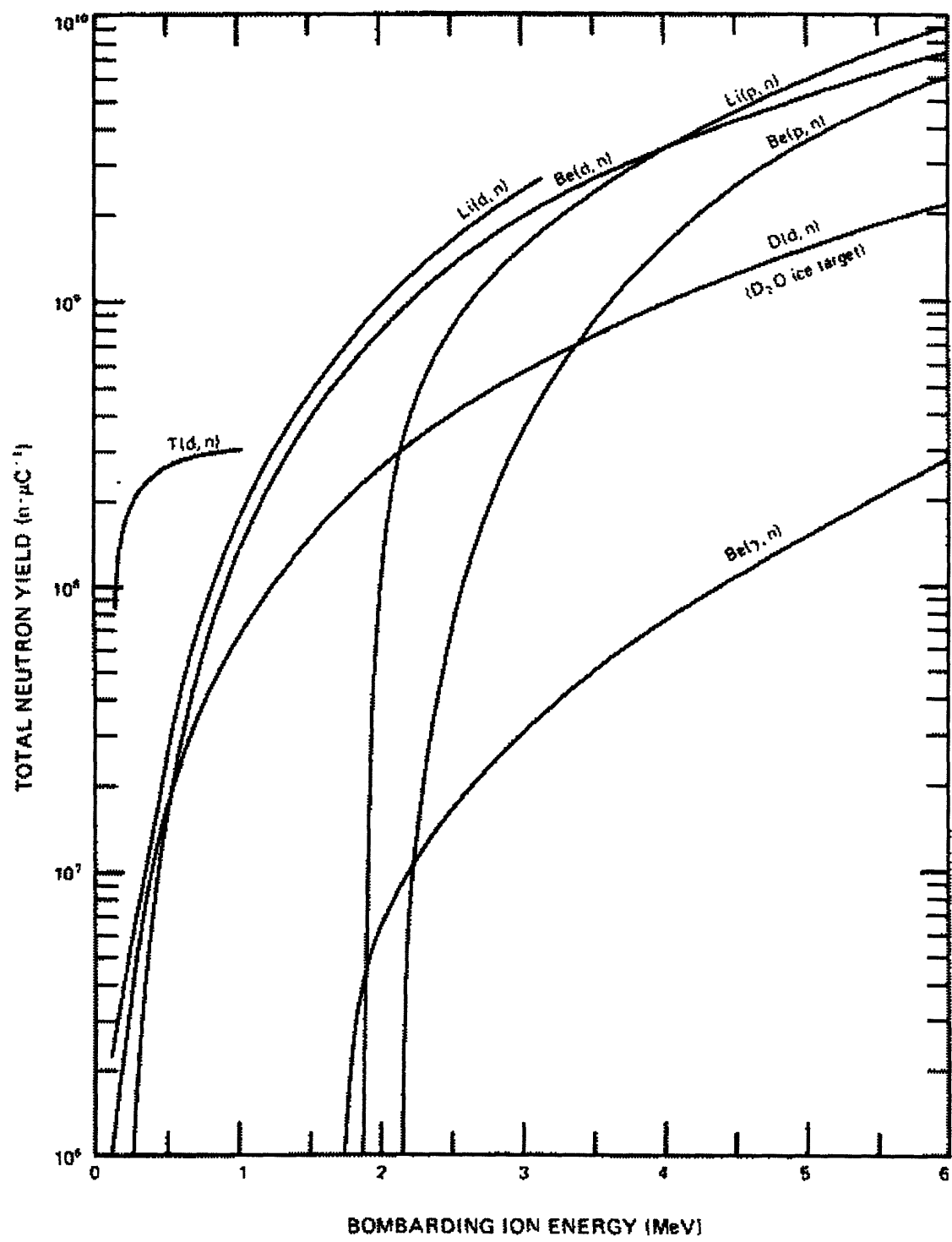
Figure 5-2: Neutron Yeild for Various Reactions vs Incident Energy

Isotope	Reaction	Neutron Yeild (n/s)		γ dose rate
		per Curie	per g	$\frac{R}{h} per 10^8 \frac{n}{s}$
Pu-238	$\alpha - n$	2.3E6	4.1E7	negligible
Cm-242	$\alpha - n$	2.5E6	8.5E9	0.04
Am-241	$\alpha - n$	2.2E6	7.0E6	0.1
Cf-252	Fission	4.3E9	2.3E12	0.007

Table 5.1: Isotope Neutron Source Characteristics

heat is not removed effectively, the charged particle beam can actually melt the target.

Also important when choosing an accelerator source is the energy distribution of the neutrons produced. Because higher energy neutrons show less of a variation of attenuation coefficient between isotopes, radiography neutron sources need low energy neutrons. The higher the energy of the neutrons that are produced in the target, the more moderation is required.

5.1.3 Isotope Sources

Isotope neutron sources are sources of isotopes which are unstable and undergo a radioactive decay that involves the production of neutrons. Most of these sources involve an isotope that decays to produce an alpha particle coupled to a sample of beryllium. The beryllium undergoes the reaction:

$$Be + \alpha = n + C \tag{5.1}$$

Typical alpha emitters used are Americium, Californium, and Plutionium. Another type of isotope source is Cf^{252}, which undergoes spontaneous fission. Table 5.1 lists some typical isotope sources and their characteristics. [18]

65

5.2 Radiofrequency Quadrupole Accelerators

5.2.1 Theory

Radiofrequency quadrupole accelerators (RFQs) were developed in the USSR by Teplyakov and Kapchinskii in 1970.[34] In the years since it's invention it has become the dominant form of low energy ion linear accelerator because RFQs have the advantage of being compact and having a high efficiency with low requirements for injection energy.

RFQs are basically a focusing structure with acceleration added as a perturbation. The perturbed quadrupole produces both focusing and acceleration. This is much improved over other types of linear accelerators which impose focusing fields on existing accelerating fields.

5.2.2 Focusing

The quadrupole is established by placing a radiofrequency electric signal across four vanes or rods. This establishes a quadrupole which varies in time and space, as illustrated in Figure 5.3. The charged particles pass through the alternating quadrupoles, which cause alternate focusing and defocusing in the plane perpendicular to the beam direction. This alternating focusing and defocusing quadrupoles has long been used for a net focusing effect.

The rods or vanes are scalloped in such a way that part of the electric field created by the quadrupole established between the vanes has a component along the beam axis. This longitudinal electric field is what provides the beam acceleration and bunching.
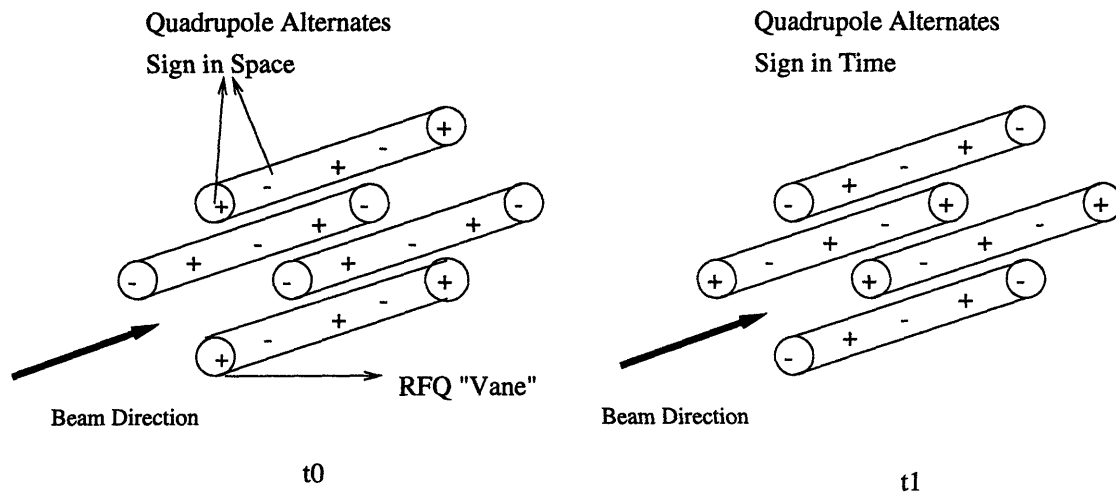
Figure 5-3: Time and Space Variation of Electric Quadrupole
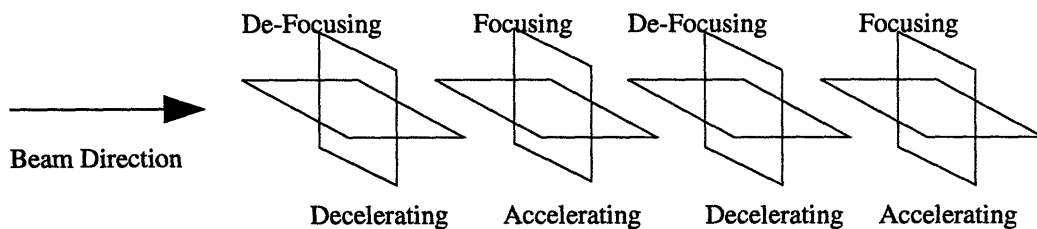
Figure 5-4: Alternating Focusing and De-Focusing Fields

Bunching

In the same way that the radiofrequency power causes alternate focusing and defocusing planes perpendicular to the beam direction, the time and space variation of the radiofrequency power applied to the vanes causes portions of the beam to be accelerated and portions of the beam to be decellerated. Rather than being a negative aspect of the RFQ, this is one of it's best advantages. It causes the beam to become efficiently gathered into packets at the proper frequency. Figure 5.4 shows how the fields alternate in space.

Once can see how the beam is bunched as it is accelerated by examining Figures 5.5 and 5.6. Figure 5.5 shows the component of the electric quadrupole perpendicular to the beam axis. This is the component of the quadrupole that provides focusing. Figure 5.6 shows the component of the quadrupole along the beam axis. This is the
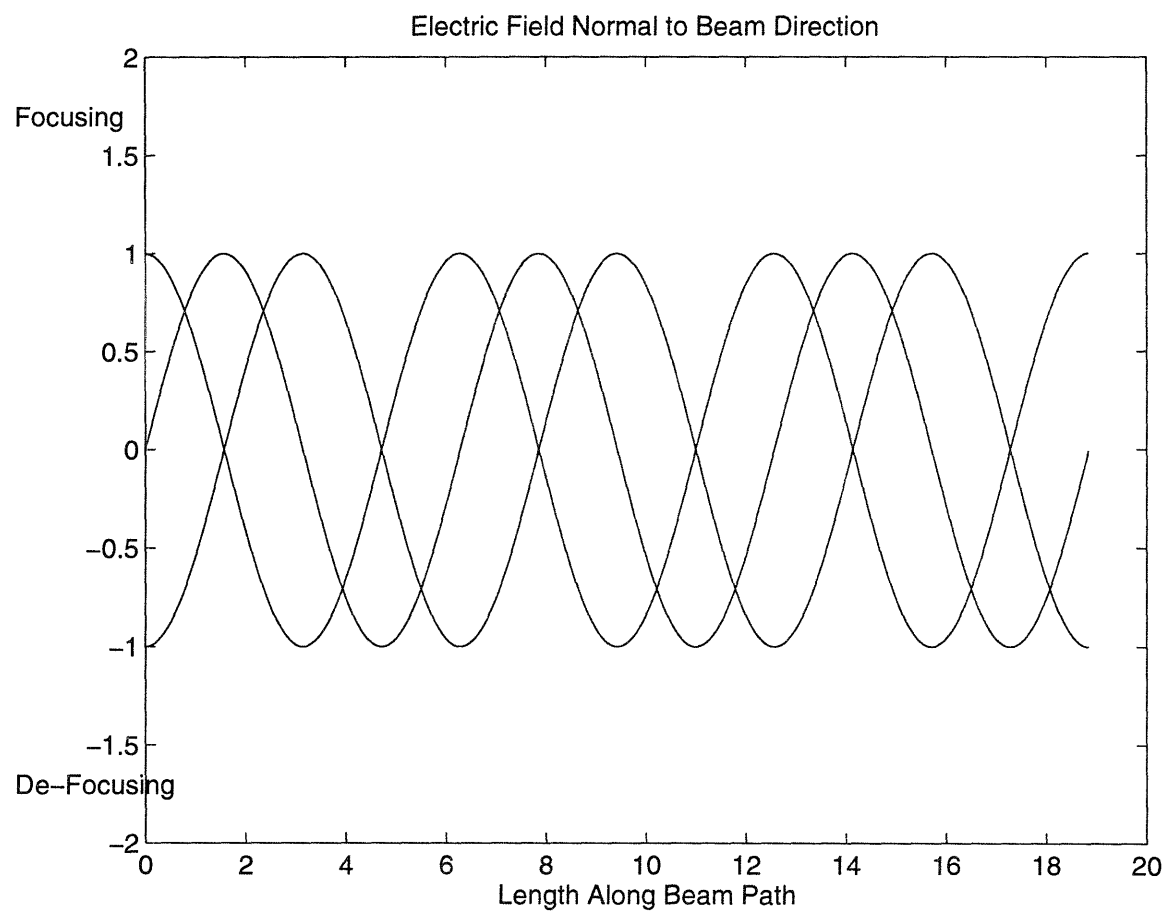
Figure 5-5: Electric Field Normal to Beam Direction
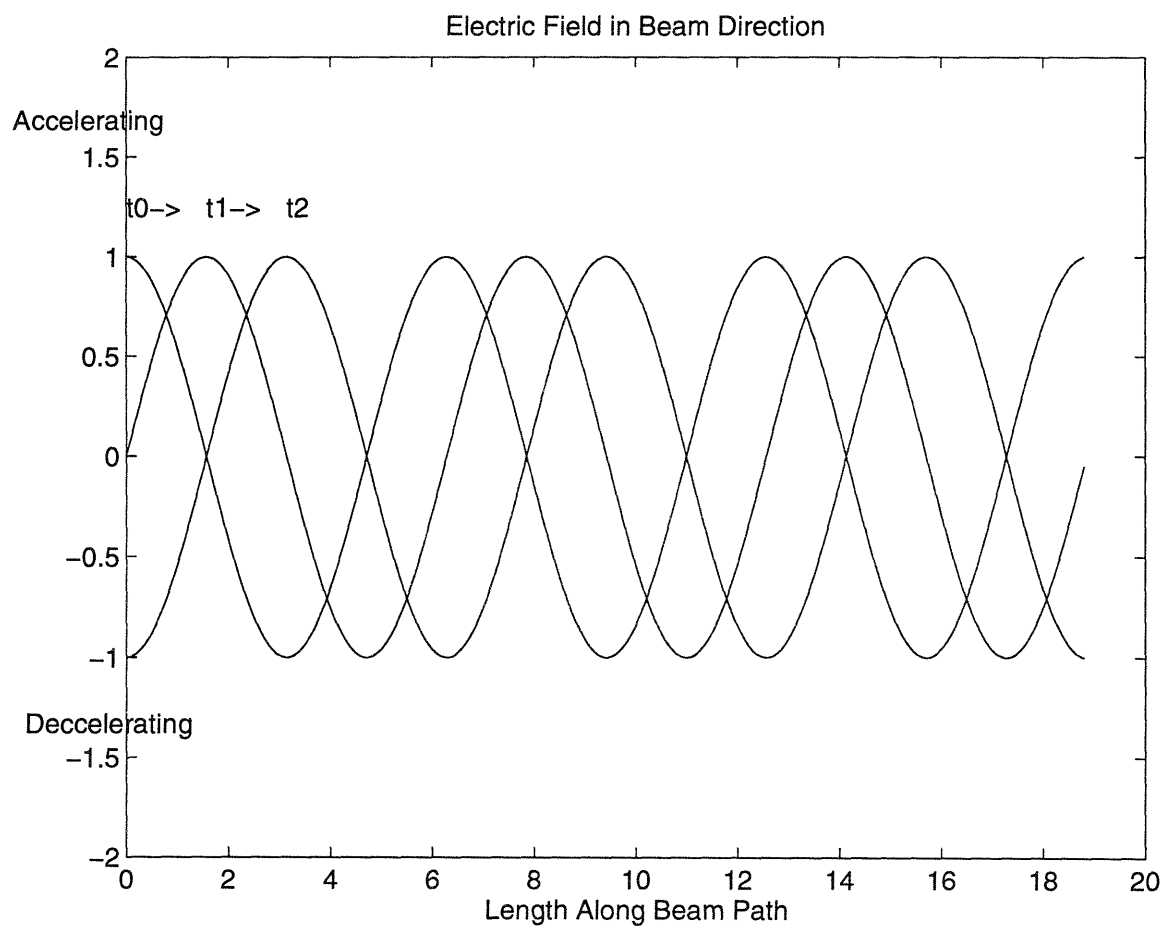
Figure 5-6: Electric Field Along Beam Direction

component of the quadrupole that provides acceleration of the beam.

The beam will become bunched at the locations where the longitudinal electric field changes from accelerating to deccelerating. Ions in the "accelerating" region will be accelerated to this point; ions in the "deccelerating" region will be slowed to this point. As this bunching point accelerates forward due to the time variation of the electric fields from time t0 to t1 to t2, the "bunch" of particles is accelerated forward with the point. This process of pushing the bunched particles forward on a crest of an accelerating electric field moving forward in time is a process used by linear accelerators classified as "Sloan-Lawrence Accelerators."

This process is know as "adiabatic bunching", and is one of the primary advantages to the RFQ concept because it is very efficient, accelerating eighty to ninety percent of the beam. Other types of linear accelerators typically lose thirty to fifty percent of the beam.

The advantages of RFQs are that the simultaneous focusing and accelerating allows the machines to be more compact than other types of linear accelerators and be very efficient, losing only a fraction of the beam that is normally lost in other types of linear accelerators. A disadvantage of RFQs is that the energy of the beam is a constant and cannot be changed for a given vane or rod structure. The energy of the beam is a function of the physical shape of the vanes.

5.3 DL-1 Neutron Source Characteristics

The neutron source used for this work was a radiofrequency quadrupole accelerator source.[3] The accelerated particle was deuterium and the reaction for neutron production was the deuterium-beryllium reaction. The DL-1 neutron source was chosen because it is compact, relatively easy to transport, and commercially available. The

Accelerated Particle	D+
Input Beam Energy (keV)	25
Output Beam Energy (keV)	975
Neutron Yeild (n/s/mA)	7.8E7
Maximum Beam Current during pulse (mA)	10
Beam Pulse Width (μs)	30-120
Pulse Repetition Rate (Hz)	1-640
Maximum Target Current (mA)	140
Maximum Target Yeild (n/s)	1E10
Accelerator Length (ft)	4
Accelerator Weight (lbs)	400
Pulsed RF Power (kW)	40
Maximum Duty Factor	2.25%

Table 5.2: DL-1 Source Characteristics

fact that it was already commercially available was important because we did not have to pay design costs for an item already in production and the item had already been through initial trials and debugging.

5.3.1 Accelerator Components

Accelerator Cavity and Ion Source

The ion source is a duoplasmatron ion source that produces deuterium ions (80-90% D+, 10-20% D_2+). The gas supply and the power supplies around it are isolated at 25 kV. The gas is then fed to the ion source, which is at electrical ground potential with the rest of the accelerator, via a flexible cable.

This beam of deuterium ions then passes through a small aperture into the accelerator cavity. The cavity is a cylindrical structure that contains four scalloped vanes. The RF power if fed into the cavity via a flexible cable connecting the accelerator cavity to the RF supply. The RF power then establishes the simultaneously bunching and accelerating quadrupole. This quadrupole accelerates the beam, which travels

71
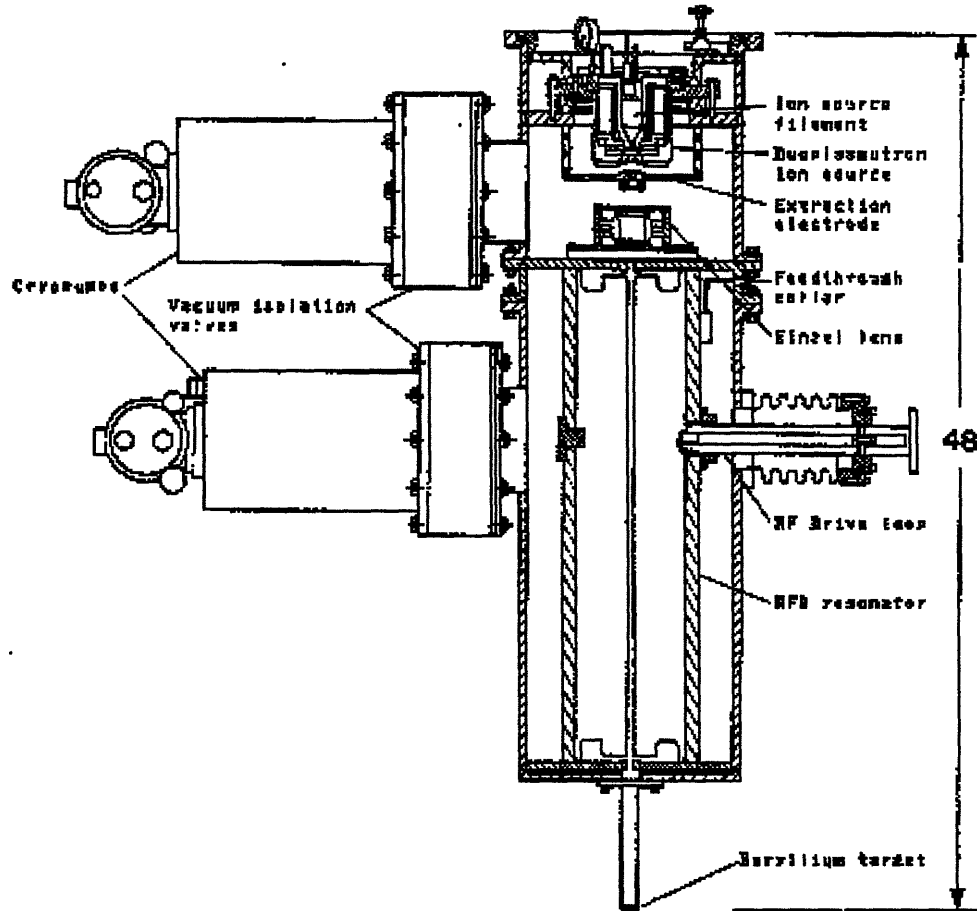
Figure 5-7: Ion Source and Accelerator Cavity

along the axis of the cylinder and strikes the beryllium target at the end of the beam tube. Figure 5.7 shows a schematic of the ion source and accelerator cavity.

Control System

The control and monitoring system consists of a 486 PC controlling two interface chassis. All interlocks are hardwired, not software dependent, for added security. The PC displays both monitored parameters, such as chamber pressure and measured arc current, and parameters that are set by the operator, such as gas flow voltage and set arc current.

72

This PC interface allows easy operator control of the ion source and beam pulse characteristics. The operator can control the ion source current and the beam pulse width, shape, and repetition rate.

5.3.2 Neutron Production

Choice of Target

Figure 5.2 shows the thick target neutron yields for various reactions.[18] Because RFQs are limited to low energies, one can see that the best choices for high neutron outputs are the tritium-deuterium reaction, and the lithium-deuterium and beryllium-deuterium reaction. The tritium-deuterium reaction is not a good choice because it would involve the containment of tritium and the neutrons produced are very high energies (about 14 MeV), much too high for thermal neutron radiography. A great deal of neutron moderation would be required.

The beryllium-deuterium reaction was chosen due to the superior heat transfer properties of beryllium, which has a higher melting point than lithium and could sustain higher currents without melting.

Neutron Energy and Angular Distribution

The energy and angular distribution of the neutrons produced by the deuterium-beryllium reaction were investigated by A.I. Shpetnyi in the mid 1950's. The following plots show the measurements he made of the neutrons produced in the reaction for 1 MeV deuterons on a beryllium target.

These plots show that the neutrons are relatively energetic (up to 5 MeV) and must be moderated to thermal energies. The plots do no show the thermal neutron
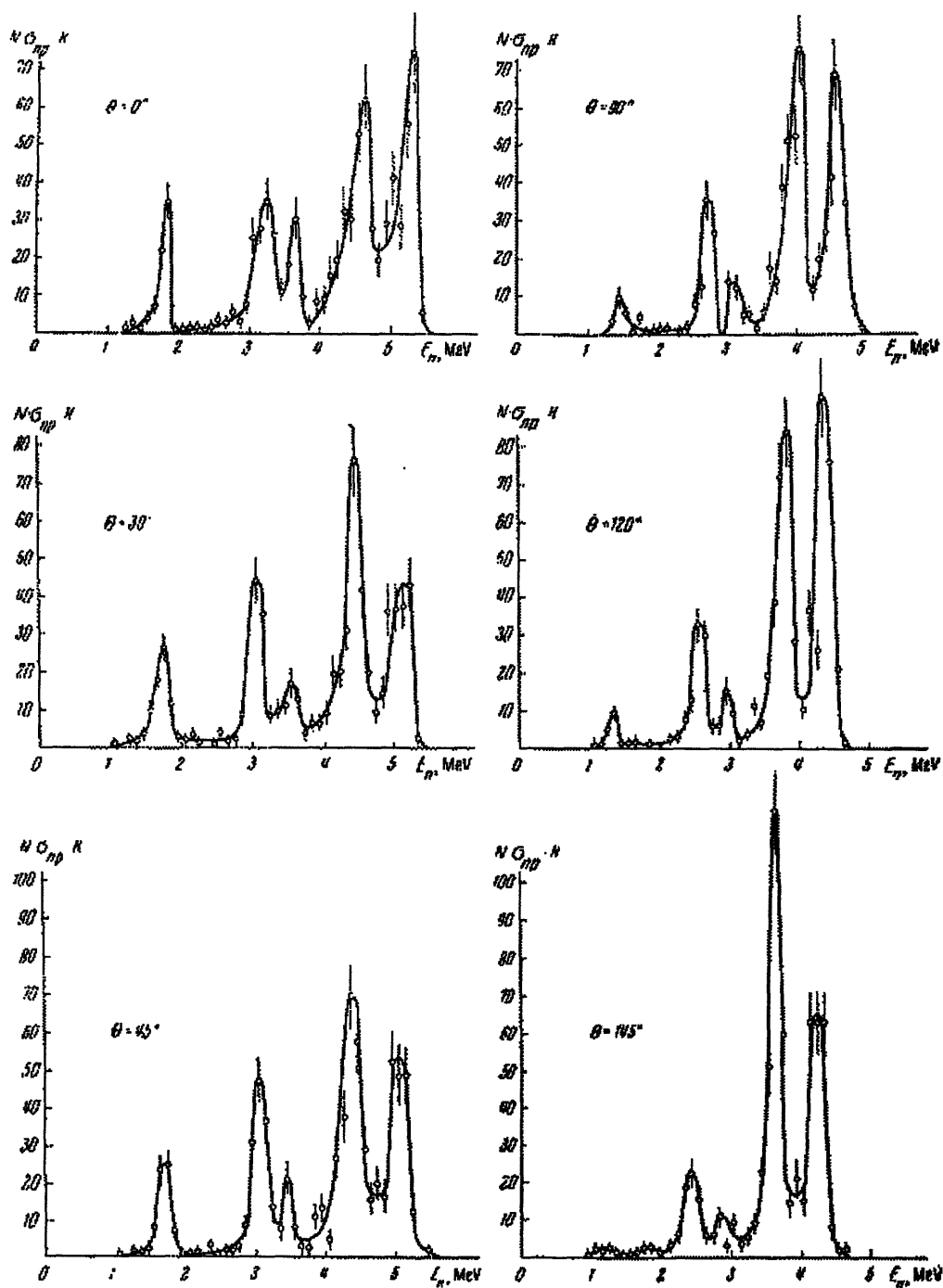
Figure 5-8: Neutron Production Spectrum from 1MeV Deuterons on Beryllium

production, because the detection methods used were not efficient for thermal neutron energies.

Target Position and Shielding

The target is mounted at the end of a stainless steel tube that extends approximately 30 inches from the end of the accelerator cavity. A beryllium disk 2 inches in diameter and 0.030 inches thick is brazed to the end of the steel tube. The stainless steel tube allows the accelerator to be kept in a separate room than the target, which improves the neutron shielding considerations for the surrounding areas.

The tube-target assembly extends through a 14 inch diameter hole cut in the 32 inch thick concrete wall that separates the room containing the accelerator from the room containing the target. Because the accelerator cavity extends a few inches into the hole connecting the accelerator room to the target room, the target sticks into the target room about 1 inch. The tube-target assembly is only 2 inches in diameter. The remaining space in the hole is filled with 16 one inch thick disks of high density polyethylene. A schematic of the target and part of the shielding assembly is shows as Figure 5.10.

The target is surrounded by a "cave" of polyethylene at least 30 cm thick, or the equivalent to 30 cm of polyethylene in concrete block, on all sides. The door to the target room was a solid concrete door 32 inches thick. A concrete "backstop" was erected behind the accelerator to shield any neutrons that might be produced in the target travelling back along the beam tube, which obviously cannot be shielded. Water tanks equivalent to 32 inches of concrete block were erected in front of a set of doors leading to the accelerator to allow for movable shielding. A small amount of lead was used to shield the low energy x-rays produced at the RFQ vanes.

This shielding resulted in neutron dose rates, including background, of less than

Concrete (81.28 cm)

High Density Polyethylene (40.64 cm)

Accelerator

Cavity

Stainless Steel Tube

with Beryllium Target
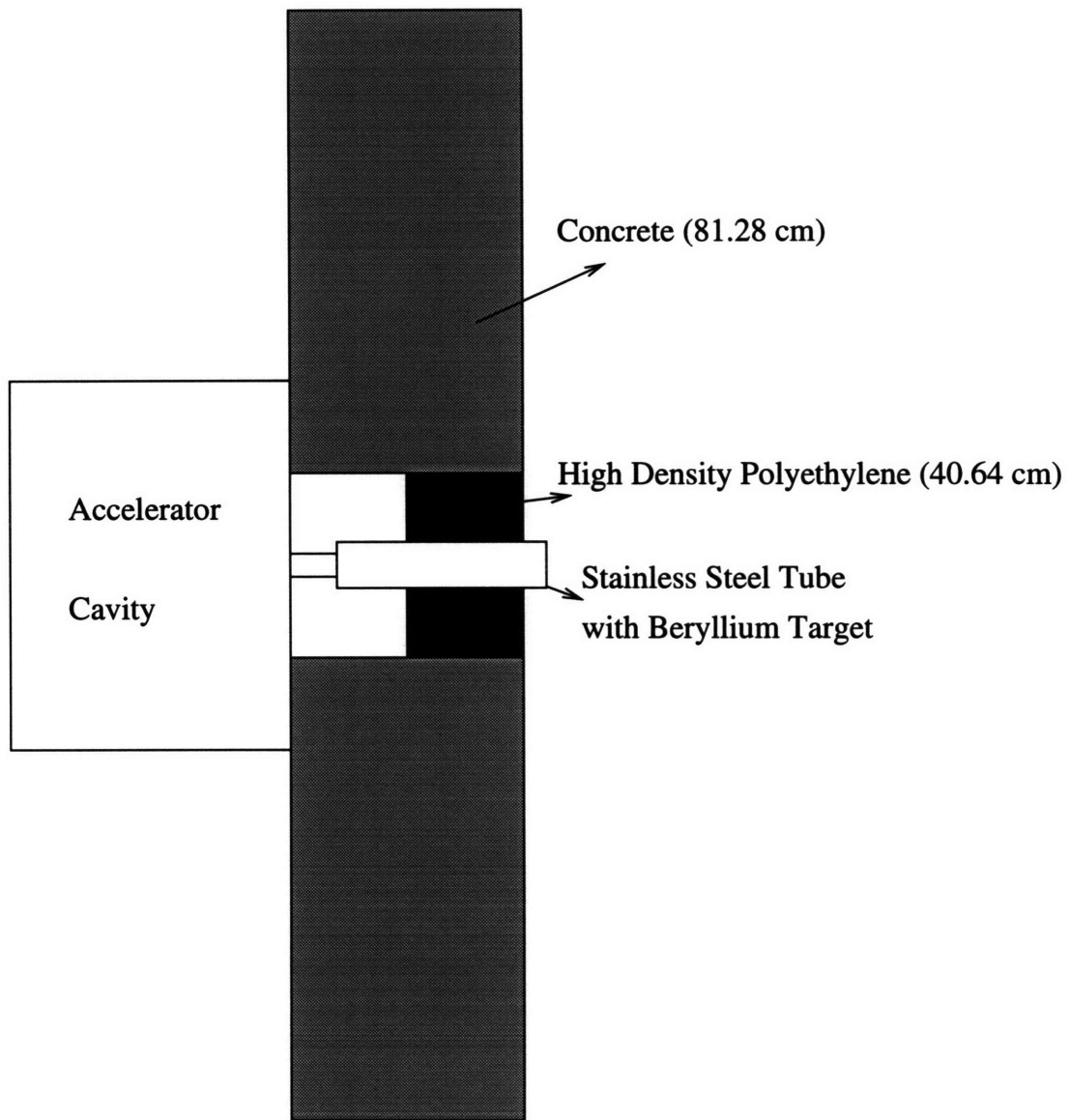
Figure 5-9: Target Position and Shielding

0.09 mrem/hr in all rooms adjacent to the accelerator and target room (including the rooms above) when operating at a time averaged beam current of 61 microamperes, approximately 60% of full power. The total dose rates, including background, were all less than 0.18 mrem/hr for the same current.

Moderator

We relied on the polyethylene behind the target and surrounding the target (the "cave") to provide most of the neutron moderation. One inch thick piece of high density polyethylene was placed in front of the target to act as a moderator. This design could definitely be improved.

Accelerator Operation and Safety

All rooms directly adjacent to the accelerator and target vault are protected by an interlock system. This system requires that every room in the interlock system must be searched prior to turning the accelerator on. Additionally, the accelerator will automatically shut off if any of the doors to these interlock protected rooms is opened and every room contains an emergency kill switch that shuts the accelerator down. This prevents any personnel from receiving any accidental exposure.

Turning the accelerator on requires that the interlock procedure be completed, the RF power supply is warmed up and on, and the arc is struck. The procedures to accomplish the arc striking and RF power supply warm up are described in the Accsys DL-1 manual.[3]

5.4 Flux Measurements

The neutron flux was measured in two ways. One method was to use the CCD camera assembly to determine the neutron flux. The other was to use a small lithium glass scintillator (a GS-20) connected to a phototube with a multi-channel analyzer.

5.4.1 Camera Method

In Chapter 4 we derived a conversion factor relating the ADC value of a CCD pixel and the neutron fluence in neutrons per square centimeter. We determined that one ADC count per pixel is the equivalent of 4.19E-4 neutrons per square centimeter. Thus, we can find the neutron fluence in neutrons per square centimeter by taking the pixel ADC value and multiplying by 4.19E-4. We can convert this into a flux value by dividing by the total time of exposure for the radiograph.

We must be careful of two details. One is that the CCD camera controller allows "pixel grouping." This means that we may take images where one *image* pixel consists of a group of *CCD* pixels. This grouping must be in square groups of CCD pixels. We may make one image pixel a 2x2 grouping of CCD pixels, or a 3x3 grouping. Many of the images we collected were grouped 4x4, so each image pixel contained 16 CCD pixels. We need to make sure that when we calculate the neutron flux and fluence we differentiate between **image** pixels and **CCD** pixels.

Another point to be careful of is to make sure that the CCD has not become saturated. Each image pixel has a maximum ADC value of 2^{15}, or 32,768 counts. Above this value, the CCD is saturated. Once saturated, the CCD no longer responds to incident neutrons. Thus, if the image pixel value is 3.2768E4, we must assume that the camera has become saturated and we cannot use the pixel ADC value to measure the neutron fluence.

5.4.2 GS-20 Measurements

The GS-20 is a glass scintillator that uses the same method as the NE-426 to detect neutrons. The GS-20 glass is loaded with lithium. The lithium undergoes the same n-alpha reaction as the NE-426 scintillator screen used in the imaging system (see chapter 4). The photons emitted are collected in a phototube and the output is read by a personal computer analyzer made by Nucleus, inc.[20] The MCA counts the number of responses at each energy channel. The neutron peak shows up very clearly, and the MCA software allows us to count the total number of events in the peak.

The GS-20 has an efficiency of 99.6% for thermal neutrons and is 4.0E-2 cm thick with an area of 2.895 cm^2. The efficiency of the GS-20 drops rapidly as the neutron energy rises above thermal levels. Figure 5.10 shows the absolute efficiency of the GS-20 detector vs neutron energy and the distribution of a Maxwellian distribution of neutrons at 300 K.[5] We will assume that the GS-20 detects only thermal neutrons. Figure 5.10 shows that this is not absolutely true, but because we do not know the energy distribution of our neutrons after moderation, we cannot determine the total efficiency of the GS-20 for our neutron beam.

The thermal neutron flux can be calculated using the following formula:

$$\phi = \frac{N}{a\epsilon t} \tag{5.2}$$

Where:

- N = total number of counts in neutron peak

- a = area of GS-20 = 2.895 square centimeters

- ϵ = GS-20 thermal neutron efficiency = 99.6%

- t = spectrum collection time

The GS-20 was also used to estimate the total neutron yeild. Because the neutron yields are fairly isotropic [30], we can estimate the total source strength by measuring
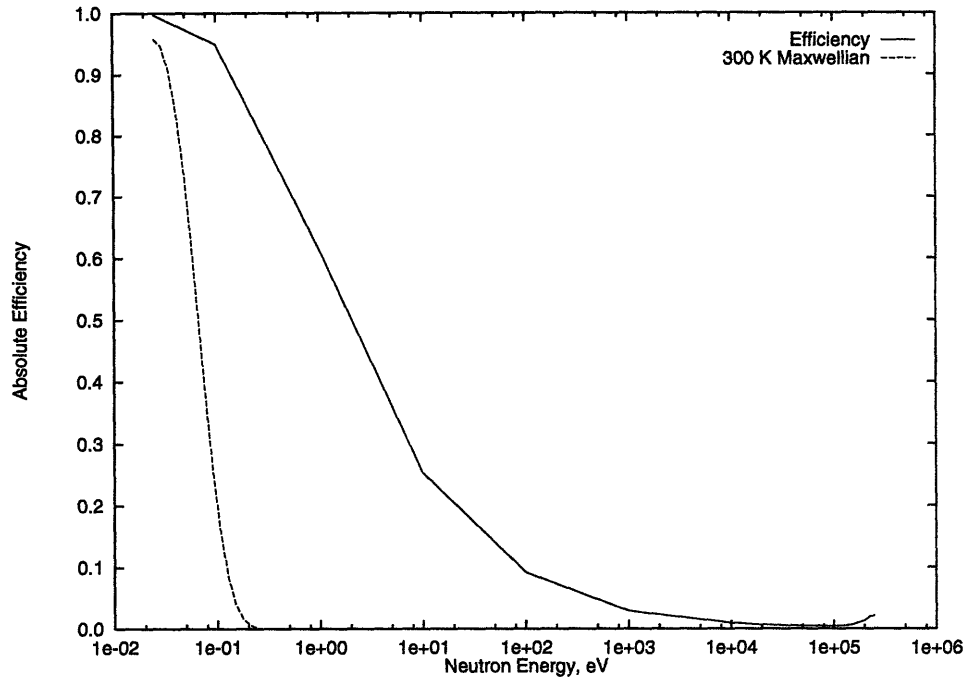
Figure 5-10: Absolute Efficiency of GS-20 vs Neutron Energy

the flux at a given distance from the source, then finding the area of a sphere of radius equal to the GS-20 - source separation. Multiplying the flux detected by the GS-20 by the total surface area of this sphere will yeild the total source strength. This is only an estimate due to a number of factors. First, the distribution of neutrons from the deuterium on beryllium reaction is not strictly isotropic. Secondly, the moderator and concrete wall surrounding the source affects the spatial distribution of neutrons from the source. Finally, the GS-20 is not uniformly efficient for all neutrons. As the neutron energy increases, the efficiency decreases. Thus we assume we only detect thermal neutrons.

5.4.3   Results

Table 5.3 contains the results of the source measurements made with the GS-20. All measurements were made with the GS-20 placed in line with the beam line.

The first value of 39.5 microamps was placed out of order because that mea-

Current	Time	GS-20	GS-20 - source	Flux @ GS-20	Source	$\frac{n}{s}/\mu A$
(μA)	(s)	counts	distance (cm)	$(\frac{n}{cm^2 s})$	Strength $(\frac{n}{s})$	
39.5	300	3.54E5	246.4	365	2.78E8	7.04E6
9.4	300	5.26E4	435.6	60.58	1.44E8	1.53E7
9.8	300	6.66E4	435.6	76.73	1.83E8	1.87E7
40.0	300	2.81E5	435.6	323.91	7.72E8	1.93E7
47.6	300	3.18E5	428.0	366.32	8.43E8	1.77E7
48.1	300	3.28E5	428.0	378.11	8.70E8	1.81E7
50.5	300	3.33E5	428.0	384.05	8.84E8	1.75E7
50.5	300	3.31E5	428.0	381.34	8.78E8	1.74E7

Table 5.3: DL-1 Source Strength Data

surement was taken before one of the amplifiers had to have a piece replaced and the machine was not receiving the full RF power output. This data point was not considered when we calculated the average thermal neutron production per second per microamp of beam current. Excluding that data point, we averaged $1.77x10^7 \frac{n}{\mu A}$, which is close to 7.8E7, the figure the manufacturer gave for total neutron production. The difference may be attributed to the assumption of isotropic neutron production, or the difference in GS-20 efficiency for different neutrons.

In order to determine the flux at the scintillator screen, we convert the mean pixel level of a blank screen exposure to a neutron fluence using the conversion factor we derived in section 4.5. Table 4.1 shows the average pixel ADC value for blank screen exposures for different amounts of time. By looking at the data collected for 40 μ A beam current with lead shielding the CCD, we can determine the neutron flux at the scintillator screen. We use the data collected with the lead in place because this reduces the noise due to x-rays and other background radiation, which would alter our camera response. We determined that with no background noise, one ADC per CCD pixel equals 4.19E-4 $\frac{n}{cm^2}$. Table 5.4 contains data showing the neutron flux at the scintillator screen for our system.

Our system produced typical neutron fluxes on the order of $10^4 \frac{n}{cm^2 s}$. Because the

Time (min)	Mean Pixel Value (ADC)	Fluence $\frac{n}{cm^2}$	Flux $\frac{n}{cm^2 s}$
.5	2.3E2	5.5E5	1.83E4
5	1.68E3	4.02E6	1.34E4
10	3.30E3	7.88E6	1.31E4
20	6.57E3	1.57E7	1.31E4
30	9.89E3	2.36E7	1.31E4

Table 5.4: Neutron Flux at Scintillator Screen

maximum fluence for this system is 7.82E6 $\frac{n}{cm^2}$, typical radiography exposures lasted on the order of 100 seconds to two minutes. This time can be lowered by increasing the pixel grouping and sacrificing spatial resolution.

The values of thermal neutron flux and total neutron production rate for this sytem were consistent with older, larger accelerator based sources. A mobile neutron radiography system with an accelerator based neutron source was developed in the early 1980's by W. E. Dance et. al. [7] This system used a sealed tube D-T source that provided up to $10^{11}\frac{n}{s}$ and a thermal flux of $10^4\frac{n}{cm^2 s}$ at the imaging area. [15] Our system provides less total neutron production, slightly less than $10^9\frac{n}{s}$ at about 50% total output, but the less energetic neutrons from the deuterium-beryllium reaction provide a larger ratio of thermal neutrons, so our system provides the same level of thermal neutron flux at the imaging area.

Chapter 6

Radiographs of Known Phantoms

We prepared a number of known samples to be radiographed to test the response of our system. The phantoms were all made of different materials of known hydrogen content radiographed with some sort of aluminum backing or casing. By taking radiographs of samples of known content we can measure the performance of our system.

6.1   Radiography Procedure

Each radiograph required that the neutron flux was measured, a blank screen exposure, a dark current exposure, and the radiograph itself. The neutron flux measurement was taken so that if we had to repeat any of the radiographs, we could attempt to reproduce the same source characteristics as the original radiograph. The dark current exposure was taken to remove fixed pattern noise (see chapter 5) from the radiograph. The blank screen exposure was taken to correct for spatial variations in the neutron flux over the image area.

The procedure used for each radiograph was fairly simple, and consisted of the following steps:

- Take GS-20 spectrum

- Place sample on imaging area on detector box and take radiograph

- Remove sample and take blank screen exposure

- Take another GS-20 spectrum to insure the source strength remained constant

- Take dark current exposure

6.1.1 Measuring the Neutron Flux

The neutron flux was measured using the GS-20 scintillator. Because the GS-20 is much further away from the target than the camera assembly, the flux measured at the GS-20 is NOT the same flux present at the scintillator screen. We could convert the GS-20 flux into a value corresponding to the expected flux at the scintillator screen using the $\frac{1}{r^2}$ rule, but the source does not follow the inverse square law inside of the moderator "cave" because it is surrounded by polyethylene and concrete, causing a great deal of noise and buildup due to neutron scatter. However, we do not need to know the neutron flux at the screen. We simply want to be able to reproduce the same source strength for a later radiograph if necessary. We can do this by keeping the GS-20 detector in the same location and simply matching the total number of counts in the GS-20 peak for a set amount of time.

6.1.2 Sample Exposure

After we measure the GS-20 response, the next step is to take an image of the sample to be radiographed. Most samples were relatively flat, so they were easy to fasten to the detector box. The outside of the aluminum box had a rectangle corresponding to the CCD imaging area scribed onto it. The sample was placed in this imaging area, then held in place, usually with tape. Then, the whole camera assembly was wheeled into the moderator cave, getting it as close to the source as possible. Due to obstructions from the concrete block and polyethylene cave, the camera assembly

could only get within a few inches of the beryllium target.

Once the camera is in place, a piece of tape or some other marker was used to locate the position of the back wheels on the camera support cart. This was done so that if the cart had to be wheeled back out of the cave to remove the sample, the camera could be repositioned in the same location for the blank screen exposure.

Once the camera and sample are in place, the neutron source is activated. Then, the software that controls the CCD is used to set the exposure time and the pixel grouping and the image is captured. At this point the image is inspected to see if any of pixels were close to the CCD saturation point. We have to keep in mind that the ADC values for the blank screen exposure will be higher than those for the sample exposure due to the increased neutron attenuation caused by the sample. If the sample exposure is very close to saturation, it is likely that the blank screen exposure will show saturation, and we should take another exposure for a slightly shorter period of time.

6.1.3   Blank Screen Exposure

The blank screen exposure was required to correct for the non-uniformity of the neutron flux. Because the center of the scintillator screen is closer to the neutron source than the edges of the screen, the blank screen exposures show a bright source spot in the center. This is easily seen in the figure below, which is a blank screen exposure of two minutes, pixels grouped 4x4.

This non-uniform neutron flux is why we have to take a blank screen exposure. How this blank screen exposure is used to make the radiograph more uniform is described in section 6.1.5. This figure also shows us why it is important to have the camera in the same location for the blank screen exposure and the sample exposure. If the camera is not in the same position, the bright spot on the screen will be offset
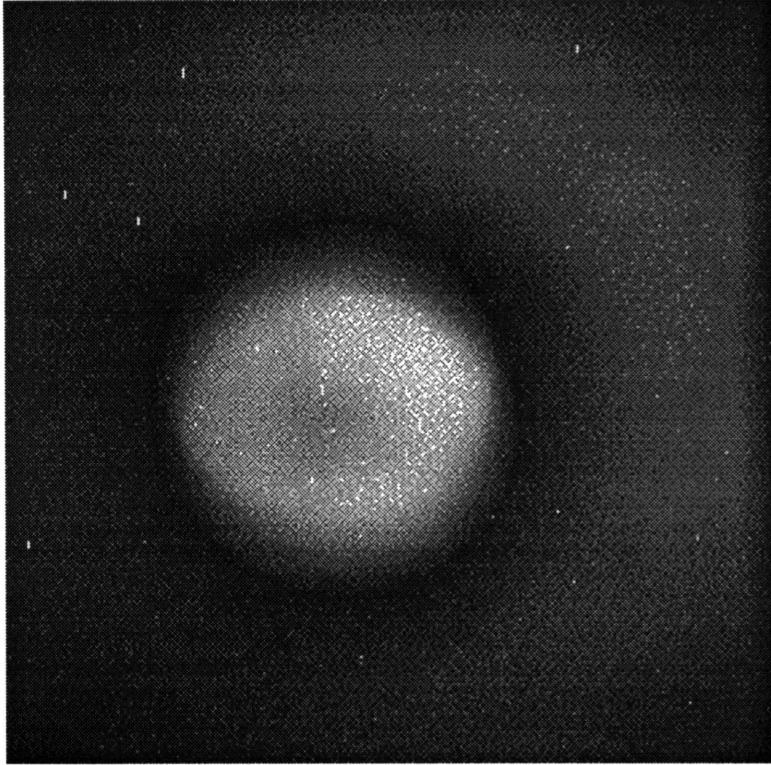
Figure 6-1: 2 Minute Blank Screen Exposure, Pixels Grouped 4x4

and this will cause errors in the algorithm that is used to correct for the non-uniform flux.

6.1.4 Dark Current Exposure

The dark current exposure is required to eliminate any fixed pattern noise from the images. The dark current exposure was taken with the neutron source off, so the camera location is not important. We just have to make sure that the pixel grouping and exposure time is the same as the blank field and the sample images.

6.1.5 Correcting for Non-uniform Flux

We used IPLab software[12] to display the images captured using the CCD. This software has a routine that corrects for the non-uniform source distribution. The

routine performs the following operation on each image pixel:

$$\overline{M} * \frac{Image - Dark}{Blank - Dark} \qquad (6.1)$$

Where:

- $\overline{M}$ = mean pixel ADC value for the blank screen exposure

- Image = pixel ADC value for the exposure with the sample to be radiographed

- Dark = pixel value of dark current exposure

- Blank = pixel value of blank screen exposure

Because this procedure goes pixel by pixel, each of these exposures must have the same number of pixels. If one is grouped 2x2 and another is grouped 3x3, the number of pixels will not be equal and the routine will not work. We must also insure that all exposures are for the same time, and that none of the exposures saturate the camera.

This routine eliminates the fixed pattern noise by subtracting the dark current from each image. Then, each pixel is replaced by the ratio of the pixel level of the image to the pixel level of the blank screen. This leaves a value between zero and one for each pixel. Finally, these ratios are each multiplied by the average brightness of the blank screen exposure. We are left with an image with a uniform background and the radiograph of the sample.

6.2 Types of Phantoms

Because the goal of this study was to investigate the use of neutron radiography to inspect aluminum aircraft components for corrosion, and this technique is based on detecting hydrogen in the corrosion products, all of the phantoms consisted of some type of hydrogen containing compound in an aluminum shell.
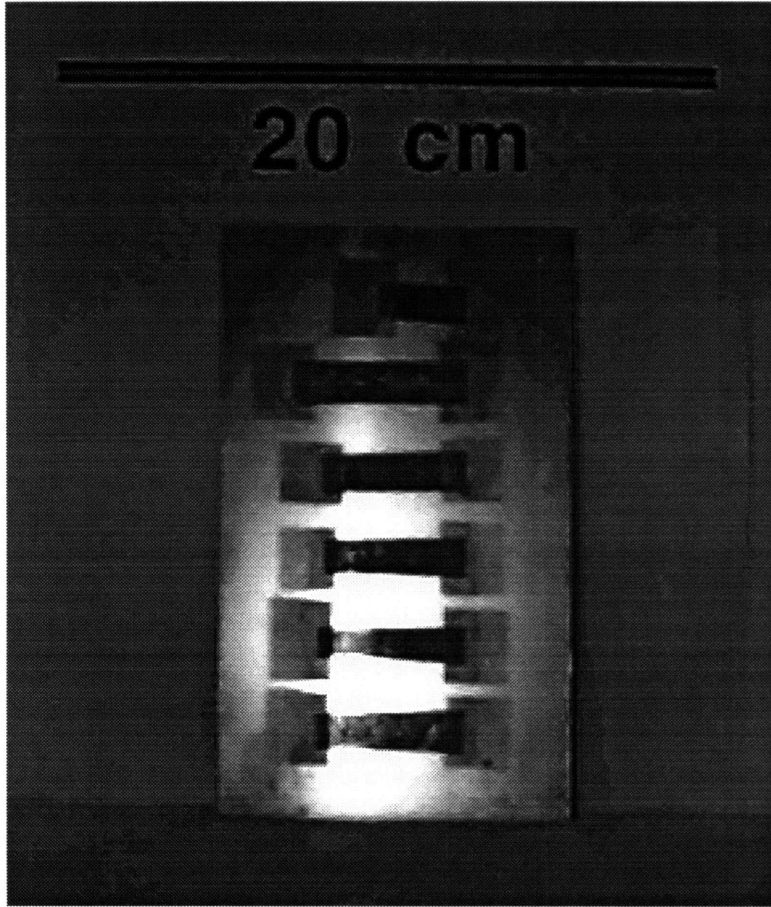
Figure 6-2: Photograph of Corrosion Sample Phantom

6.2.1 Corroded Aluminum Samples

One of the phantoms imaged consisted of six pieces of aluminum that were placed in a corroding solution for two to sixty-five hours. The aluminum pieces were strips about 1 cm wide and four to five centimeters long, except for the sample which had been corroded for sixty-five hours, which broke and was only about 2 centimeters long.

Figure 6.2 is a photograph of the corrosion sample phantom. The photograph shows six strips of aluminum that have been placed in a corrosive solution for varying lengths of time. The length of time each strip of aluminum was left in solution was, from top to bottom, 2 hours, 4 hours, 6 hours, 20 hours, 40 hours, 65 hours. The six corroded strips of aluminum were secured to a rectangular piece of uncorroded aluminum about 0.762 mm thick. The strips of corroded aluminum are 1 mm thick
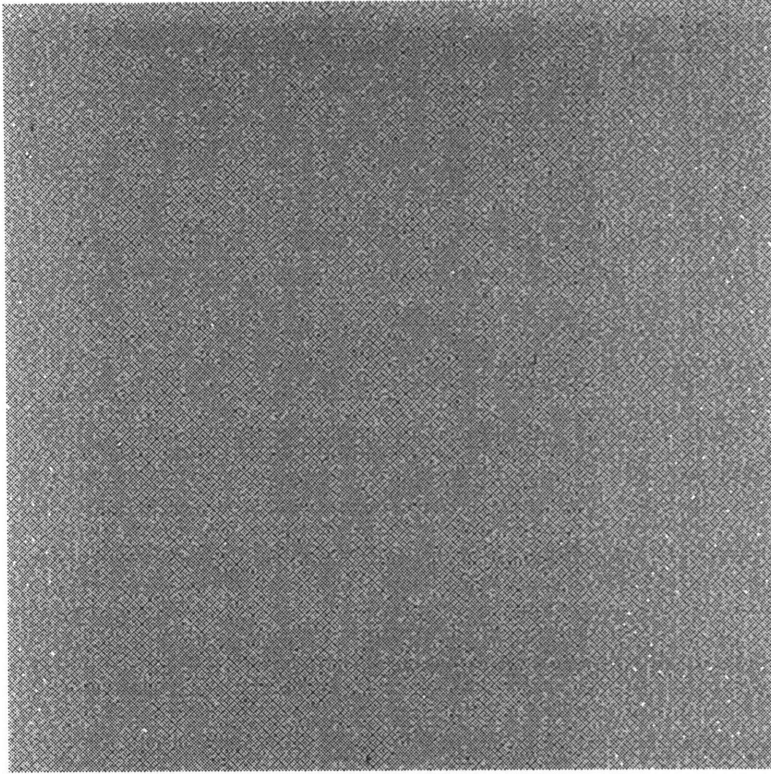
Figure 6-3: Radiograph of Corrosion Sample Phantom, 2 Minute Exposure, 4x4 Pixel Grouping

and were held to the uncorroded aluminum backing with one piece of Scotch Tape on the left and right sides of each corroded strip.

Figure 6.3 is a radiograph of the corrosion sample phantom. The phantom was taped to the aluminum detector housing so that the strips of corroded aluminum were horizontal and the broken corrosion strip was at the bottom of the image. The exposure time was two minutes, and the total number of counts detected by the GS-20 placed 428 cm from the source over a collection time of five minutes was 1.85E5 counts. The CCD pixels were grouped 4x4. To find the size of the area of the phantom represented by each image pixel, we use the length of a CCD pixel on one side multiplied by the number of CCD pixels grouped for each image pixel, then multiply by the minification caused by the lens (7 for our system). Thus, each image pixel represents a square of the phantom that is 22.5E-3 mm x 4 x 7 = 0.63 mm on a side.
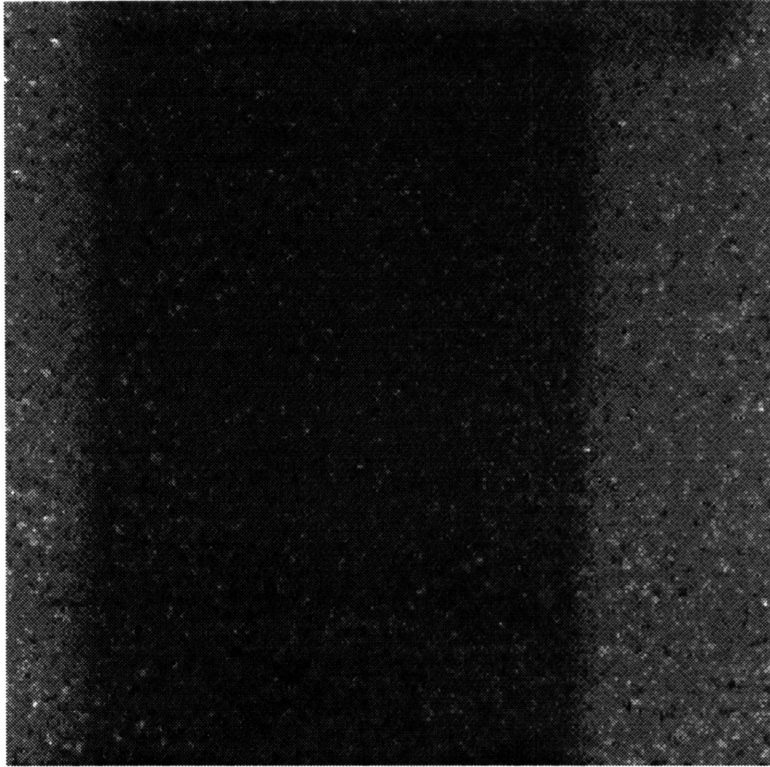
Figure 6-4: Median Filtered Image of Corrosion Sample Phantom

The corrosion strips do not show in Figure 6.3. In order to attempt to reduce the noise in the image, a median filter was used. The median filter was included in the IPLab software package. The filter replaces each pixel ADC value by the average of the ADC values of the nine pixels in the 3x3 square centered on the pixel being replaced. This has the effect of smoothing the picture. The median filtered radiograph is shown in Figure 6.4.

In order to evaluate the data to see if there was a detectable difference in neutron attenuation in the strips of corroded aluminum, the average pixel level of each row of pixels was plotted (see Figure 6.5). The graph should show a constant ADC value for the areas of aluminum that were not covered by corroded aluminum strips with lower average pixel ADC values for the rows of pixels that correspond to horizontal areas covered by corroded aluminum strips. The amount that the average pixel level drops should increase as the length of time of exposure to corrosive solution increases
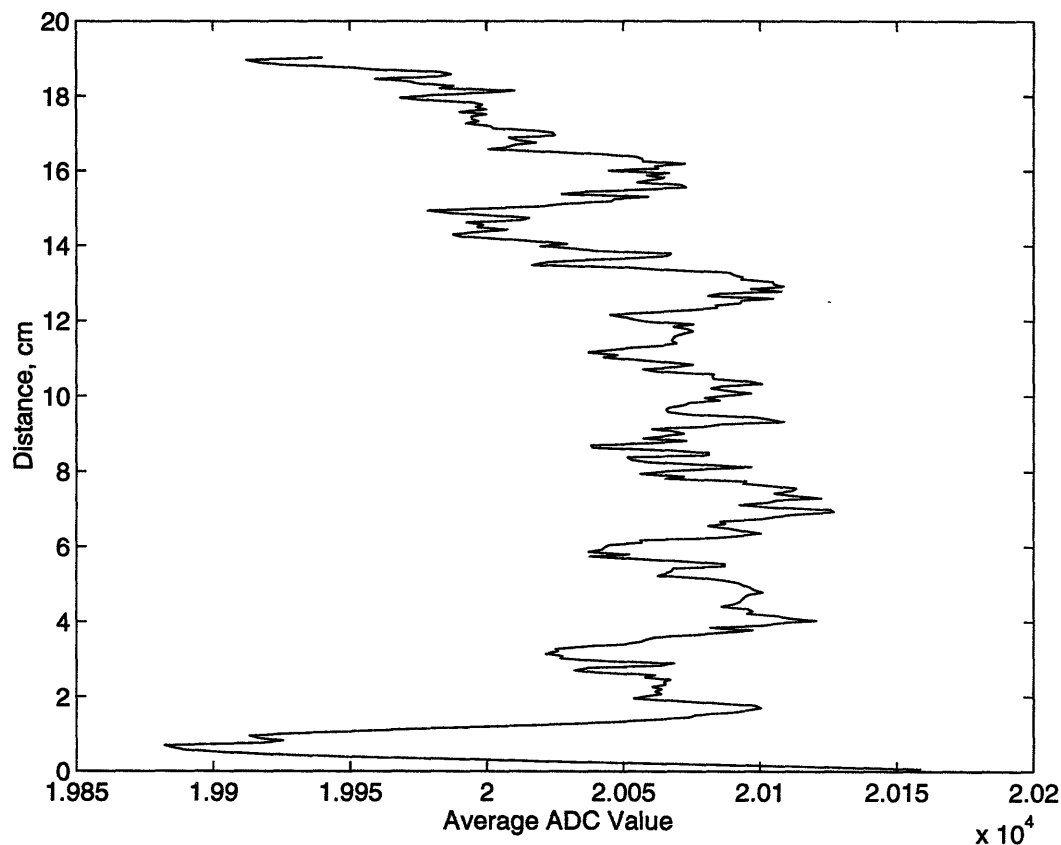
Figure 6-5: Graph of Average ADC Value of Filtered Image vs Vertical Position

for each strip, due to more hydrogen containing corrosion product being present in the aluminum strips that were exposed for longer periods of time, causing increased attenuation of the neutron beam.

The graph does not show this expected behavior. The average ADC value of each row of pixels fluctuates wildly. We derived in this section that each pixel is 6.3E-2 cm on each edge. Using this conversion factor, we plotted the average ADC value across each row against the height of the row of pixels. The Top of the uncorroded aluminum sheet, where the tape fastened the phantom to the detector assembly, corresponds to 19 cm.

Figure 6.5 shows the graph of average ADC value vs pixel row for the median filtered radiograph. We know that each image pixel is 6.3E-2 cm on each edge. Using

this conversion factor, we plotted the average ADC value across each row against the height of the row of pixels. The top of the uncorroded aluminum sheet, where the tape fastened the phantom to the detector assembly, corresponds to 19 cm.

The plot does not show the expected behavior. It does show a series of six dips in the average ADC value approximately 2.5 cm apart, which was the spacing between the strips of corroded aluminum. However, these dips are very noisy and do not show the expected correlation between length of exposure to corrosion solution and neutron attenuation. This could be due to an error in the creation of the strips of corroded aluminum or an error in the radiographic process. Because we do not know the actual hydrogen content of each strip, we cannot determine what the source of the error was.

6.2.2   Polyethylene Phantom

The next phantom we used was a phantom that was created using aluminum and polyethylene. A sheet of aluminum 9.4E-2 cm was used for backing, and four rectangular pieces of polyethylene were taped to the front side of this aluminum. A photograph of the phantom is shown as Figure 6.6. The thicknesses of the polyethylene pieces are: 0.23 cm (Upper Left), 7.6E-2 cm (Upper Right), 5.3E-2 (Lower Left), and 1.4E-2 cm (Lower Right).

Two radiographs of the polyethylene phantom are shown. Figure 6.7 shows an unfiltered, 2 minute exposure, CCD pixels grouped 4x4, 1.87E5 GS-20 counts over 300 seconds. Figure 6.8 shows the same radiograph after median filtering.

High density polyethylene has a neutron attenuation coefficient of $3.3 cm^{-1}$. We can use this to predict the expected attenuation of the polyethylene rectangles. By measuring the mean ADC value of the regions corresponding to the polyethylene rectangles and the unattenuated region of the radiograph, we can determine the actual neutron attenuation in the phantom. Table 6.1 lists the average ADC value for dif-
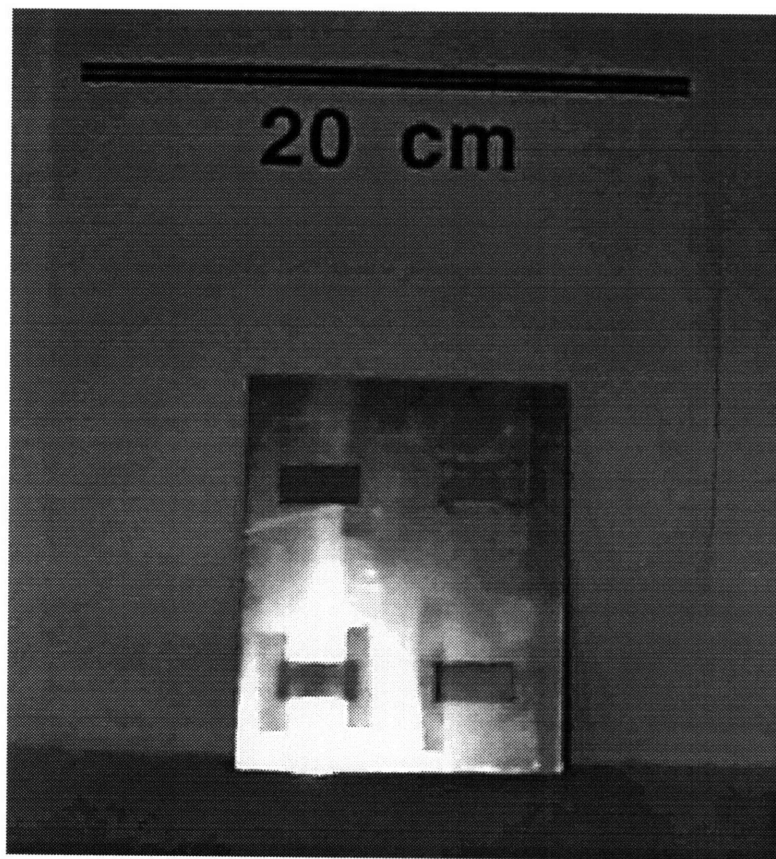
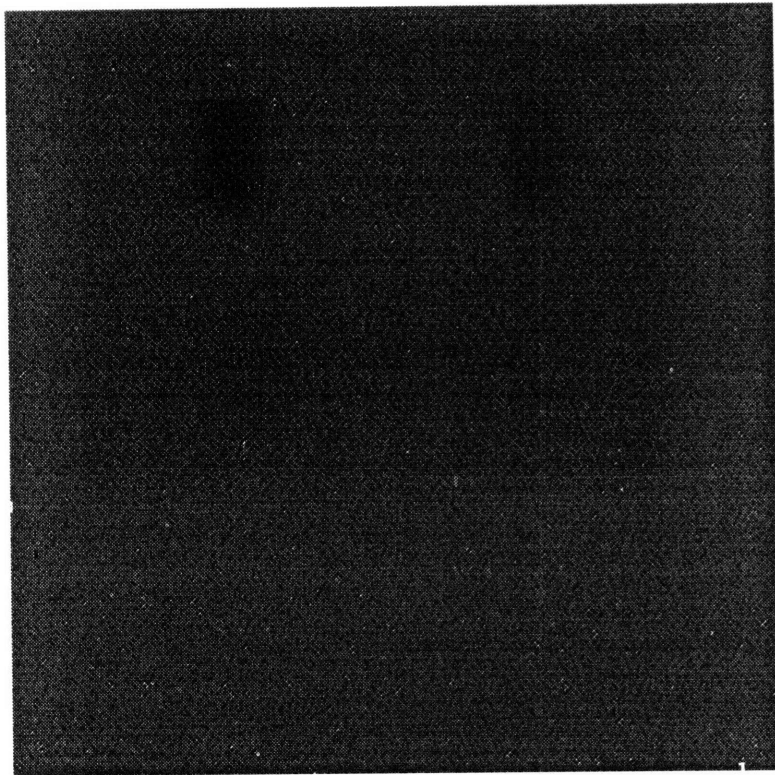Figure 6-6: Photograph of Polyethylene Phantom

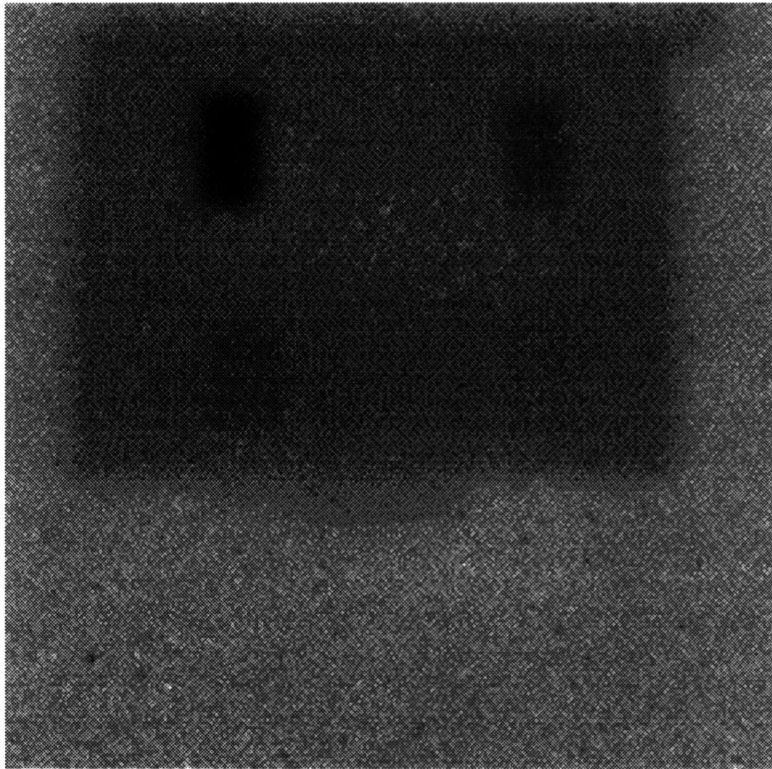Figure 6-7: Unfiltered Radiograph of Polyethylene Phantom, 2 Minute Exposure, 4x4 Pixel Grouping

Figure 6-8: Median Filtered Radiograph of Polyethylene Phantom, 2 Minute Exposure, 4x4 Pixel Grouping

Region	Contains	Unfiltered		Filtered	
		Mean	Std. Dev.	Mean	Std. Dev.
		ADC/pixel	ADC/pixel	ADC/pixel	ADC/pixel
1	.23 cm Poly	1.67E4	6.3E2	1.65E4	4.0E2
2	7.6E-2 cm Poly	1.82E4	3.9E2	1.82E4	2.2E2
3	5.3E-2 cm Poly	1.90E4	4.0E2	1.89E4	9.3E1
4	1.4E-2 cm Poly	1.95E4	4.8E2	1.94E4	1.2E2
5	7.63E-2 cm Al	1.99E4	4.5E2	1.99E4	1.1E2
6	No Phantom	2.09E4	5.3E2	2.09E4	1.4E2

Table 6.1: Mean Pixel ADC Value of Regions of the Polyethylene Phantom

Region	Predicted Attenuation	Measured Attenuation	
		Unfiltered	Filtered
1	46.5%	79.7%	79.1%
2	77.7%	87.0%	87.2%
3	83.8%	91.0%	90.7%
4	95.4%	93.1%	93.1%
5	99.9%	95.0%	95.1%

Table 6.2: Neutron Attenuation of Regions of Polyethylene Phantom

ferent regions of the phantom.

The predicted and experimental numbers are in relatively good agreement. The difference is probably due mostly to the fact that the system does have a small but measurable response to photons. Since x-rays are produced in the source, the signal observed in the CCD is not due only to thermal neutrons, and the attenuation of the signal is due to the combined attenuation of x-rays, fast neutrons, and thermal neutrons. The predicted attenuation data is based on thermal neutron attenuation alone. The thermal neutron attenuation coefficient of high density polyethylene, 3.3 inverse cm, is relatively close to the thermal neutron attenuation coefficient of the corrosion products of aluminum (see chapter 3). Thus, the radiograph of this polyethylene phantom is a good approximation of how the system will respond to similar thicknesses of corrosion in aluminum.
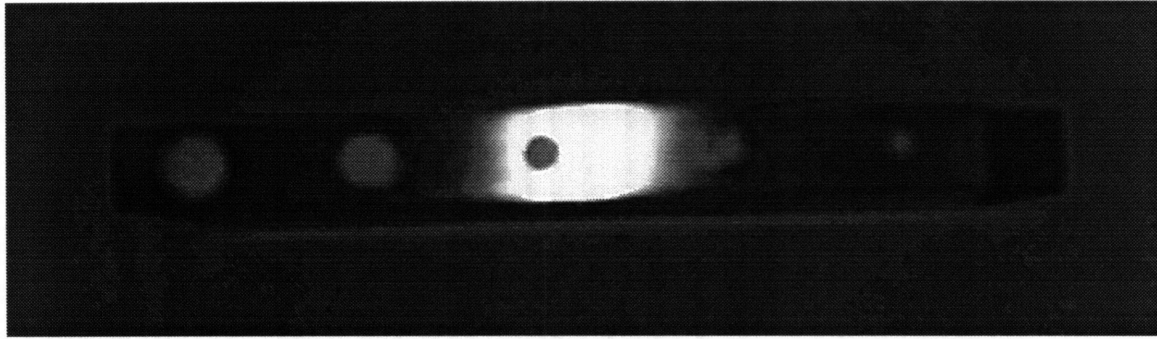
Figure 6-9: Photograph of Aluminum Hydroxide Phantom

6.3   Aluminum Hydroxide Phantom

Another phantom that was used was a rectangular prism of aluminum that had five cylindrical voids drilled into it. These voids were then filled with aluminum hydroxide powder, and the phantom was radiographed. Figure 6.9 shows a photograph of the phantom.

The prism dimensions are 12.5cm x 5 cm x 0.7 cm. The hole diameters are 0.95 cm, .79 cm, .64 cm, .48 cm, and .32 cm. The hole depths are all approximately 2.5 cm. The powder used to fill the holes was 50% Al_2O_3 and 50% $Al(OH)_3 : xH_2O$. This form of aluminum hydroxide is good because it approximates actual corrosion products in aluminum, but the disadvantage is that the hydrogen content is unspecified, making it impossible to know the actual thermal neutron attenuation coefficient of the powder.

Figure 6.10 shows a median filtered image of the radiograph of the aluminum hydroxide phantom. The exposure time was 2 minutes, the CCD pixel grouping was 4x4, and there were 1.33E5 GS-20 counts over 300 seconds. The phantom was held in place using black electrical tape around the edges.
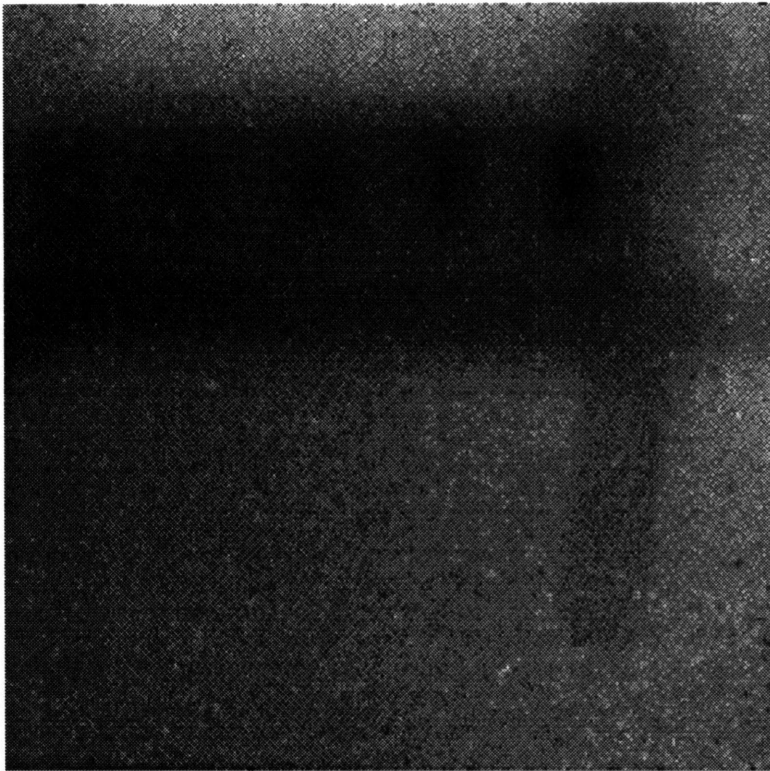
Figure 6-10: Aluminum Hydroxide Phantom, Median Filtered Radiograph, 2 Minute Exposure 4x4 Pixel Grouping
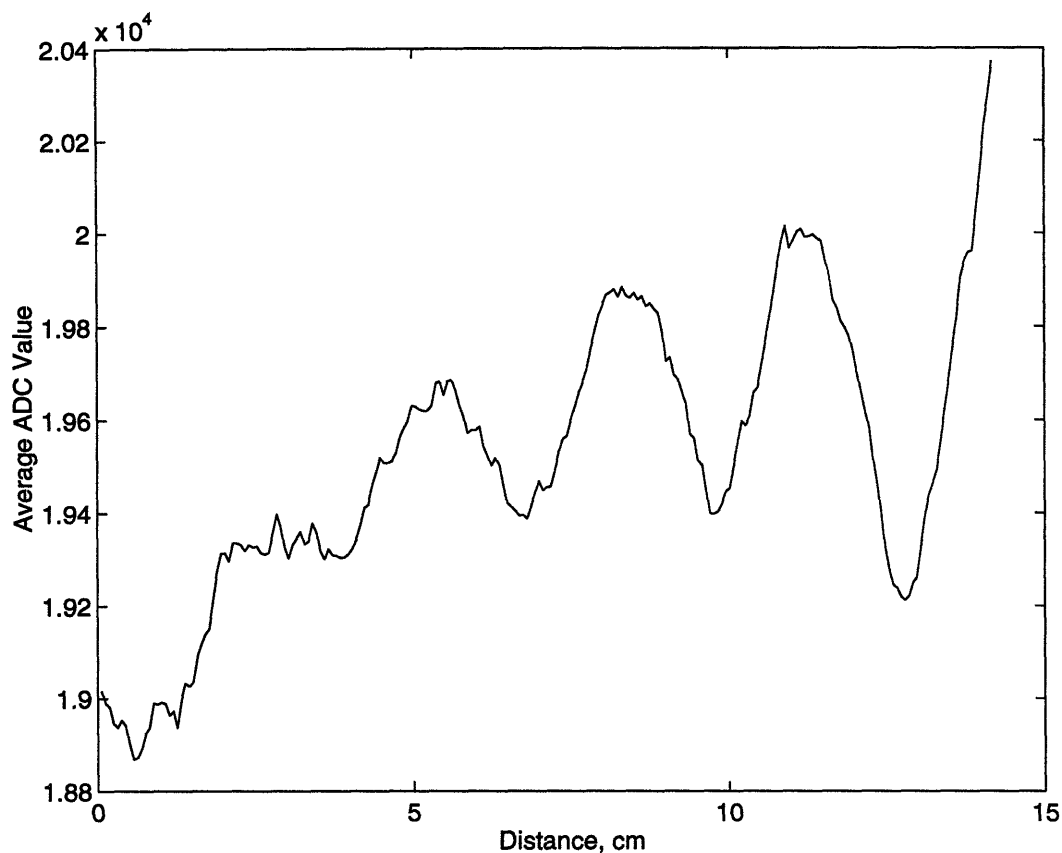
Figure 6-11: Average ADC Value of Each Column of Figure 6.10 vs Horizontal Position

The cylinders of powder are easily identifiable, and so is the tape holding the phantom in place. A plot of the average pixel ADC value for each column in the phantom was generated, and is shown as Figure 6.11. This plot should show a constant ADC value for each row where no powder is located, with dips in the average ADC level corresponding to each cylinder, with the amount the average ADC level decreases corresponding to the diameter of the cylinder. It shows the appropriate decreases at each cylinder, but the background level is not as constant as we expect. This could be due to poor positioning of the camera assembly for the blank screen exposure or residual powder on the surface of the aluminum prism causing attenuation of the beam in areas where no cylinder exists.

Once again, we calibrated the "pixels" to distances. 0 cm corresponds to the far

left edge of the phantom. We see four areas where the average column ADC value has dropped significantly, as well as places where the tape causes a decrease in the ADC value. We cannot see the fifth cylinder of powder because it is hidden by the tape.

6.4 Wax Phantom

The final phantom used consisted of a square sheet of aluminum, 15 cm x 15 cm x 0.15 cm. The center of this square of aluminum was milled out, leaving a 2.5 cm border on all sides. This center region was milled out into a series of five steps, each one 9.9 cm long and 1.9 cm wide. The first step was milled to a depth of 1.3E-2 cm, the next 2.5E-2 cm, the next 3.8E-2 cm, the next 5.1E-2 cm, the last step was 6.3E-2 cm. This region of "steps" was then filled with wax by melting the wax and pouring it over the aluminum. After the wax cooled, the excess wax was scraped off until the surface was a flat plane. This technique produced a relatively even surface, however, a few voids and ripples were left and the density of the wax may not be uniform.

This square of aluminum filled with wax steps was then covered by a second square sheet of aluminum, 15cm x 15 cm x 0.15 cm. The two squares of aluminum were sealed around the edges with black electrical tape, creating a step wedge of wax sandwiched between two sheets of aluminum. Figure 6.12 is a photograph of the two sheets of aluminum.

Figure 6.13 shows a median filtered image of the radiograph of the wax phantom. The exposure time was 100s, the CCD pixels were grouped 4x4, and there were 2.08E5 GS-20 counts over 300 seconds. The wax and tape are easily seen.

Figure 6.14 shows the average ADC value of each column of pixels of the radiograph of Figure 6.13. 0 cm corresponds to the outside edge of the 1.27E-2 cm deep
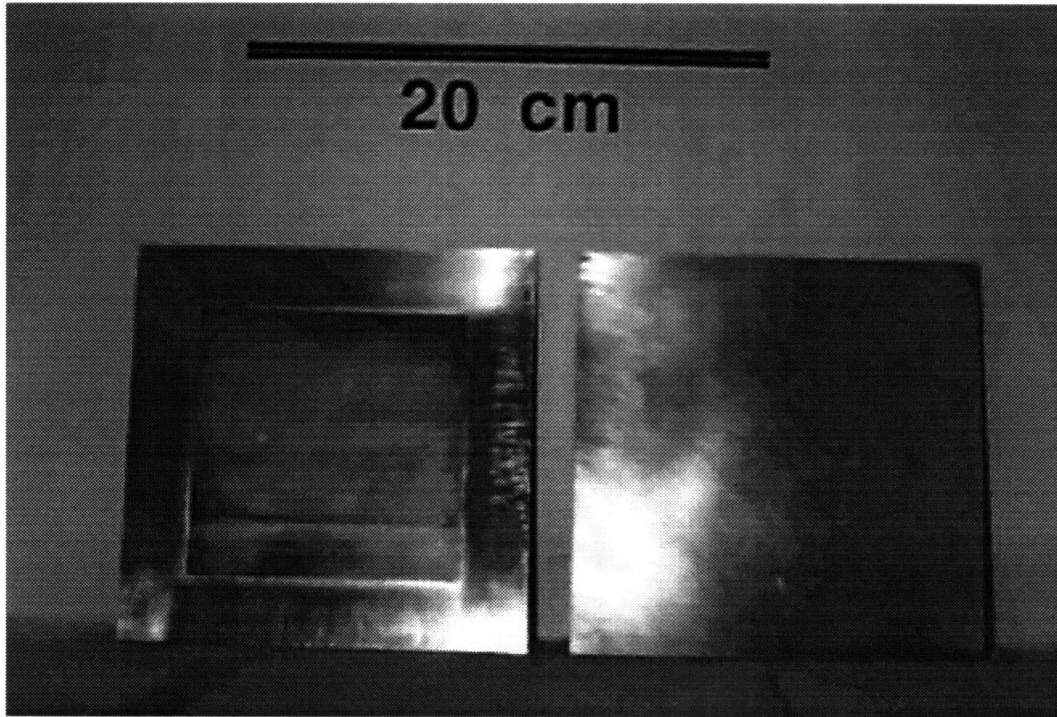
Figure 6-12: Photograph of Wax Phantom
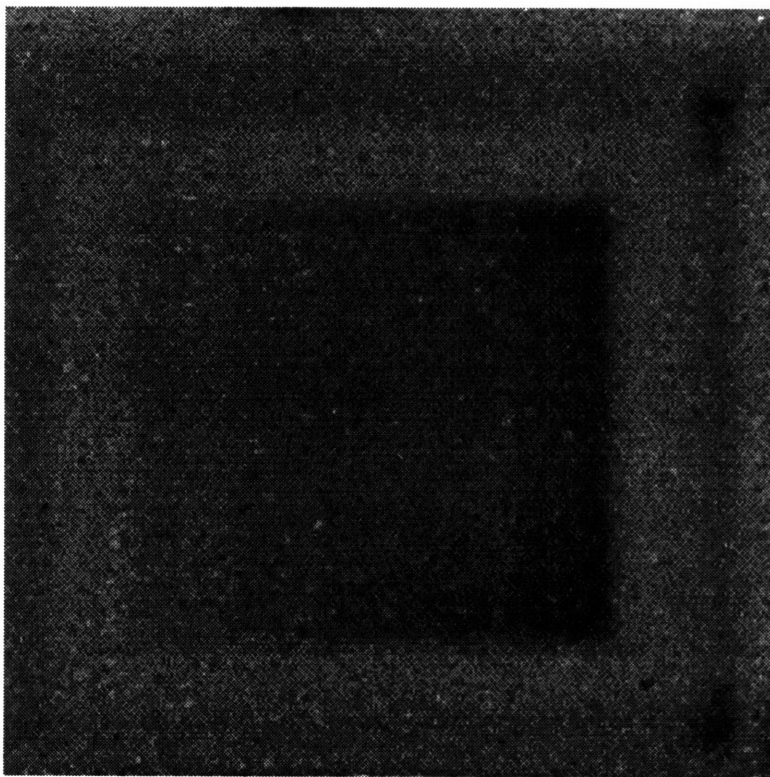
Figure 6-13: Median Filtered Image of Radiograph of Wax Phantom, 100s exposure, 4x4 Pixel Grouping
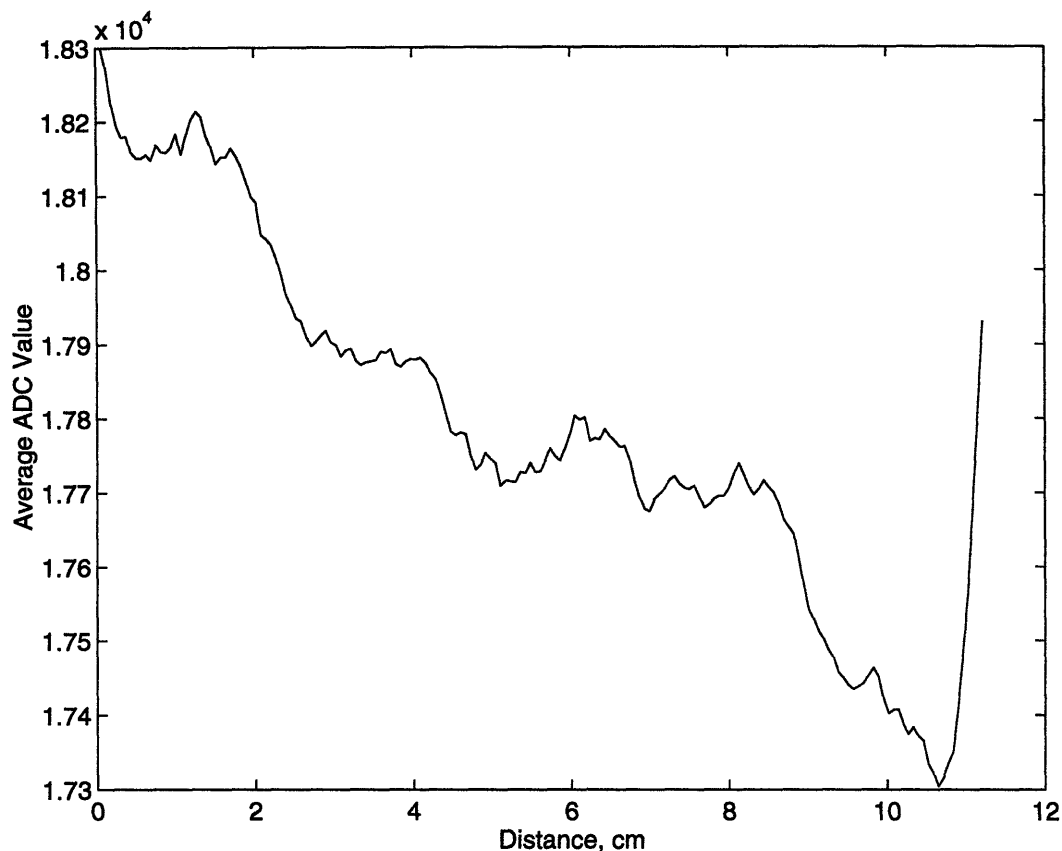
Figure 6-14: Average ADC Value of Each Column in Figure 6.13 vs Position

step.

We see four recognizable steps, but expect to see five. On closer inspection the center step appears to be as wide as two "normal" steps. Looking at the area of the wax phantom corresponding to these areas, we can see that there are a number of bubbles and voids, more than in the other regions. This uneven distribution of wax might explain why these steps are not well defined, and appear to form a single large step.

The average pixel level was found for each of the "steps" in the median filtered image. The data is compiled in Table 6.3.

Wax has a thermal neutron attenuation coefficient of $3.3\frac{1}{cm}$, which is close to the

Region	Contents	Mean Pixel ADC Value	Std. Dev.
1	6.4E-2 cm wax	1.7435E4	1.7E2
2	5.2E-2 cm wax	1.7711E4	1.5E2
3	3.8E-2 cm wax	1.7756E4	1.2E2
4	2.5E-2 cm wax	1.7875E4	1.1E2
5	1.3E-2 cm wax	1.8138E4	1.3E2
6	0.30 cm cm Al	1.8572E4	1.0E2
7	Void	1.8687E4	1.8E2

Table 6.3: Mean Pixel Level of Regions of the Wax Phantom

Region	Contains	Measured Attenuation	Predicted Attenuation
1	6.4E-2 cm wax	93.3%	81.0%
2	5.2E-2 cm Wax	94.8%	84.2%
3	3.8E-2 cm wax	95.0%	88.2%
4	2.5E-2 cm Wax	95.7%	92.1%
5	1.3E-2 cm Wax	97.1%	95.8%
6	0.30 cm Al	99.4%	99.9%

Table 6.4: Predicted and Measured Neutron Attenuation of Regions of Wax Phantom

value of the attenuation coefficient of the aluminum corrosion products (see Chapter 3). Using this thermal neutron attenuation coefficient, we can determine the expected thermal neutron attenuation in the phantom. The predicted and measured values are contained in Table 6.4.

Again, we see that the actual data shows less attenuation than predicted. This is probably because of x-rays contributing to some part of the signal detected in the imaging system. Because the data for the predicted attenuation was generated using thermal neutron cross sections, and some of the signal is generated by fast neutrons and x-rays, the predicted attenuation values are too low. This is the same problem we encountered with the polyethylene phantom.

Chapter 7

Radiographs of Aircraft Components

After we verified that the system was working as expected by taking radiographs of phantoms whose internal structure was known, we used the system to take radiographs of objects whose internal structure was not known. The objects we chose to use were lap joints taken from older aircraft that had been dismantled. Lap joints are places in the aircraft skin where two sheets of aluminum are joined. This is usually accomplished by overlapping the two sheets, bonding them together with some sort of epoxy, and then riveting the sheets together. Often, a "spacer" is also riveted to the joint at this overlap. Figure 7.1 shows a schematic of a typical lap joint. [2]

Three lap joints were imaged. The lap joints came from a section of an old KC-135 mid-air refueling tanker that had been repaired. The epoxy and new rivets used in the repair of these lap joints made the repaired area easy to see. The epoxy was applied in a thick layer, and excess epoxy lined where the spacer joined the lapjoint. The rivets which were replaced as part of the repair were replaced by larger, longer rivets.
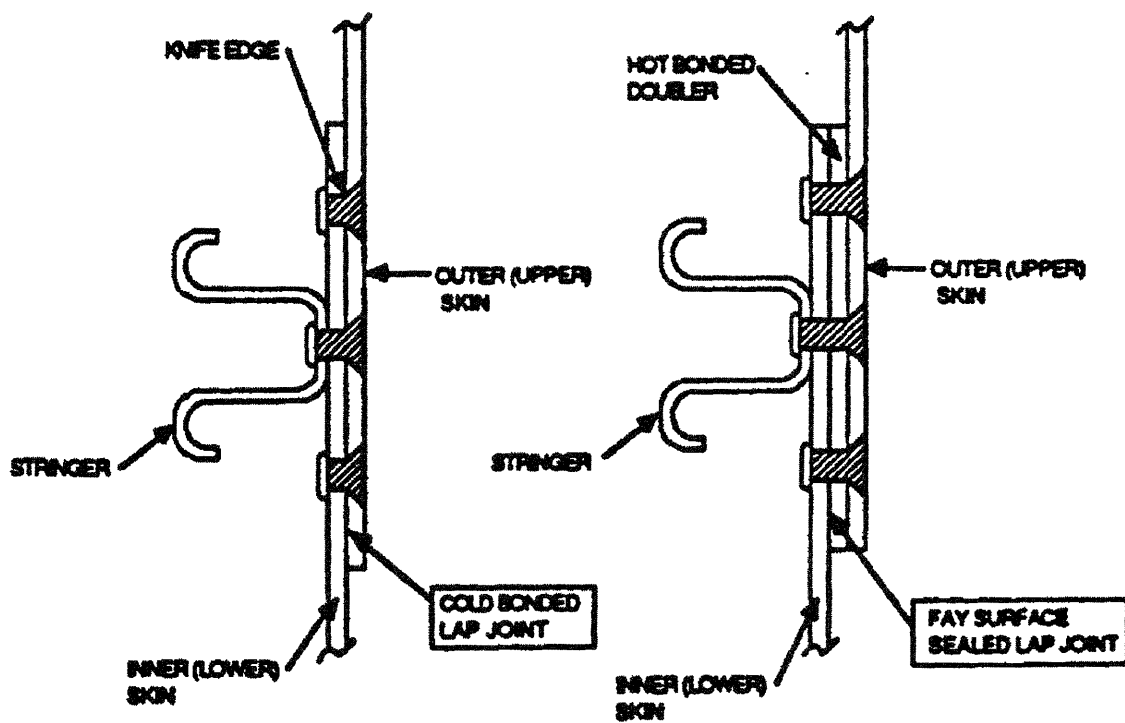
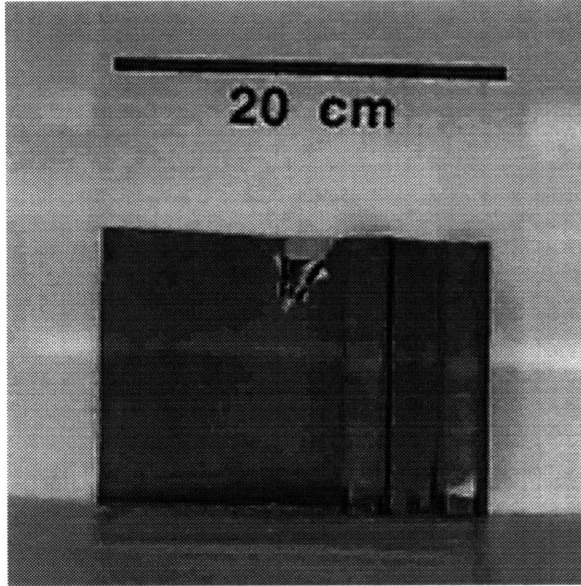Figure 7-1: Diagram of a Typical Lap Joint

Figure 7-2: Photograph of Lap Joint 1 (Front View)

7.1   Lap Joint 1

Figures 7.2, 7.3, and 7.4 each show a different view of one of the repaired lap joints. We will refer to this as "lap joint 1." The photograph shows the stringer riveted to the lap joint. The resolution of the photograph does not allow one to see the repaired areas of the lap joint. Lap joint 1 has six rivets running down the center of the stringer, each approximately 2.5 to 5.0 cm apart. The four rivets furthest from the cadmium triangle are larger, longer rivets that were used to repair the lap joint. Also, a bead of excess epoxy approximately 8 cm long has dried to the outside edges of the stringer as a result of the joint repair. Also visible is a cadmium triangle that we placed on the sample to provide a reference point and a way of calibrating distances on the radiograph. The cadmium triangle is a right triangle with legs of 2.54 cm and 1.53.81 cm.

Figure 7.5 shows a radiograph of lap joint 1. The image has been median filtered, and is a 100 second exposure, pixels grouped 4x4, with a beam characterized by 1.94E5 GS-20 counts over 300 seconds. The epoxy strips on each side of the stringer are easily visible, as well as the four replacement rivets, which stand out much more
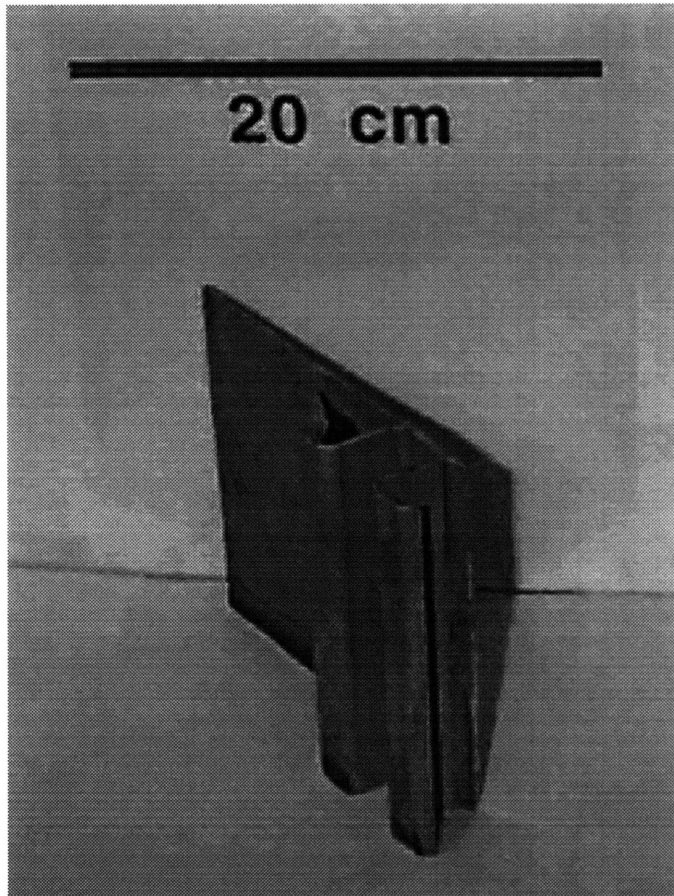
106

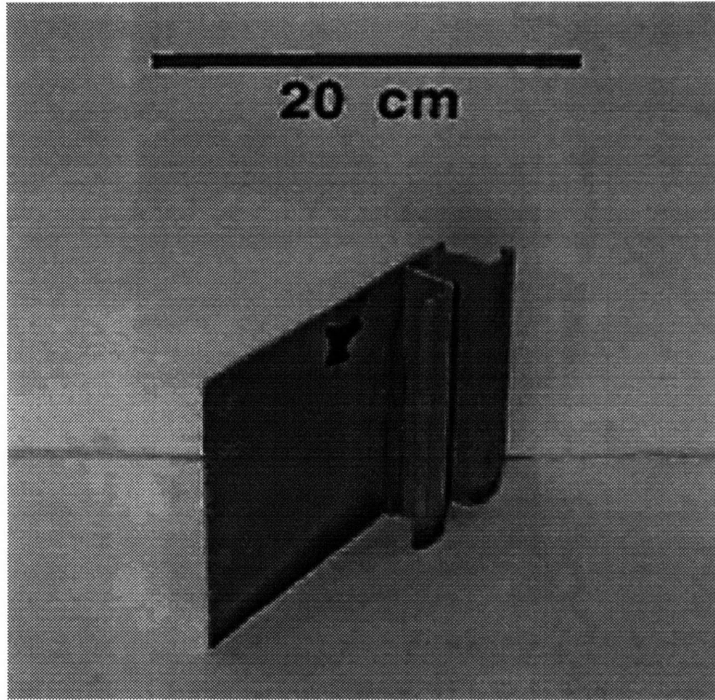Figure 7-3: Photograph of Lap Joint 1 (Side View)

Figure 7-4: Photograph of Lap Joint 1 (Side View)

clearly than the original aluminum rivets. The cadmium triangle shows up very well, also. The darker regions under the stringer and around the repaired rivets indicate the presence of hydrogen, either from epoxy or corrosion products.

7.2 Lap Joint 2

Figures 7.6 and 7.7 show different views of lap joint 2. This lap joint shows rivets on either side of the stringer as well as down the middle, for a total of three rows of rivets. Again, the repaired rivets, epoxy, and cadmium triangle are visible features. This cadmium triangle has legs 2.54 cm and 5.08 cm long. Figure 7.8 is a radiograph of lap joint 2. The image has been median filtered, and is a 100s second exposure, pixels grouped 4x4, 1.93E5 GS-20 counts over 300 seconds. Again, the epoxy, replacement rivets, and cadmium triangle are easily visible in the radiograph.
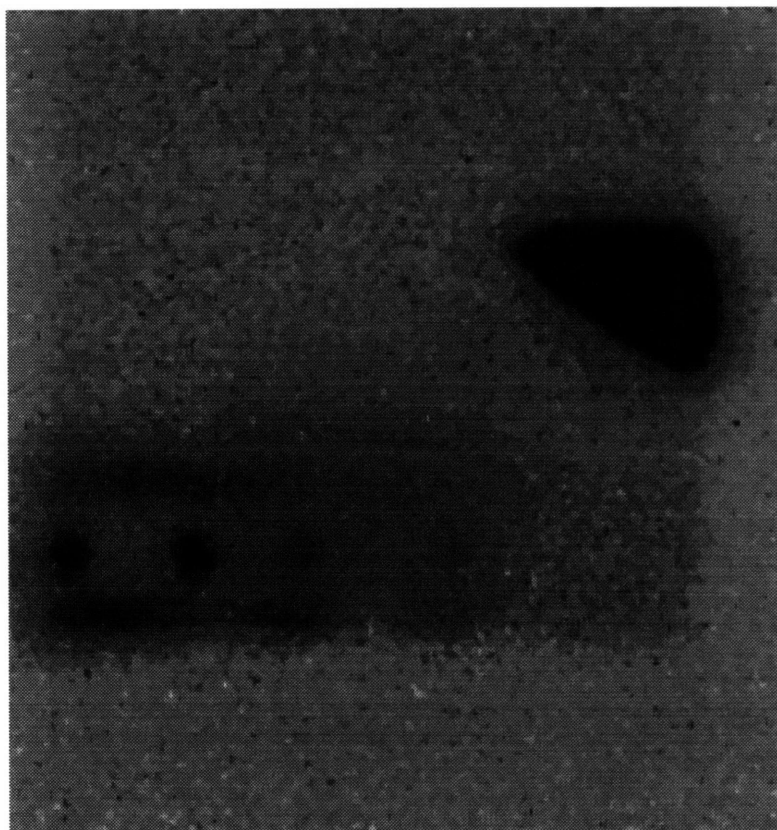
Figure 7-5: Radiograph of Lap Joint 1
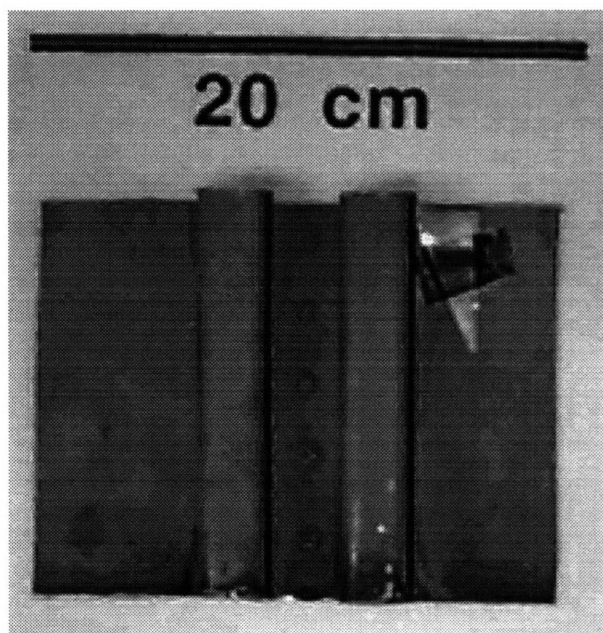
Figure 7-6: Photograph of Lap Joint 2 (Front View)
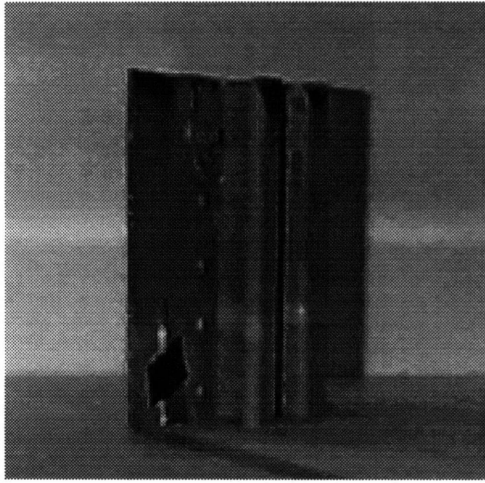
Figure 7-7: Photograph of Lap Joint 2 (Side View)
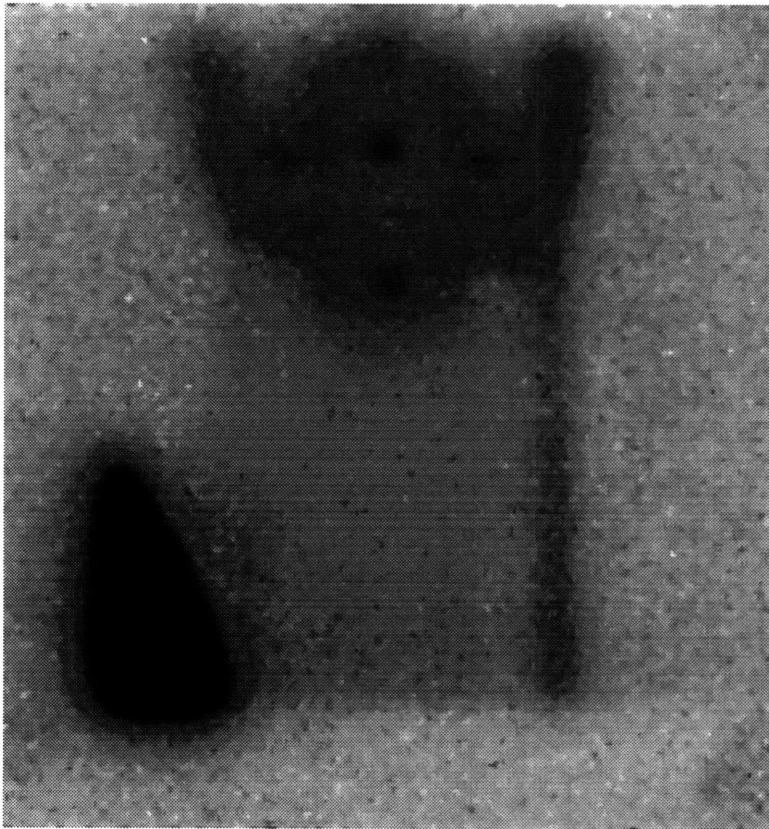
Figure 7-8: Radiograph of Lap Joint 2
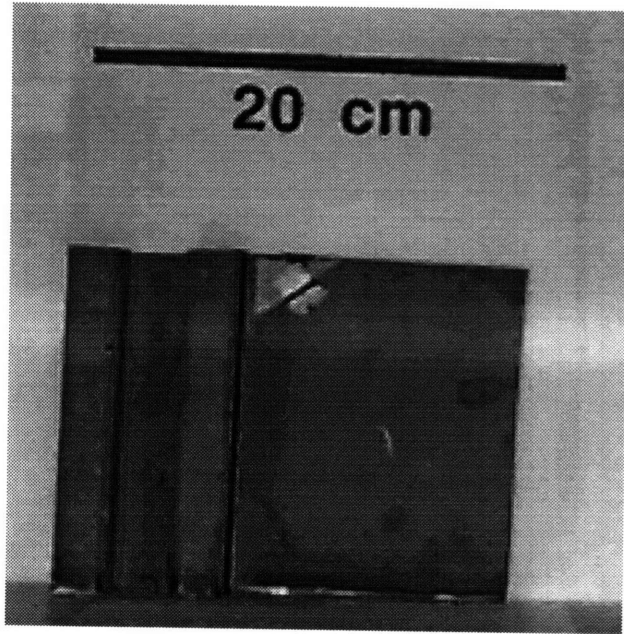
Figure 7-9: Photograph of Lap Joint 3 (Front View)

7.3 Lap Joint 3

Figure 7.9 is a photograph of lap joint 3, which is very similar to a mirror image of lap joint 1. The cadmium triangle used as a reference for this radiograph has legs 1 inch and 1,5 inches long. Figure 7.10 is a radiograph of lap joint 3. The image has been median filtered, and is a 100 second exposure, pixels grouped 4x4, 1.92E5 GS-20 counts over 300 seconds.
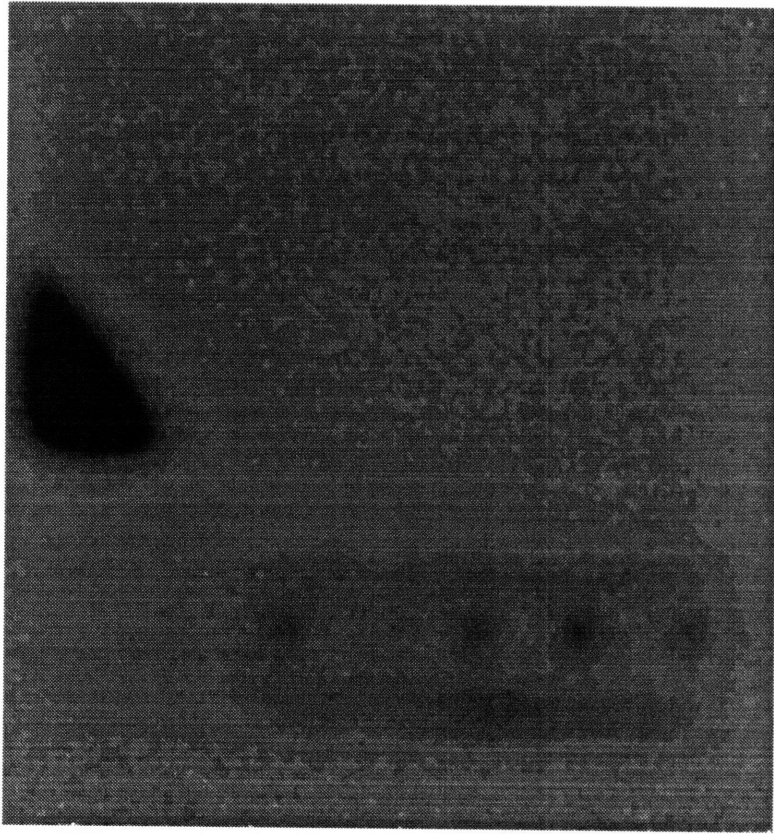
Figure 7-10: Radiograph of Lap Joint 3

Chapter 8

Conclusions

8.1 System Weaknesses

8.1.1 Noise Sources

One area that the system needed improvement in was in shielding it from noise sources. These include x-rays producing noise in the CCD chip and fast neutrons and x-rays producing noise at the scintillator screen. Because part of the signal is generated from these fast neutrons and x-rays, the differences in signal level between two regions in the radiographic image is not due to thermal neutron attenuation differences alone. The difference in signal level is also due to differences in fast neutron and x-ray attenuation. This is seen by looking at the predicted attenuation and measured attenuation in the polyethylene phantom. The measured values are close to the predicted values, but an error is present. This error is due to the fact that we assumed the entire signal was a measure of thermal neutrons, so signal attenuation could only be caused by one thing, thermal neutron attenuation. In reality, the signal was a combined measure of thermal neutrons, fast neutrons, and x-rays, so signal attenuation **cannot** be attributed to thermal neutron attenuation alone.

These noise sources also reduce our effective maximum flux. Each image pixel can contain a maximum of 3.2E5 A-D counts before it is saturated. If 1.0E5 of these

counts are from noise sources such as fast neutrons and x-rays, only 2.2E5 of these A-D counts are measuring the desired quantity, thermal neutron fluence. If we can shield from these noise sources, we increase the thermal neutron fluence we are able to measure, which improves image noise characteristics and spatial resolution (see chapter 2).

8.1.2 Collimation

The system also could be improved with collimation. Spatial resolution was good for thin objects, but if this system is to be used on thicker objects, a more collimated neutron beam would be required to maintain spatial resolution. Since tomography usually is done on objects with appreciable thickness, a better collimated beam is required before the system can be used for tomography.

8.1.3 Corrosion vs. Epoxy

The system demonstrated that it was very capable at imaging hydrogen in aluminum objects. The problem with using this system to detect corrosion products in aluminum aircraft components is that many epoxies and sealants are used in aircraft assembly, especially in regions where corrosion is likely to take place, such as crevices and joints. Unless a radiograph of the components is taken immediately after construction to image the location and thickness of hydrogen containing epoxies and sealants before exposure to corroding environments, and this radiograph is saved for reference throughout the lifetime of the aircraft, dark areas on radiographs of aircraft components can be either epoxy or corrosion product. The only way to determine what caused the neutron attenuation is to perform a destructive test.

One possible method to discriminate between corrosion products and epoxy on the radiographs is to look at the standard deviation of the pixels. Epoxy tends to

be much more uniform in thickness and density than corrosion products, because it is applied intentionally. This results in a much "cleaner" signature for epoxy and sealants. Corrosion products, on the other hand, tend to be less uniform in thickness and density. This results in a larger variation of pixel level for a corroded area and an area that is covered in epoxy. This can be seen by looking at the plot of average pixel level created for the phantom made of corrosion strips and the wax phantom. The average pixel level of the corrosion strips, even after median filtering, is very noisy. This can be seen by the jagged appearance of the line in Figure 6.5. The average pixel value of the wax phantom in Figure 6.14, however, is much smoother. This difference in standard deviation is probably due to the fact that the wax phantom had the hydrogen containing material applied in an even, deliberate manner. The corrosion products are much less uniform in nature.

8.2   System Strengths

8.2.1   Portable System

The main goal of this work was to take a technology which had proven useful in a limited number of applications and expand the range of possible uses. Neutron radiography has previously been limited in its applicability due to the fact that nuclear reactors were required for neutron sources of sufficient intensity for imaging. These sources were expensive, required highly trained personnel to operate, and were stationary. Objects to be radiographed had to be brought to the reactor site, and then highly trained operators had to use delicate equipment to produce the radiograph. The process was time consuming and expensive.

By switching to an accelerator source, we have greatly reduced the cost of a neutron source, made it much simpler to operate, and relatively simple to transport. The detector assembly is made of commercially available components. They are robust

enough to be able to handle shipping or a field environment, such as an assembly line or an aircraft hangar. The detector is also easy to control, using simple "point and click" software interfaces.

8.2.2   Source Strengths

More intense, portable neutron sources opened neutron radiography to a wide field of applications it had previously been close to due to the monopoly reactors had on strong neutron sources. Radiofrequency Quadrupole accelerators like the DL-1 provided a much smaller machine capable of producing high intensity ion beams for use as neutron sources. The DL-1 neutron source has a number of advantages over traditional reactor sources.

The DL-1 is much cheaper to build and operate than a nuclear reactor. Additionally, it is relatively simple to operate compared to a nuclear reactor. Except for warming the machine up after it has been down for a few days, the machine can be turned on and off with a simple switch. Also, the DL-1 is a portable machine, unlike a nuclear reactor. All of these factors combine to make the DL-1 neutron source much more attractive in many areas than a nuclear reactor.

The DL-1, when operating at approximately 50% of maximum current, produced $8.8x10^8 \frac{n}{s}$ with a thermal flux in the imaging area of $1.3x10^4 \frac{n}{cm^2 s}$. This source proved to be strong enough for the imaging applications desired.

8.2.3   Detector Strengths

The imaging system used was highly successful. The lens coupled CCD provided a source that combined the best characteristics of earlier types of neutron detectors. It had a high dynamic range like scintillator detectors. It is a linear, stationary system

like the Anger Camera, and it had excellent spatial resolution like film detectors.

In addition to being a composite of the best qualities of other types of neutron detectors, it was made entirely of commercially available components. This made for a system that operated on "point and click" software interfaces. It also makes the imaging system rugged enough to be easy transported and robust enough for use in environments other than a clean lab space, such as an airplane hangar or an assembly line.

8.2.4   Time Considerations

Previously, portable neutron sources existed, but they were too weak to allow for neutron radiographs to be produced with a reasonable exposure time (minutes). As accelerator based neutron sources grew stronger and position sensitive neutron detectors improved, this time decreased. We have demonstrated that this system is capable of imaging a wax layer 1.3E-2 cm thick with a spatial resolution of 6.3E-2 cm with a 100 second exposure.

8.3   Future Development

8.3.1   Moderator Design

One area that has received very little attention during all of this development was the design of a neutron moderator. The moderator presently in place was designed simply to meet the shielding requirements to operate the neutron source. Effort in this area is likely to increase the thermal neutron flux and perhaps make a more uniform strength beam.

8.3.2 Collimation

Two collimators were designed and tested. Both used a boron loaded powder (boron carbide) mixed with a latex paint as a neutron absorbent coating. One collimator consisted of a series of aluminum plates 5 cm wide that were spaced approximately 1 cm apart. One set of plates was held horizontally, and behind those a set of plates was held vertically, creating an effective grid with an L/D ratio of 5. The other collimator consisted of the same paint applied to a plastic honeycomb. The honeycomb openings were 0.72 cm in diameter and the honeycomb was 6.7 cm thick, for an L/D ratio of 9.3.

We considered using cadmium to create a collimator, but concern over x-ray noise created in the (n,gamma) in cadmium detracted from this idea. These collimators seemed to help the spatial resolution, as can be seen by the plot of the Modulus Transfer Function with and without collimator (see Figure 4.7). Continued work may increase the spatial resolution of the system.

8.3.3 Quantify the Noise Response

The scintillator screen was never tested specifically for it's response to x-ray and fast neutron sources. This should be performed to determine if shielding the scintillator from x-rays and reducing the number of fast neutrons would decrease the system noise. The scintillator could be shielded from x-rays with lead, which is essentially transparent to neutrons. The fast neutron flux could be decreased by moving the detector so it is not directly in line with the target. Because most of the fast neutrons are produced in the forward direction (see Figure 4.X), only lower energy neutrons or neutrons would strike the detector. "Fast" neutrons could not strike the detector because they would not be in line with the scintillator. The only way those "fast" neutrons could make it to the scintillator screen is to undergo one or more moderating, direction altering collisions.

Additionally, the shielding of the CCD could be improved. Presently, it consists of a single layer of 5 cm thick lead bricks around the base of the CCD. This is poor because the bricks are not perfectly shaped, and gaps between bricks exist. A better solution would be to design a lead collar to fit around the CCD, eliminating the gaps caused by the bricks.

8.3.4 Tomography

This system has proven to be a viable radiographic system. A next logical step would be to develop it to the point where it could perform tomography. Shuanghe Shi [29] has already developed the necessary software and hardware to accomplish this. The system now must be tested to see if the detector and source are capable of tomography.

Bibliography

[1] Aircraft accident investigation report (translation), far eastern air transport, ltd., boeing 737-200, b-2603. Technical report, Civil Aeronautics Administration, Ministry of Communications, Taipei, Taiwan, Republic of China, 1981.

[2] Aircraft accident report: Aloha airlines, flight 243, boeing 737-200, n73711. Technical Report PB89-910404, National Transportation Safety Report, 1989.

[3] Inc. AccSys Technology. *Operating and Maintenance Procedures for Model DL-1 RFQ Neutron Generator*, first edition, 1991.

[4] H. Berger. *Neutron Radiography*. Elsevier Press, 1985.

[5] Inc. Bicron. *Catalog*, 1990.

[6] P. D. Burns. Signal to noise ratio of charge coupled device imagers. *SPIE: Charge Coupled Devices and Solid State Optical Sensors*, 1242, 1990.

[7] W. E. Dance S. F. Carollo and F. J. Horak. Demonstration of mobile accelerator neutron radiography for in situ detection of moisture and corrosion in aircraft structures. Technical Report AIAA-83-2449, AIAA Aircraft Design, Systems and Technology Meeting, October 1983.

[8] J. P. Cassidy. Application of neutron radiation inspection at the pantex plant. In *Neutron Radiography: Proceedings of the First World Conference*. D. Reidel Publishing Co., 1983.

[9] Jim C. I. Chang. Aging aircraft science and technology issues and challenge and usaf aging aircraft program. In *Structural Integrity in Aging Aircraft*. American Society of Mechanical Engineers, 1995.

[10] P. Convert and J. B. Forsyth. *Position Sensitive Detection of Thermal Neutrons*. Academic Press, 1983.

[11] G. E. Cooke and H. D. Healy. A study to determine the annual direct maintenance for weapons systems and equipment in the united states air force. Technical Report Contract #F09693-89-C-3016, Systems Exploration, Inc., 1990.

[12] Signal Analytics Corporation. *IPLab Spectrum User's Guide*, version 2.4 edition, 1993.

[13] J.C. Domanus. *Collimators for Thermal Neutron Radiography*. D. Reidel Publishing Co., 1987.

[14] J. Stokes et. al. A new accelerator based radiography system. In *Neutron Radiography: Proceedings of the First World Conference*. D. Reidel Publishing Co., 1983.

[15] W. E. Dance et. al. Diane: Advanced system for mobile neutron radiography. *Nuclear Instruments and Methods in Physics Research B*, 40:1316–1321, 1989.

[16] L. Laporte G. Bayon and J. Le Gall. A review of ten years of operation of the industrial neutron radiography facilities associated with the triton reactor at fontenay aux roses nuclear research center. In *Neutron Radiography: Proceedings of the First World Conference*. D. Reidel Publishing Co., 1983.

[17] A.A. Harms and D.R. Wyman. *Mathematics and Physics of Neutron Radiography*. D. Reidel Publishing Co., 1986.

[18] M. R. Hawkesworth. Neutron radiography: Equipment and methods. *Atomic Energy Review*, 15(2), 1977.

[19] M. Howard and G. O. Mitchell. Nondestructive inspection for hidden corrosion in u.s. air force aircraft lap joints: Test and evaluation of inspection procedures. In *Structural Integrity in Aging Aircraft*. American Society of Mechanical Engineers, 1995.

[20] Nucleus Inc. *Personal Computer Analyzer: Operation and Instruction Manual*, version 880109 edition, 1988.

[21] D. A. Jones. *Principles and Prevention of Corrosion*. Prentice Hall, 1992.

[22] H. Kallman. Neutron radiography. *Research*, 1, 1948.

[23] G. F. Knoll. *Radiation Detection and Measurement*. John Wiley and Sons, 1989.

[24] Andreas Koch. Lens coupled scintillating screen-ccd x-ray area detector with a high detective quantum efficiency. *Nuclear Intruments and Methods in Physics Research A*, 38:654–658, 1994. CCD Data for PI 1242E.

[25] R. L. Newacheck. Applications and trends of industrial neutron radiography. In *Neutron Radiography: Proceedings of the First World Conference*. D. Reidel Publishing Co., 1983.

[26] E. McFarland R. Lanza and S. Shi. A cooled ccd based neutron imaging system for low fluence neutron sources. 1995.

[27] E. W. McFarland R.C. Lanza and J. Leigh. Detection and characterization of the heterogeneous distribution of hydrogen in titanium compressor blades by neutron computed tomography. *Journal of Advanced Materials*, pages 3–10, April 1995. Info on all parts of imaging system and Radiography theory.

[28] W.V. Schemp and E. Toker. Signal to noise ratio calculations. Note No. 1.

[29] Shuanghe Shi. An accelerator based neutron imaging system and its application to detection of corrosion in aircraft. Master's thesis, Massachussetts Institute of Technology, 1995.

[30] A. I. Shpetnyi. Energy and angular distribution of neutrons emitted in the $be^9(d, n)b^{10}$ reaction. *Soviet Physics JETP*, 5(3), October 1957.

[31] A. R. Spowart. Measurement of the absolute detection efficiency of granular and glass neutron scintillators. *Nuclear Instruments and Methods*, 75:35–42, 1969.

[32] A. R. Spowart. Measurement of the gamma sensitivity of granular and glass neutron scintillators and films. *Nuclear Instruments and Methods*, 82:1–6, 1970.

[33] A.R. Spowart. Optimising neutron scintillators for neutron radiography. *British Journal of N.D.T.*, 11(1):9, March 1969.

[34] J. W. Staples. *RFQs - An Introduction*. American Institute of Physics, 1992.

[35] J. Thewlis. Neutron radiography. *British Journal of Applied Physics*, 7, 1956.

[36] H. H. Uhlig and R. W. Revie. *Corrosion and Corrosion Control*. John Wiley and Sons, 1985.

[37] S. F. Carollo W. E. Dance and H. M. Bumgardner. Mobile accelerator neutron radiography system. Technical Report AMMRC TR 84-39, Army Materials and Mechanics Research Center, October 1984.

[38] A. H. Warth. *The Chemsitry and Technology of Waxes*. Reinhold Publishing Co., 1960.